J Adv Ceram

Review

Recent progress and challenges in photocatalytic green hydrogen production

Mengxi Tan[1,✉], Jing Chen[1,✉], Zenghui Zhang[3], Lushan Ma[1], Luhan Wang[1], Yang Li[1], Yang Bai[2,✉]

Cite this article: Tan M, Chen J, Zhang Z, et al. *J Adv Ceram* 2026, **15**(3): 9221241. https://doi.org/10.26599/JAC.2026.9221241

ABSTRACT: Photocatalytic green hydrogen (H_2) production technology, as a clean technology that replaces traditional fossil fuel-based H_2 production, has emerged as a research focus in addressing energy shortages and environmental pollution due to its unique advantage of being driven by solar energy. In recent years, remarkable advancements have been made in the design of photocatalysts and the investigation of reaction mechanisms, but the restricted light absorption range, high recombination rate of photogenerated carriers, and insufficient stability are still serious constraints on the increase in energy conversion efficiency. The development of high-performance photocatalysts is crucial for achieving efficient solar-to-hydrogen (STH) conversion. This review deeply analyzes the fundamental principles of photocatalytic green H_2 production from three dimensions: optimization of light absorption performance, regulation of charge dynamics, and enhancement of surface reaction kinetics. It systematically reviews the recent research achievements in this field and deeply deconstructs the design strategies of photocatalysts, aiming to provide references for the rational design of ideal photocatalysts and more in-depth mechanism analysis. Finally, future research directions and potential breakthroughs are discussed, with the aim of accelerating the development and practical application of solar-driven green H_2 production technology.

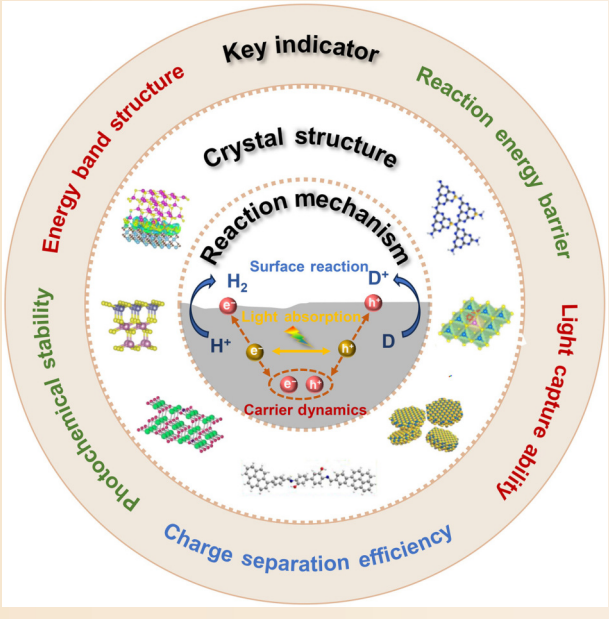

KEYWORDS: photocatalytic H_2 production; light absorption; charge dynamics; surface reaction kinetics

1 Introduction

Energy shortages and environmental pollution are two serious challenges to the sustainable development of society [1–3]. With the rapid development of the global economy, the continuous increase in energy demand has led to the excessive consumption of traditional fossil energy, which not only results in decreasing reserves of energy sources but also causes a series of serious environmental problems, such as greenhouse gas emissions and atmospheric pollution [4–6]. Therefore, it is urgent to develop clean and sustainable new energy sources. Among the numerous alternative energy sources that have attracted much attention, hydrogen energy, as an energy carrier with high energy density, has become the ideal candidate for meeting the long-term energy needs of humankind, with its significant advantages of clean, zero carbon, and no secondary pollution [7–9]. According to the "2024 Global Hydrogen Review", the global demand for H_2 reached 97 million tons in 2023, an increase of 2.5% over the previous year [10]. H_2 can be categorized as gray hydrogen, blue hydrogen, and green hydrogen based on the degree of carbon emissions generated during H_2 production [11–13]. Gray hydrogen is derived from fossil fuels through techniques such as steam methane reforming or coal gasification, offering low costs but generating significant carbon emissions [14,15]. Blue hydrogen also utilizes fossil fuels but incorporates carbon capture, utilization, and storage technology, resulting in substantially lower carbon emission intensity [16]. Green hydrogen is generated from renewable energy sources such as wind power, hydropower, and solar power through technologies including water thermolysis, photolysis, and electrolysis, achieving zero carbon emissions

[1] College of Chemistry and Chemical Engineering, Henan University of Technology, Zhengzhou 450001, China. [2] Beijing Key Laboratory of Materials Intelligent Technology, Institute for Advanced Materials and Technology, University of Science and Technology Beijing, Beijing 100083, China. [3] China Tobacco Shaanxi Industrial Co., Ltd., Xi'an 710065, China.

✉ Corresponding authors. E-mail: M. Tan, mxtan@haut.edu.cn; J. Chen, chenjing0504@haut.edu.cn; Y. Bai, baiy@mater.ustb.edu.cn

Received: October 23, 2025; Revised: December 27, 2025; Accepted: January 5, 2026

during the production process [17–19]. Currently, H_2 production remains in a stage characterized by "gray H_2 dominance, blue H_2 transition, and green H_2 incubation" [20,21]. Ninety-six percent of H_2 production relies on fossil fuels, with each kilogram of gray H_2 production generating 10–12 kg of CO_2 emissions [22–24]. The electricity cost for H_2 production through water electrolysis is high, and the efficiency and durability of the electrolysis cells are insufficient, resulting in high operational and maintenance costs [16,25,26]. Photocatalytic water splitting for H_2 production technology utilizes photogenerated carriers in semiconductor materials, creating a new path for the direct conversion of solar energy into chemical energy, with simple system design, low cost, and scalability [1,27,28]. By 2025, the global annual solar irradiation is projected to reach approximately 120,000 TW, far exceeding the energy consumption of humanity per year (30 TW) [29–31]. Photocatalytic H_2 production technology converts abundant but intermittent solar energy into chemical energy, demonstrating great potential for large-scale applications. The development of this technology is expected to promote the transformation of the energy structure and alleviate the reliance of humanity on traditional energy sources.

Since Fujishima and Honda [32] discovered that TiO_2 electrodes can decompose water to produce H_2 under light in the 1970s, photocatalytic technology has attracted extensive attention from the scientific community and has become one of the research hotspots in the fields of energy and environment [32–36]. As displayed in Fig. 1, in recent years, this technology has made significant progress in the research of photocatalysts and the exploration of reaction mechanisms [37–41]. Among them, the unsatisfactory performance of the photocatalyst is the key factor restricting its development. Photocatalysts often suffer from a high recombination rate of photogenerated carriers, narrow light absorption range, and limited catalytic active sites, which results in low H_2 production efficiency and makes it difficult to achieve large-scale industrial applications [42–46]. Therefore, developing efficient photocatalysts has become the core task for promoting the progress of photocatalytic H_2 production technology. Common photocatalysts include metal sulfides (CdS, ZnS, MoS_2, $ZnIn_2S_4$ (ZIS)), transition metal oxides (TMOs; TiO_2, MnO, CuO, ZnO), carbon nitrides (g-C_3N_4), perovskite materials ($SrTiO_3$ (STO), Cs_2SnI_6, $Cs_3Cu_2Br_5$), etc. [47–59]. Among them, metal sulfides, with their narrow bandgap, possess a wide range of light absorption and exhibit excellent photocatalytic performance [30,60–64]. However, these materials have poor chemical stability and are prone to photocorrosion under light and reaction conditions. The S^{2-} on the surface of metal sulfides is prone to being oxidized by photogenerated holes to form S or SO_4^{2-}. In addition, some metal sulfides (e.g., CdS) are toxic, posing harm to the environment [38]. Transition metal oxides exhibit excellent photochemical stability, along with wide availability and low cost, making them suitable for large-scale applications [28,65–68]. Nevertheless, the large bandgap results in limited utilization of visible light, which restricts the efficiency of photocatalytic H_2 production to a certain extent [69]. Carbon nitride (g-C_3N_4) features a suitable bandgap structure, along with favorable characteristics such as good chemical stability, low cost, and easily available raw materials (e.g., urea and melamine). However, it tends to agglomerate during the preparation process, resulting in a poor specific surface area that undermines mass transfer efficiency. Meanwhile, the high recombination rate of photogenerated carriers due to inferior crystallinity further restricts its photocatalytic performance [70–75]. Benefiting from their excellent structural tunability, the bandgap of perovskite materials can be adjusted within a wide range through component regulation, but they exhibit poor chemical stability and are prone to decomposition by water, oxygen, and light [59,76–78]. Moreover, most high-efficiency perovskite photocatalysts contain heavy metal ions (Pb^{2+}), which tend to leach from the lattice during photocatalytic reactions, causing water pollution [79]. Although lead-free perovskite photocatalysts have been developed, their photocatalytic activity and stability are still inferior to those of lead-based perovskites, making complete replacement difficult. As mentioned above, various types of photocatalysts have their own advantages and inherent limitations in the field of H_2 production. It is of great practical significance to systematically summarize the latest research progress on these photocatalysts in H_2 production. In recent years, existing reviews have primarily focused on the technical details of individual modification strategies [80,81]. Therefore, there is an urgent need for a comprehensive and timely review that systematically summarizes the breakthrough achievements in this field, deeply analyzes the microscopic regulatory mechanisms behind various modification strategies, and provides clear references for the precise positioning of future research directions in this field.

This review systematically summarizes the latest research progress in the field of photocatalytic H_2 production, with a focus on elaborating the design concepts, controllable synthesis methods, and performance regulation strategies of photocatalysts, as displayed in Fig. 2. Based on the fundamental principles of photocatalytic H_2 production, this review comprehensively analyzes the regulatory mechanisms and inherent laws underlying modification strategies from three core perspectives: light absorption, charge dynamics, and surface reaction kinetics. By integrating the current research status and core challenges faced in this field (such as low separation efficiency of photogenerated carriers and insufficient stability), this review further looks forward to future development directions (such as the construction of multifunctional composite photocatalysts and the development of in situ characterization technologies for reaction mechanisms). This study not only provides novel insights into the design of high-performance photocatalysts but also offers valuable guidance for promoting in-depth theoretical research and the expansion of practical applications of photocatalytic H_2 production technology.

2 Mechanisms of photocatalytic H_2 production

The reaction process of photocatalytic H_2 production is roughly divided into several core steps [82–84]. As depicted in Fig. 3(a), the first stage is light absorption. The photocatalyst absorbs photons of specific wavelengths, exciting electrons in the valence band (VB) to the conduction band (CB) and forming photogenerated electron–hole pairs [85–87]. Subsequently, the second stage is charge migration. The photogenerated carriers separate and migrate to the active sites of photocatalysts [88–90]. Finally, the third stage is the surface reaction. The photogenerated electrons participate in the reduction reaction of protons to generate H_2, while holes are consumed by oxidation of the sacrificial agent or water [91–93]. In this process, the photogenerated charges need to overcome the losses from bulk recombination and surface recombination [94,95]. Meanwhile, the potential of the photogenerated electrons involved in the reaction must be more negative than the proton reduction potential to ensure the thermodynamic requirements of the reaction [96,97]. The bandgap structures of common photocatalysts are shown in Fig. 3(b). For the commercialization of photocatalytic H_2 production technology, the core requirement is to exceed the critical threshold of 10% for solar-to-hydrogen (STH) production

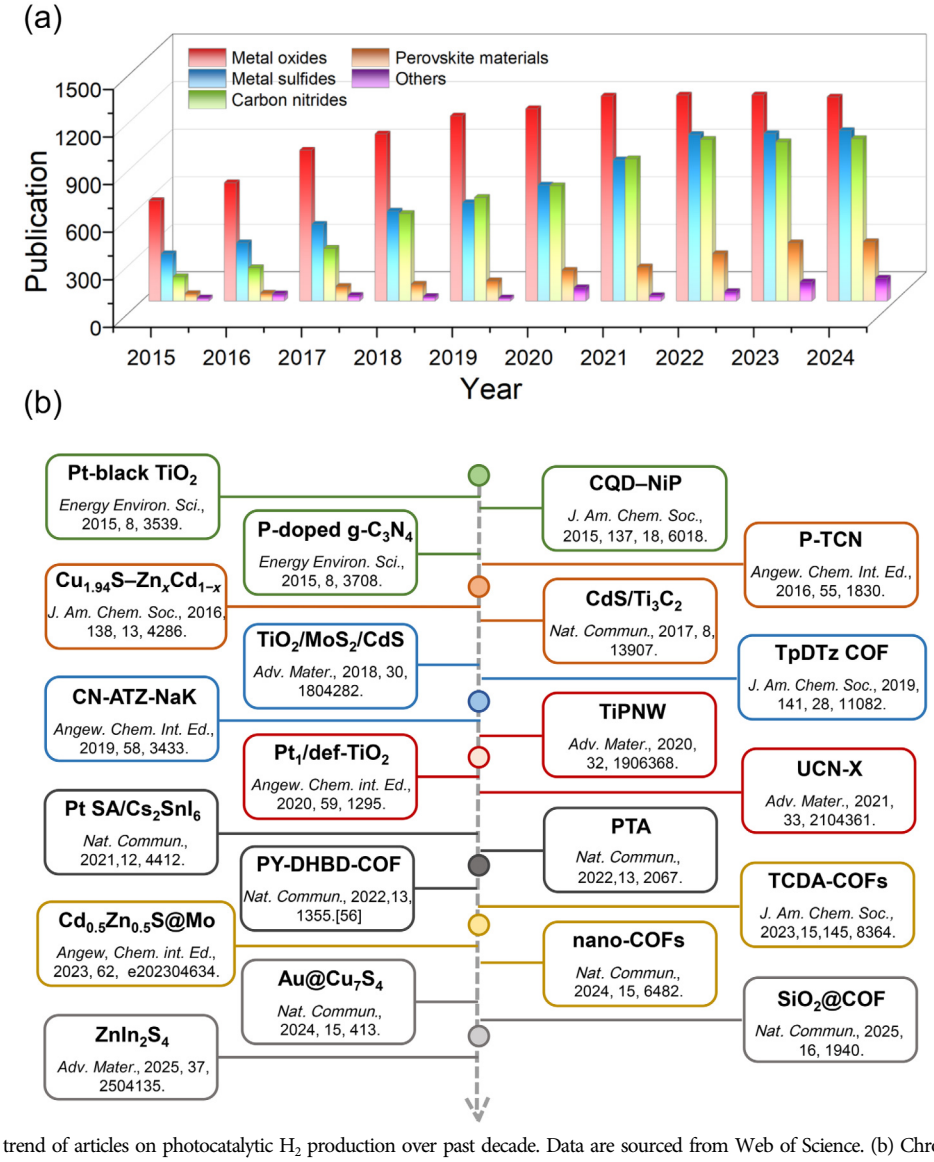

Fig. 1 (a) Publication trend of articles on photocatalytic H_2 production over past decade. Data are sourced from Web of Science. (b) Chronology of representative photocatalysts for solar H_2 production.

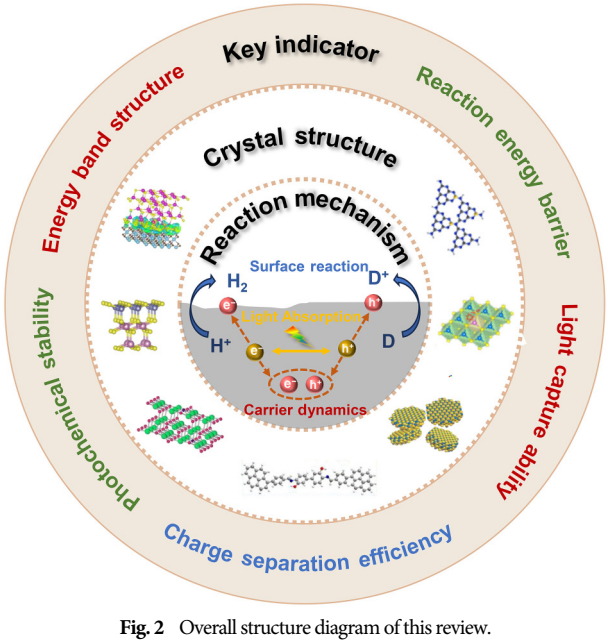

Fig. 2 Overall structure diagram of this review.

efficiency [98,99]. The STH efficiency is synergistically determined by three factors: light absorption capacity, charge separation efficiency, and surface reaction efficiency [100–102]. However, achieving this target still faces multiple core challenges. First, the narrow visible light response range of photocatalysts results in a low utilization rate of solar energy. Second, the sluggish charge dynamics process and insufficient migration and separation efficiency of photogenerated carriers directly limit the number of active species participating in surface reactions. Third, the scarcity of surface active sites further restricts the progress of reaction kinetics. Based on this, the following sections systematically explore the core regulation strategies and related mechanisms of light absorption, charge dynamics, and surface reaction kinetics.

From the perspective of the electronic structure, the essence of the light absorption process is that electrons in semiconductors absorb the energy of photons and undergo energy level transitions, which are closely related to the characteristics of the electron distribution in the VB, CB, and bandgap. The energy band structure of semiconductors arises from the interactions between atomic energy levels [104]. In isolated atoms, electrons move around the nucleus and have discrete energy levels, with significant energy differences between the levels [105]. A large

number of atoms combine through chemical bonds to form semiconductor crystals, where the extranuclear electron clouds of adjacent atoms overlap [106]. The interaction between atoms causes the originally discrete energy levels to split, and these split levels merge to form energy bands. In the electronic structure of semiconductors, the VB is formed by the hybridization of atomic bonding orbitals and is the energy band filled with electrons [107]. The CB is composed of atomic antibonding orbitals or high-energy level empty orbitals and is an energy band that is not occupied by electrons or contains only a small number of electrons [108]. The bandgap between the top of the VB and the bottom of the CB is the energy interval in which electrons cannot exist stably [109]. As shown in Fig. 4(a), semiconductors can be categorized into direct bandgap semiconductors and indirect bandgap semiconductors [5]. Specifically, the VB maximum (VBM) and CB minimum (CBM) of direct bandgap semiconductors are located at the same wave vector position in the Brillouin zone. For such semiconductors, electron transition only requires the absorption of photon energy and can be accomplished without the assistance of phonons to compensate for the momentum difference. When photons irradiate the surface of semiconductors, electrons that are originally bound in the VB gain energy and then leap to the CB, becoming free-moving photogenerated electrons, while positively charged holes are left in the VB [110]. Notably, only photons with energy matching the bandgap can enable the electrons to complete the transition. The following equation needs to be satisfied between the energy of the incident photon and the bandgap of photocatalysts: $h\nu = hc/\lambda \geq E_g = E_{VB} - E_{CB}$. Here, h represents the Planck constant ($\approx 6.626\times10^{-34}$ J·s^{-1}), ν is the frequency of the incident photon, c signifies the speed of light ($\approx 3.0\times10^{8}$ m·s^{-1}) in a vacuum, λ is the light wavelength, and E_g corresponds to the bandgap energy. E_{VB} and E_{CB} represent the energy levels of VB and CB, respectively [111]. For indirect bandgap semiconductors (Fig. 4(b)), the VBM and CBM are located at different wave vector positions in the Brillouin zone. When electrons in such semiconductors undergo transition, they not only need to absorb photon energy but also have to compensate for the momentum difference by absorbing or emitting phonons to satisfy the law of momentum conservation [110]. The involvement of phonons increases the complexity of the electron transition process, resulting in a much lower electron transition probability in indirect bandgap semiconductors than in direct bandgap semiconductors [5]. The light absorption capacity of photocatalysts can be quantitatively compared based on the absorption coefficient, $\alpha(h\nu)$, which is determined by all possible band transitions that occur from the VB to CB: $\alpha(h\nu) \propto \sum P_{12} \times g_V(E_{VB}) \times g_C(E_{CB})$. In the equation, P_{12} denotes the transition probability of electrons from the VB to CB. $g_V(E_{VB})$ and $g_C(E_{CB})$ correspond to the density of states (DOS) in the VB and CB, respectively [5]. The former reflects the number of electrons in the VB that participate in transitions, while the latter represents the number of vacancies in the CB that accommodate the transitioned electrons. In experimental characterization, ultraviolet-visible diffuse reflectance absorption spectroscopy is commonly applied to compare the light absorption capabilities of different photocatalysts. The ideal photocatalysts are equipped with exceptional light-harvesting capabilities. In the energy distribution of the solar spectrum, infrared light (52%–55%) possesses insufficient energy to drive reactions, while ultraviolet light (3%–5%), despite its high energy, induces severe photocorrosion that deactivates catalysts [112]. Visible light (42%–43%), however, offers moderate energy intensity and abundance. Therefore, efficient capture of visible light contributes to excellent photocatalytic performance. As shown in Figs. 4(c) and 4(d), the dye sensitization and localized surface plasmon resonance (LSPR) strategies are two typical means of regulating light absorption

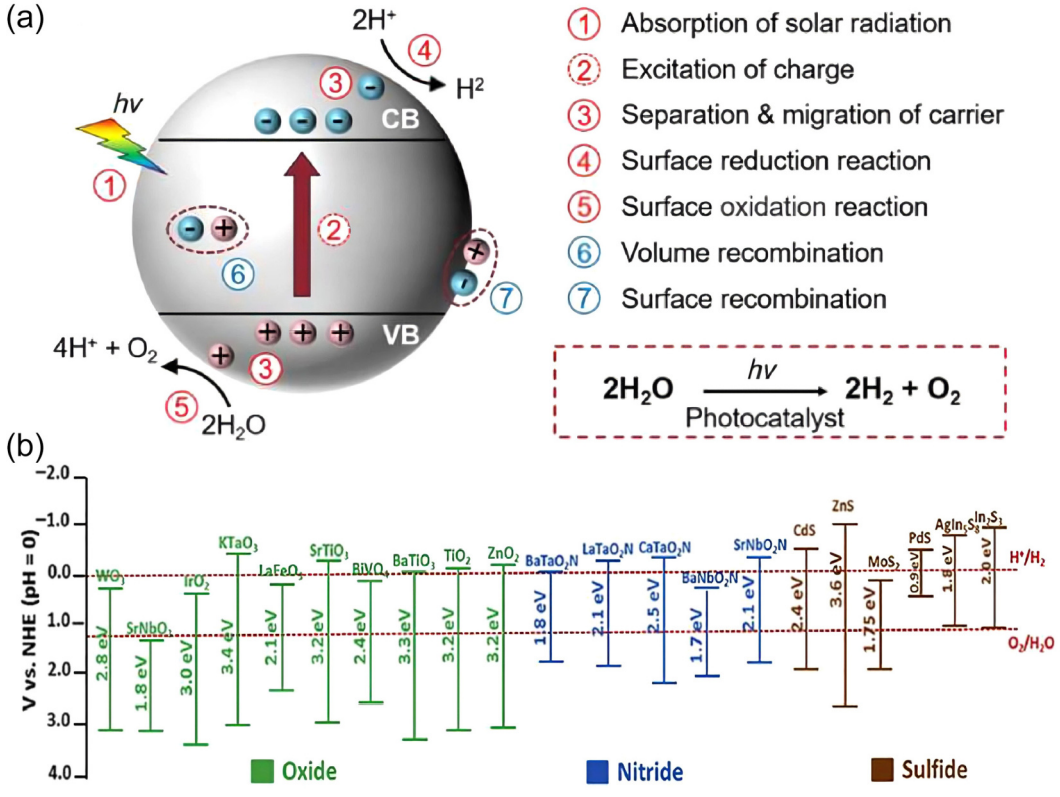

Fig. 3 (a) Reaction process of photocatalytic H_2 production. Reproduced with permission from Ref. [80], © Elsevier Ltd. 2023. (b) Bandgap structures of common photocatalysts. Reproduced with permission from Ref. [103], © The Authors 2018.

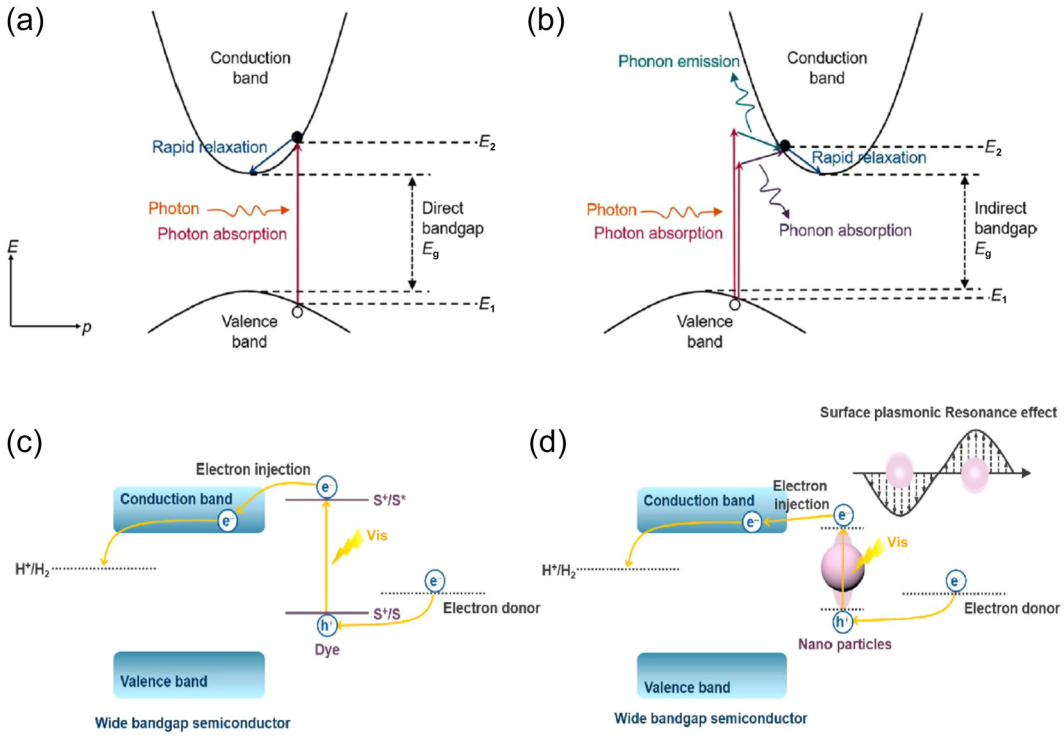

Fig. 4 Process of light absorption in (a) direct bandgap semiconductors and (b) indirect bandgap semiconductors. (c) Dye sensitization and (d) LSPR strategies. Reproduced with permission from Ref. [5], © American Ceramic Society 2019.

performance. These methods improve the light absorption capacity of the photocatalyst by broadening the light response range and enhancing the local light field intensity. Dye sensitization (Fig. 4(c)) refers to the process of anchoring dye molecules with visible light response properties onto the surface of photocatalysts [113]. When dye molecules absorb photons of specific wavelengths, electrons in their VB undergo a transition to the excited state. Once the energy level of the excited state for the dye is higher than that of the CB for the photocatalyst, the excited electrons will be rapidly injected into the CB of the photocatalyst, while the dye molecules are oxidized and subsequently regenerated via reduction by electron donors in the reaction system [114]. Dye sensitization can significantly broaden the light response range of wide bandgap photocatalysts. Moreover, the diverse types of dye molecules enable targeted absorption of light at specific wavelengths. Plasma photocatalysts are based on the LSPR effect of metal nanostructures [11]. When the frequency of incident light matches the plasmon oscillation frequency of metal nanoparticles, it triggers the collective resonance of free electrons, resulting in a strong localized electromagnetic field enhancement effect [114]. On the one hand, the enhanced localized field significantly boosts the light absorption intensity of the photocatalyst. On the other hand, the high-energy hot electrons generated by resonance can be injected into the CB of the photocatalyst to participate in the reaction, while the thermal effect produced during the process also assists in facilitating the photocatalytic reaction [115]. In addition, the Schottky junction interface formed between the metal and photocatalyst suppresses the recombination of photogenerated charges, thereby further improving the conversion efficiency of photogenerated charges [116].

The photocatalytic H_2 production reaction needs to satisfy both thermodynamic and kinetic requirements. First, from a thermodynamic perspective, the decomposition of 1 mol H_2O requires 237 kJ of energy under standard conditions, so the energy of incident photons should be greater than 1.23 eV [117]. To maximize the utilization of solar energy, the E_g of the photocatalyst must be less than 3.0 eV, corresponding to a light absorption boundary of approximately 400 nm [118]. At the same time, the potential of CB should be lower than the reduction potential of protons. The kinetics mainly include charge carrier dynamics and surface reaction kinetics. Charge dynamics in photocatalysis refer to the behavior of photogenerated carriers from generation to migration into the surface active sites. The core process involves the generation of photogenerated carriers from photons absorbed by the photocatalyst, followed by efficient separation of the carriers, overcoming Coulombic attraction and arriving at the surface of the catalyst via bulk phase migration. Among them, the exciton binding energy, which is the energy required for an exciton to dissociate into free electrons and holes, directly affects the dissociation efficiency of photogenerated carriers [116]. Its magnitude is closely related to the dielectric constant, the effective mass of electrons, and the crystal structure [119]. Following charge separation, photogenerated carriers migrate to active sites through diffusion and drift mechanisms (Fig. 5(a)). The diffusion mechanism is a random thermal movement driven by concentration differences and follows Fick's law [120]. Drift is a migration process influenced by an external electric field [110]. Common methods to establish an external electric field include constructing heterojunctions, establishing polarization fields, and introducing vacancies or element doping [121–123]. These methods utilize the interfacial energy band bending, built-in electric field, and local electric potential difference to drive the directional migration of charges or promote charge separation by forming electron traps [124,125]. Based on recent research advances, energy band engineering has been demonstrated as a core strategy for regulating the charge transfer dynamics and enhancing the separation efficiency of photogenerated charges, which serves as an effective approach to boost the photocatalytic performance [126]. As shown in Fig. 5(b),

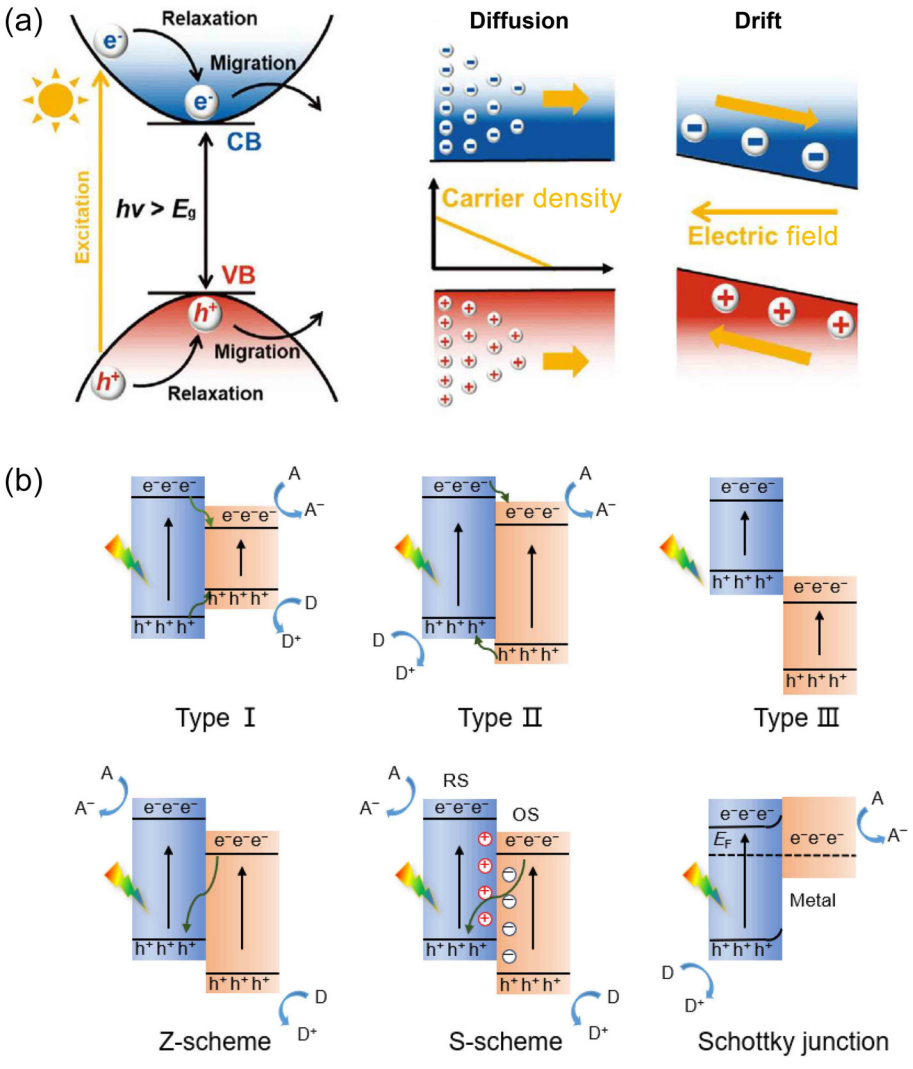

Fig. 5 (a) Schematic diagram of light excitation and carrier migration processes. Reproduced with permission from Ref. [110], © The Authors 2024. (b) Energy band structure of types I, II, III heterojunctions, Z-scheme, S-scheme, and Schottky junction systems. Reproduced with permission from Ref. [127], © Elsevier B.V. 2021.

according to the differences in energy band structures, heterojunctions can be categorized into type I, type II, and type III heterojunctions, as well as Z-scheme and S-scheme heterojunctions and Schottky junctions [5]. Among them, the photogenerated electrons and holes in type I heterojunctions migrate together into a single semiconductor phase, facilitating their recombination. Type III heterojunctions with split bandgap structures struggle to achieve directed charge separation due to the lack of an effective driving force for the relative migration of photogenerated electrons and holes, thereby limiting their potential to enhance photocatalytic performance [127]. Z-scheme heterojunctions with a staggered band structure can drive the directional migration of photogenerated charges along the Z-scheme pathway by virtue of the built-in electric field induced by the Fermi energy level (E_F) difference at the interface. This process enables the selective consumption of photogenerated carriers with weak redox capability while retaining those with strong redox activity to participate in the photocatalytic reaction, thereby significantly enhancing the photocatalytic efficiency [128]. The S-scheme heterojunction is formed by the combination of oxidative semiconductors with reductive semiconductors, exhibiting similar characteristics to the Z-scheme heterojunction in terms of bandgap arrangement and charge migration pathways. When metals or semiconductors with metallic properties come into contact with photocatalysts, the energy band of the photocatalyst at the interface bends upward, thereby establishing a unidirectional photogenerated charge transport channel from the photocatalyst toward the metal [63]. This strategy effectively facilitates the separation of photogenerated carriers and ultimately achieves a significant enhancement in photocatalytic performance. In addition, as displayed in Fig. 6(a), the separation and transfer of charges need to span complex temporal and spatial scales from femtoseconds to seconds and from atoms to micrometers, which is a key factor affecting the photocatalytic performance [129,130]. Importantly, the recombination of photogenerated charges is much faster than their migration and depletion in the photocatalyst bulk (a few ps) and at the surface (tens of ns) [131,132]. Only a small amount of photogenerated charges can be involved in the final surface reaction, resulting in a low photocatalytic performance. Therefore, the merit of charge dynamics is one of the important factors that directly determines the overall performance of the photocatalytic reaction.

The surface reaction kinetics in photocatalytic H_2 production mainly focus on the process where the photogenerated electrons migrate to the catalyst surface and then react with the adsorbed protons to form H_2. This involves several key steps, such as the adsorption of reactants, charge transfer, reaction energy barriers, intermediate formation, and product desorption (Fig. 6(b)).

Specifically, protons or water molecules first bind to the reduction active sites (e.g., metal cocatalysts, defective sites) on the surface of the photocatalyst through physical/chemical adsorption. Then, photogenerated electrons are transferred from the surface to the adsorbed protons, undergoing the intermediary transformation of $H^+ \rightarrow H^* \rightarrow H_2$ (H^* is hydrogen atoms adsorbed at the active site) [133]. Finally, the two molecules of H^* are bound together to form H_2 and desorbed. The rate of this process is determined by the number of active sites, adsorption strength, charge transfer efficiency, and reaction energy barrier, and it is also regulated by the surface electron density, temperature, and pH of the solution [134–136]. In the field of photocatalysis and other heterogeneous catalysis, the turnover number (TON) and turnover frequency (TOF) are core performance indicators directly related to the catalytic activity and surface reaction kinetics and can quantitatively characterize the efficiency and kinetic features of surface reactions [137]. Among them, TON is defined as the ratio of the number of electrons participating in the photocatalytic reaction to the number of active sites in the photocatalyst [138]. The number of reactive electrons can be quantitatively derived from the amount of H_2 production by photocatalysis [139]. However, since the number of active sites in photocatalysts is usually difficult to determine accurately, the number of atoms or surface atoms in the photocatalyst is often used for approximate calculation in practical research. It should be noted that this approximation method counts inactive atoms as equivalent active sites; thus, the calculated TON values are generally lower than the actual values [138]. The core value of TOF lies in its ability to directly reflect the catalytic reaction efficiency of a single active site within a unit of time, making it a key indicator for evaluating the intrinsic activity of photocatalysts [138]. Although in actual reaction systems, the composition and surface structure of photocatalysts are complex and variable, which makes it difficult to accurately obtain the true TOF values, TOF can still effectively eliminate interference from nonintrinsic factors such as photocatalyst dosage and specific surface area. It serves as an important parameter for comparing the surface reaction kinetics of similar photocatalysts in a horizontal manner [139]. Furthermore, the hydrogen adsorption free energy (ΔG_{H^*}) directly governs the adsorption–desorption behavior of the key intermediate H* on the surface of photocatalysts, serving as the core descriptor determining the surface reaction rate of photocatalytic H_2 production [140]. A negative value of ΔG_{H^*} indicates that the binding of H* to the active sites on the photocatalyst surface is excessively strong, which will hinder the desorption of the product H_2 and lead to sluggish surface reaction kinetics [141]. Conversely, an excessively positive ΔG_{H^*} value indicates the poor adsorption of H* onto active sites, hindering proton reduction to H_2 and similarly limiting reaction rates [142]. Only when ΔG_{H^*} approaches 0 eV, the adsorption and desorption of H* reach a dynamic equilibrium, and the surface reaction activity achieves its maximum value [143]. ΔG_{H^*} enables precise correlation between the structure and intrinsic activity of photocatalysts, providing a crucial theoretical basis for the rational design of highly active photocatalysts and the optimization of surface reaction kinetic pathways [139]. It has been reported that the loading of cocatalysts not only facilitates charge separation and transfer but also optimizes the reaction pathway to lower the energy barrier. For example, the modification of Pt can optimize ΔG_{H^*}, lower the reaction energy barrier, and significantly

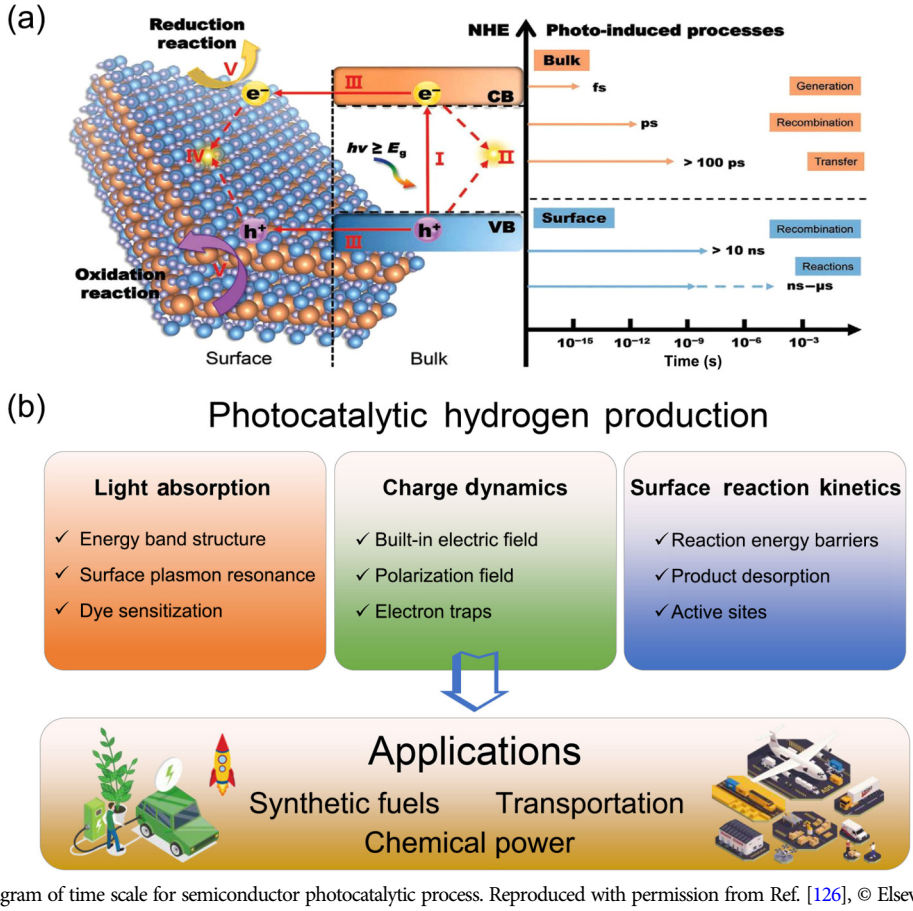

Fig. 6 (a) Schematic diagram of time scale for semiconductor photocatalytic process. Reproduced with permission from Ref. [126], © Elsevier B.V. 2025. (b) Factors affecting photocatalytic H_2 production and future applications.

清華大学出版社 Tsinghua University Press | SciOpen

accelerate the kinetics of H_2 generation, while the presence of surface hydroxyl groups further enhances the reaction rate by facilitating proton transfer [144–146]. Surface defects and vacancies significantly increase the adsorption rate of reaction molecules [147–149]. Specific active sites significantly enhance the reaction activity and selectivity by stabilizing key intermediates [150,151]. In addition, compared with traditional photocatalysts, single-atom photocatalysts (SAPCs) exhibit unique advantages in terms of surface reaction kinetics [121]. SAPCs are catalytic systems formed by anchoring metal active components in the form of individual atoms onto the surface or lattice of the carrier [12,60]. The adsorption energy of their single-atom active sites can be precisely regulated by controlling the carrier types and the coordination structures of single atoms [22]. SAPCs can not only selectively capture the oxygen atoms in H_2O molecules through atomic-level structure design, effectively weakening the H–O bond energy to promote the dissociation of H_2O molecules but also precisely control the adsorption strength of the products, ensuring that the H_2 molecules are quickly desorbed from the surface of the photocatalyst after their formation, thus avoiding the occupation of active sites [23]. Additionally, SAPCs offer the significant advantages of nearly 100% atomic utilization and uniform active sites.

3 Photocatalysts for solar H_2 generation

Solar-driven H_2 production via photocatalysis is a highly promising strategy for renewable energy conversion, and the rational design of photocatalysts is pivotal to enhancing its efficiency [5]. Photocatalysts for H_2 generation are typically classified based on their chemical composition and structural characteristics [110]. This review systematically surveys representative photocatalyst systems, primarily including metal sulfides, transition metal oxides, carbon nitrides, perovskite materials, MXenes, and porous organic frameworks [47,48,50,55]. Starting from the general characteristics of various photocatalysts, the specific modification strategies and recent research progress are elaborated in detail. The activity of the photocatalyst and the detailed modification strategies are summarized in Table 1.

3.1 Metal sulfides

Metal sulfides possess excellent visible light absorption properties, tunable surface electronic configurations, and abundant active sites and have drawn extensive attention from numerous researchers in STH conversion. Generally, metal sulfides are formed by the combination of metal cations (e.g., Cd^{2+}, Zn^{2+}, Mo^{4+}, In^{3+}, etc.) with sulfur anions (S^{2-}) and have a wide variety of

Table 1 List of H_2 production performance for photocatalysts

Photocatalyst	Measure	Sacrificial agent	Cocatalyst	Activity (μmol·g^{-1}·h^{-1})	Light source	Ref.
CdS/NiCoAl-LDH	Type Ⅱ heterojunction	Na_2S, Na_2SO_3	—	2116.1	300 W Xe lamp (AM 1.5G)	[38]
ZIF-8/CdS	Type Ⅱ heterojunction	Na_2S, Na_2SO_3	Ni_2P	21,050	300 W Xe lamp (λ > 420 nm)	[152]
CdS/Ni/TiN	Schottky junction	Na_2S, Na_2SO_3	—	469,430	300 W Xe lamp (AM 1.5G)	[97]
$SnNb_2O_6$/CdS	S scheme heterojunction	—	Ni_2P	11,992	300 W Xe lamp (λ > 420 nm)	[98]
Co_8POM@MXene-CdS	Schottky junction	10 vol% TEOA	—	8130	300 W Xe lamp (AM 1.5G)	[153]
CdS/MoO_2/MoS_2	Bifunctional cocatalyst-modified	10 vol% lactic acid	—	5000	300 W Xe lamp (AM 1.5G)	[154]
In_2S_3-In(OH)$_3$-ZnS	Type Ⅱ heterojunction	Na_2S	—	223,600	A 5 W blue LED light	[155]
CdS/MoS_2/Ti_3C_2	Type Ⅱ heterojunction	10 vol% lactic acid	—	14,880	300 W Xe lamp (λ > 420 nm)	[50]
MoS_2/g-C_3N_4	Type Ⅱ heterojunction	0.1 M TEOA	—	1155	300 W Xe lamp (λ > 420 nm)	[156]
MoS_2/UiO-66-NH_2	Schottky junction	10 vol% TEOA	—	2070	300 W Xe lamp (λ > 420 nm)	[157]
MoS_2@TiO_2	Type Ⅱ heterojunction	TEOA	—	2160	300 W Xe lamp (AM 1.5G)	[158]
MoS_2/ZnO	Type Ⅱ heterojunction	Na_2S, Na_2SO_3	—	235	300 W Xe lamp (λ > 420 nm)	[99]
$ZnFe_2O_4$@$ZnIn_2S_4$	Type Ⅱ heterojunction	TEOA	Au	1145.38	300 W Xe lamp (AM 1.5G)	[159]
Co_3O_4@$ZnIn_2S_4$	S scheme heterojunction	TEOA	—	18,900	300 W Xe lamp (AM 1.5G)	[86]
$Zn_3n_2S_6$	In-doping	Na_2S, Na_2SO_3	—	11,410	300 W Xe lamp ($\lambda \geq$ 400 nm)	[160]
$ZnIn_2S_4$	Core–shell structure	10 vol% TEOA	—	2,970	300 W Xe lamp (λ > 420 nm)	[87]
In_2O_3/$ZnIn_2S_4$	Type Ⅱ heterojunction	10 vol% TEOA	Pt	2,180	300 W Xe lamp (λ > 420 nm)	[89]
MoS_2@$ZnIn_2S_4$	P–N heterojunction	TEOA	—	22,250	300 W Xe lamp ($\lambda \geq$ 400 nm)	[161]
$ZnIn_2S_4$	Mo-doping	TEOA	—	26,700	300 W Xe lamp ($\lambda \geq$ 400 nm)	[90]
$ZnIn_2S_4$/ReS_2	Z scheme heterojunction	Na_2S, Na_2SO_3	—	1322	300 W Xe lamp ($\lambda \geq$ 420 nm)	[91]
ReO_2/ReS_2/$Zn_2In_2S_5$	S scheme heterojunction	TEOA	—	6,750	300 W Xe lamp ($\lambda \geq$ 420 nm)	[162]
ZnCdS/$NiCrO_4$	P–N heterojunction	Na_2S, Na_2SO_3	—	760.89	300 W Xe lamp ($\lambda \geq$ 420 nm)	[92]
$CuInS_2$/CeO_2	S scheme heterojunction	Na_2S, Na_2SO_3	Pt	226,600	300 W Xe lamp (λ > 420 nm)	[94]
TiO_2/Ni-$Zn_{0.2}Cd_{0.8}S$	S scheme heterojunction	Benzylamine	—	4,550	300 W Xe lamp (λ > 420 nm)	[96]
P-doped h-BN/$ZnIn_2S_4$	Z scheme heterojunction	TEOA	—	59,460	300 W Xe lamp (λ > 420 nm)	[62]
MnCdS/$NiCo_2S_4$	Schottky junction	Na_2S, Na_2SO_3	—	34,280	300 W Xe lamp (λ > 420 nm)	[95]
CdS	Adjustment of crystallinity	10 vol% lactic acid	Pt	16,060	350 W Xe lamp ($\lambda \geq$ 420 nm)	[84]
Cu_3SnS_4/$Mn_{0.3}Cd_{0.7}S$	S scheme heterojunction	Na_2S, Na_2SO_3	—	72,500	300 W Xe lamp ($\lambda \geq$ 400 nm)	[37]
WO_{3-x}/$ZnIn_2S_4$	S scheme heterojunction	TEOA	—	14.05	NIR light (λ > 800 nm)	[163]
g-C_3N_4/$ZnIn_2S_4$	Type Ⅱ heterojunction	TEOA	Pt	20,738	300 W Xe lamp (λ > 420 nm)	[164]
ZnCdS/PO/FeCoNiPi-MnO	Type Ⅱ heterojunction	NaH_2PO_2	—	1140	300 W Xe lamp (λ > 420 nm)	[165]

Table 1 (Continued)

Photocatalyst	Measure	Sacrificial agent	Cocatalyst	Activity ($\mu mol \cdot g^{-1} \cdot h^{-1}$)	Light source	Ref.
CuS/MoS_2	Type Ⅱ heterojunction	—	—	85,604	300 W Xe lamp (AM 1.5G)	[8]
Co/MnO/GDY	S scheme heterojunction	TEOA	—	2117.33	300 W Xe lamp ($\lambda > 420$ nm)	[28]
Quartz/TiO_2	Piezoelectric photocatalysis	Lactic acid	—	20,400	300 W Xe lamp ($\lambda > 420$ nm)	[43]
TiO_2	Adjustment of crystallinity	Methanol	—	4230	300 W Xe lamp ($\lambda > 420$ nm)	[39]
Ni/TiO_2	P–N heterojunction	Formic acid	Ni	2416	300 W Xe lamp ($\lambda > 420$ nm)	[83]
$TiO_2/MoS_2/Cu_2S$	Oxygen vacancies	Methanol	—	3376.7	300 W Xe lamp ($\lambda \geq 400$ nm)	[166]
MnO/CCN	S scheme heterojunction	BzOH	TEOA	791.6	300 W Xe lamp ($\lambda > 420$ nm)	[167]
$ZnO/CeVO_4$	Z scheme heterojunction	Na_2S, Na_2SO_3	—	1289	300 W Xe lamp ($\lambda > 420$ nm)	[168]
ZnO/graphene	Localelectric field effect	TEOA	—	1400	Natural sunlight	[169]
ZnO/ZnS	Z scheme heterojunction	Na_2S, Na_2SO_3	—	71,860	300 W Xe lamp ($\lambda > 420$ nm)	[170]
ZnO	Oxygen vacancies	Na_2S, Na_2SO_3	Pt	5780	250 W Hg high-pressure lamp	[171]
ZnO@ZnS	S scheme heterojunction	TEOA	Pt	207.95	300 W Xe lamp ($\lambda > 420$ nm)	[172]
CDs/TCN	Photothermal effect of carbon dots	TEOA	—	12,940	300 W Xe lamp ($\lambda > 420$ nm)	[54]
$g\text{-}C_3N_4$	Ultrathin nanosheet	10 vol% TEOA	Pt	4300	300 W Xe lamp ($\lambda > 420$ nm)	[173]
$g\text{-}C_3N_4$	Introduction of phosphate groups	TEOA	Pt	976,700	300 W Xe lamp ($\lambda > 420$ nm)	[174]
PCN	K-doping	TEOA	Pt	7840	300 W Xe lamp ($\lambda > 420$ nm)	[40]
$600\text{-}CuMn_2O_4/GDY\text{-}40\%$	S schemeheterojunction	15 vol% TEOA	Mn_2O_3	1586.54	300 W Xe lamp ($\lambda > 420$ nm)	[175]
$NiCS_3/g\text{-}C_3N_4$	Built-inelectric field	TEOA	—	951	300 W Xe lamp ($\lambda > 420$ nm)	[42]
$TiO_2/g\text{-}C_3N_4$	Type Ⅱ heterojunction	—	—	808.97	300 W Xe lamp ($\lambda > 420$ nm)	[176]
$g\text{-}C_3N_4$	Schottky junction	TEOA	—	2181	300 W Xe lamp ($\lambda > 420$ nm)	[177]
$CdSe@Ti_3C_2$	Schottky junction	—	—	763.2	300 W Xe lamp ($\lambda > 420$ nm)	[57]
BTT-COFs	Regulation of conjugation degree	Ascorbic acid	Pt	5220	150 W Xe lamp ($\lambda > 420$ nm)	[178]
$COF\text{-}Cu_3TG$	Single-atom electronic bridge	TEOA	—	10,470	300 W Xe lamp ($\lambda > 420$ nm)	[22]
TiO_2/MOF	Type Ⅱ heterojunction	TEOA	—	176.8	300 W Xe lamp ($\lambda > 420$ nm)	[179]
$Al\text{-}Pd/SrTiO_3$	Schottky junction	Methanol	—	1430	300 W Xe lamp (AM 1.5G)	[77]
$SrTiO_3$	Ag-doping	—	—	48.62	300 W Xe lamp (AM 1.5G)	[180]
$Cs_3Cu_2Br_5$	Ag-doping	H_3PO_2/HBr	—	488	300 W Xe lamp ($\lambda > 420$ nm)	[181]
$SrTiO_3$	P-doping	18 vol% Methanol	Pt	400	300 W Xe lamp ($\lambda > 420$ nm)	[76]
Cs_2SnI_6	Schottky junction	HI, 20 vol% H_3PO_2	Pt	430	300 W Xe lamp ($\lambda > 420$ nm)	[182]
$CsPbBr_3$@ZEO-1	Nanoconfinement effect	HI	Pt	4826	300 W Xe lamp ($\lambda > 420$ nm)	[183]
PMA_2PbI_4/MoS_2	Z scheme heterojunction	HI	—	1545	300 W Xe lamp (AM 1.5G)	[184]
MHPs	K-doping	—	—	11.2	300 W Xe lamp ($\lambda > 420$ nm)	[185]

chemical formulae, including binary (e.g., CdS, ZnS, and MoS_2) [9,97,149], ternary (e.g., $ZnIn_2S_4$, $Mn_{0.3}Cd_{0.7}S$, and $CuInS_2$) [37,87,120,130,132], and multivariate systems (e.g., Cu_2ZnSnS_4 and AgInZnS) [186–188]. The metal centers of these sulfides are mostly transition metals, which have abundant d electron orbitals. Their VBs are occupied by the 3p orbitals of S, resulting in a lower positive VB and higher photogenerated hole mobility [189]. By adjusting the types and ratios of the metals, the light absorption and photocatalytic activity can be optimized, giving them a unique advantage in the field of photocatalytic H_2 production [190]. Moreover, as displayed in Fig. 7, the crystal structures of metal sulfides are diverse. The hexagonal wurtzite structure (CdS), composed of tetrahedrally coordinated metal and sulfur atoms, exhibits anisotropic photogenerated carrier transport properties (Fig. 7(a)) [191]. The layered structure (MoS_2) is formed by S–Mo–S sandwich layers stacked by van der Waals forces, in which edge sites (e.g., coordinated unsaturated sites of Mo) serve as active centers for photocatalytic H_2 production (Fig. 7(b)) [191]. A spinel or layered hexagonal structure ($ZnIn_2S_4$), consisting of alternately arranged metal-sulfur polyhedra, has an open framework that facilitates photogenerated charge separation and surface reactions (Fig. 7(c)) [192].

3.1.1 *Binary metal sulfides*

CdS is regarded as an ideal photocatalyst owing to its appropriate bandgap (~2.4 eV) and excellent visible light absorption ability, and is a typical representative of binary metal sulfides. Xue *et al.* [193] synthesized highly dispersed Cu-doped CdS (CCS) nanoparticles by the cation exchange method. As shown in Fig. 8(a), Cu doping caused the CB of CdS to shift toward the positive direction, reducing the bandgap of CdS and enhancing visible light absorption. The phase diagram (Fig. 8(b)) of ΔG_{H^*} indicated that the adsorption of hydrogen atoms in pure CdS was an endothermic process, and the reduction of hydrogen atoms was thermodynamically difficult to carry out. The adsorption sites of S atoms coordinated with two Cd atoms and one Cu atom (−0.753 eV) showed lower ΔG_{H^*} than those coordinated with three Cd atoms in CCS (−0.550 eV). The results of theoretical calculations and experimental characterization confirmed that Cu doping altered the surface electron distribution of CdS, which improved the hydrogen adsorption capacity of the surface active sites. Compared with pure CdS, the photocatalytic H_2 production activity was improved by 11 times. Layered double hydroxides (LDHs) are often used as matrix materials in composite photocatalysts due to their unique layered structure. Yang *et al.* [38]

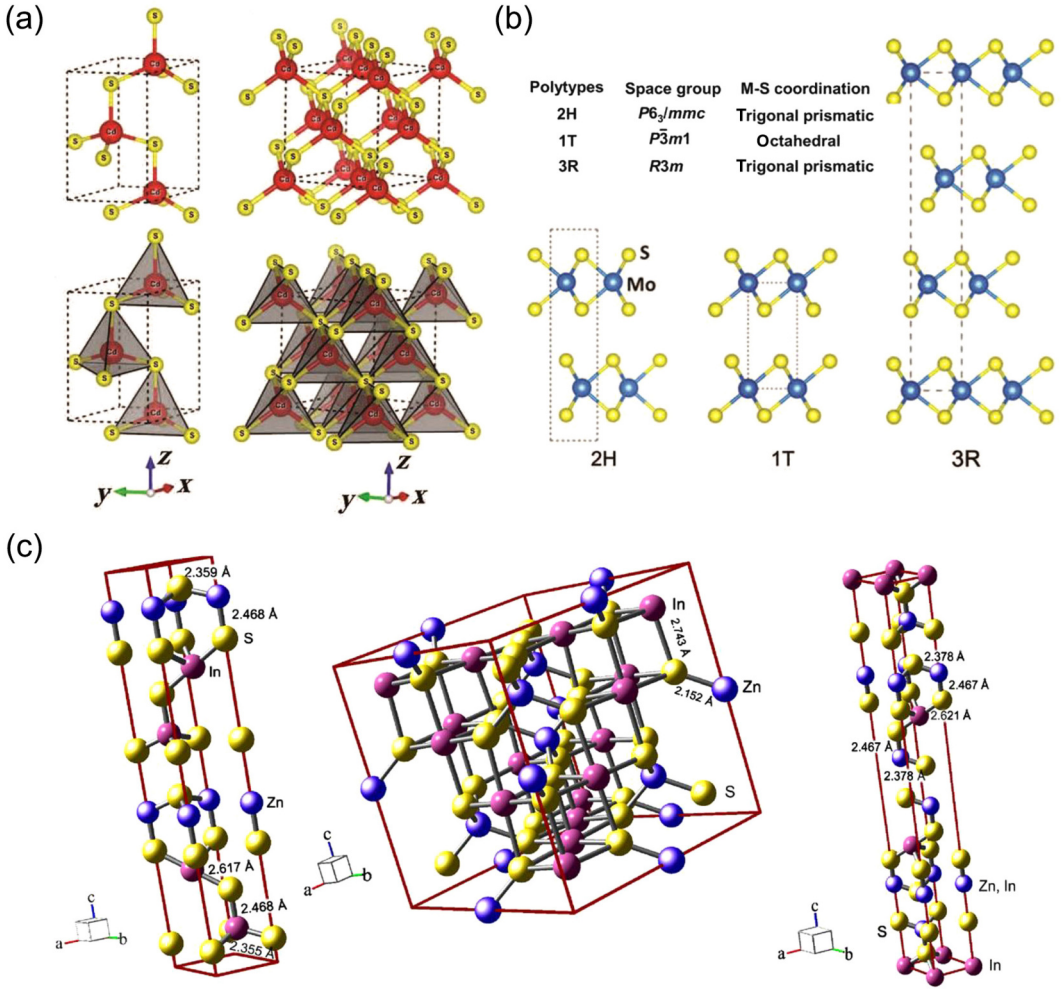

Fig. 7 Crystal structures of (a) wurtzite (left) and zinc-blende (right) CdS and (b) MoS_2. Reproduced with permission from Ref. [191], © Wiley-VCH GmbH 2022. (c) Hexagonal, cubic, and rhombohedral $ZnIn_2S_4$. Reproduced with permission from Ref. [192], © Elsevier Inc. 2011.

loaded CdS nanoparticles onto NiCoAl-LDH with a layered structure. The abundant and tight contact interface provided favorable conditions for photogenerated charge transfer. The enhancement of the interface charge transfer efficiency and light absorption performance significantly improved the photocatalytic performance. Moreover, after four cycles of tests, the photocatalytic H_2 production activity remained at 94%. Studies have shown that the lifetime of photogenerated charges is closely related to the surface and electronic structure of the photocatalyst [97]. Liu *et al.* [97] prepared CdS nanowires by a chemical vapor deposition (CVD) method and deposited Ni and TiN layers sequentially on their surface to construct a CdS/Ni/TiN heterostructure. The Ni layer passivated the defect states on the surface of CdS, which reduced the nonradiative recombination centers on the surface of CdS and prolonged the lifetime of electrons. The LSPR effect of TiN effectively enhanced light absorption, generated high-energy hot electrons to participate in the reaction, and accelerated charge transfer through the high conductivity of TiN. The single-molecule fluorescence (SMF) images (Figs. 8(c)–8(h)) indicated that the discontinuous distribution of Ni and the rough surface formed by the TiN coating increased the reaction contact area and provided more active sites. Furthermore, as depicted in Figs. 8(i) and 8(j), the stepped energy band structure of CdS/Ni/TiN facilitated electron migration from CdS to TiN, while the holes were enriched toward the interior of CdS, achieving spatial charge separation. The STH of the optimized CdS/Ni/TiN reached 14.2%, and the photocatalytic H_2 production rate reached 469.43 mmol·g^{-1}·h^{-1}, which was 20.55 times that of the original CdS. Replacing conventional Pt, Ni_2P functions as an economical cocatalyst that not only acts as an electron trap to inhibit charge recombination but also provides reactive sites, significantly reducing the overpotential of the reaction. The photocatalytic H_2 production efficiency of Ni_2P/ZIF-8/CdS reached 21.05 mmol·g^{-1}·h^{-1}, and the Ni_2P-modified S-type $SnNb_2O_6$/CdS-diethylenetriamine photocatalytic system exhibited a quantum efficiency of 35.8% at 420 nm [98,152].

Chang *et al.* [155] prepared In_2S_3–$In(OH)_3$–ZnS nanofibers by combining hydrothermal and electrospinning methods and explored the effects of $InCl_3$ concentrations on the material morphology, crystal structure, and photocatalytic H_2 production performance. As depicted in Fig. 9(a), the hollow sphere photocatalyst of CdS/MoO_2/MoS_2 was constructed by the simultaneous sulfidation and reduction of $CdMoO_4$ to generate MoS_2 and MoO_2 on the CdS surface [154]. Among them, MoS_2 served as a reduction center to accumulate electrons for H_2 production, while MoO_2 acted as an oxidation center to capture holes and oxidize lactate (LA) for the generation of pyruvic acid (PA). This method of coupling photocatalytic H_2 production with organic synthesis enabled the realization of dual reaction pathways while achieving directional migration and efficient separation of photogenerated charges. Analogously, using Ti_3C_2 as the 2D

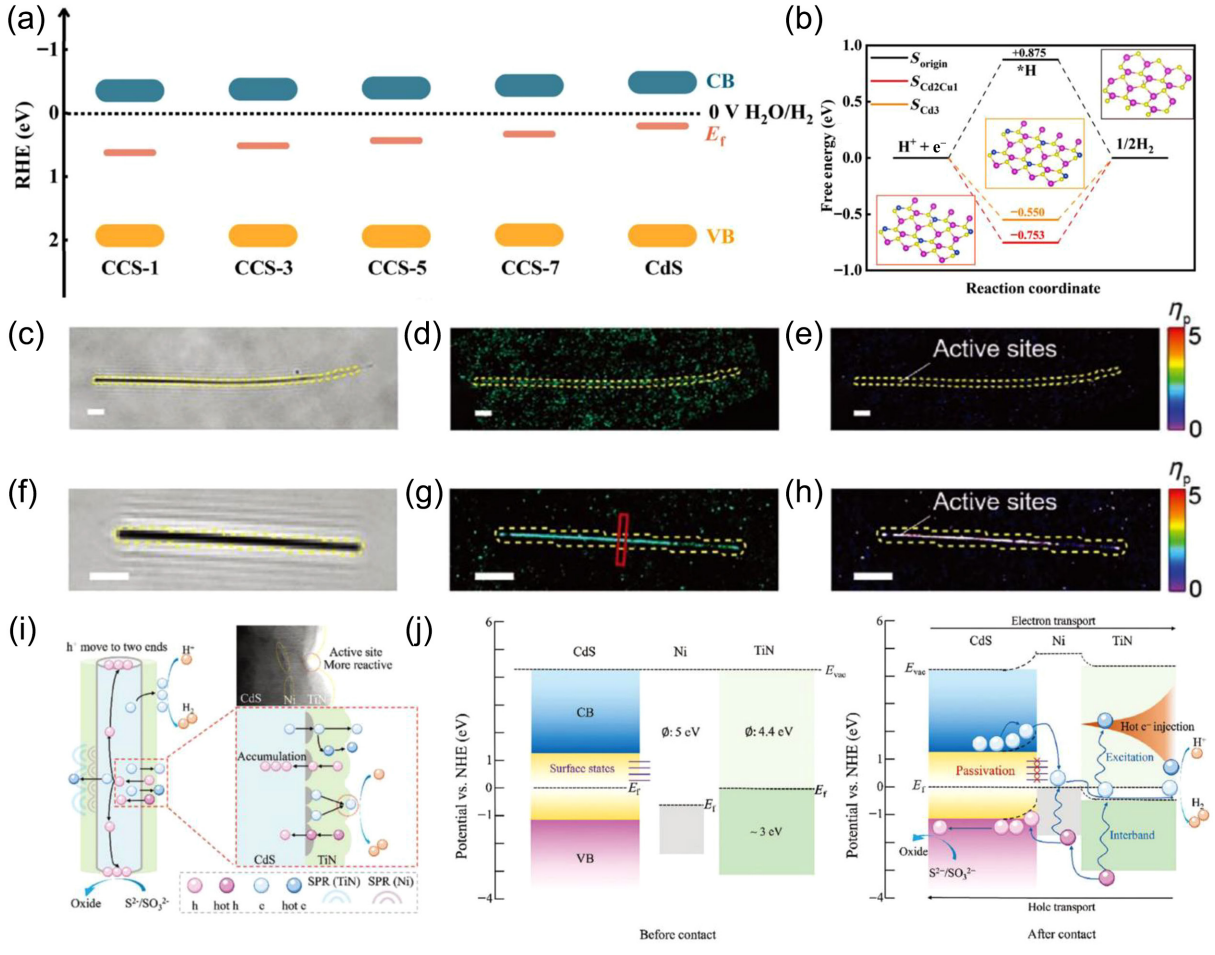

Fig. 8 (a) Energy band structure of CCS and (b) phase diagram of ΔG_{H^*}. Reproduced with permission from Ref. [193], © Hydrogen Energy Publications LLC. 2024. Site-specific photoreduction activities of (c–e) CdS and (f–h) carbon nanotubes (CNTs): (c, f) bright-field images, (d, g) SMF images, and (e, h) corresponding activity density maps. (i) Interface characteristics and active sites of CdS/Ni/TiN; (j) energy band structure of CdS/Ni/TiN. Reproduced with permission from Ref. [97], © Wiley-VCH GmbH 2025.

substrate, MoS_2 and CdS were uniformly loaded on the surface of Ti_3C_2 through self-reduction and a microwave hydrothermal method to form a ternary composite photocatalyst CdS@MoS_2/Ti_3C_2 [50]. Density functional theory (DFT) calculations (Fig. 9(b)) verified the existence of strong interactions at the interface between CdS and Ti_3C_2/MoS_2, where electrons at the interface tended to transfer from Ti_3C_2 to CdS (3.90 e) and subsequently from CdS to MoS_2 (0.33 e). The high electrical conductivity of Ti_3C_2 and the Ti vacancies on its surface were utilized to rapidly transfer charges and capture holes, therefore avoiding S^{2-} oxidation. By taking advantage of the edge S active sites of MoS_2 to capture electrons and subsequently participate in the proton reduction reaction, the reduction of Cd^{2+} was prevented. This targeted charge trapping strategy not only enhanced the charge separation efficiency but also avoided the photocorrosion of CdS, significantly improving the stability of the photocatalyst. The photocatalytic H_2 production rate of CdS@MoS_2/Ti_3C_2 reached 14.88 mmol·h^{-1}·g^{-1}, and the cycling stability lasted for up to 78 h.

3.1.2 *Ternary metal sulfides*

Ternary metal sulfides have garnered extensive focus due to their outstanding catalytic activity, stability, and multifunctionality [194]. Zhang *et al.* [37] prepared S-type heterojunctions of Cu_3SnS_4/$Mn_{0.3}Cd_{0.7}S$ (CTS/MCS) using an ultrasound-assisted self-assembly method (Fig. 10(a)). Through the synergistic effect of the photothermal effect of CTS and the S-type heterojunction, photogenerated charge separation was promoted, which significantly enhanced the photocatalytic H_2 production efficiency. In detail, as shown in Fig. 10(b), the photothermal effect of CTS increased the surface temperature of the catalyst (up to 74.1 °C), which lowered the reaction energy barrier and accelerated the reaction kinetics. The S-type charge transfer pathway promotes the separation of photogenerated charges and retains photogenerated carriers with strong reduction/oxidation capabilities. The charge transfer pathways at the heterojunction interface and the mechanism of the internal electric field were revealed by *in situ* X-ray photoemission spectroscopy (XPS) and DFT calculations. The ability of the photocatalyst to resist interference from salt ions in a simulated seawater environment was verified, demonstrating its potential for practical application. The metal atoms and sulfur atoms in $ZnIn_2S_4$ are arranged alternately to form a layered structure, and the layers are connected with each other by van der Waals forces. The unique structure makes it easy to modify or compound with other semiconductor catalysts. Chen *et al.* [163] loaded WO_{3-x} quantum dots (QDs) onto ZIS nanosheets by means of a low-temperature water bath method. By taking advantage of the synergistic effect between the LSPR generated by WO_{3-x} QDs and the built-in electric field within the interface, the H_2 production rate of WO_{3-x}/ZIS was enhanced by 14.5 times compared to pure ZIS under the photothermal-assisted effect driven by near-infrared

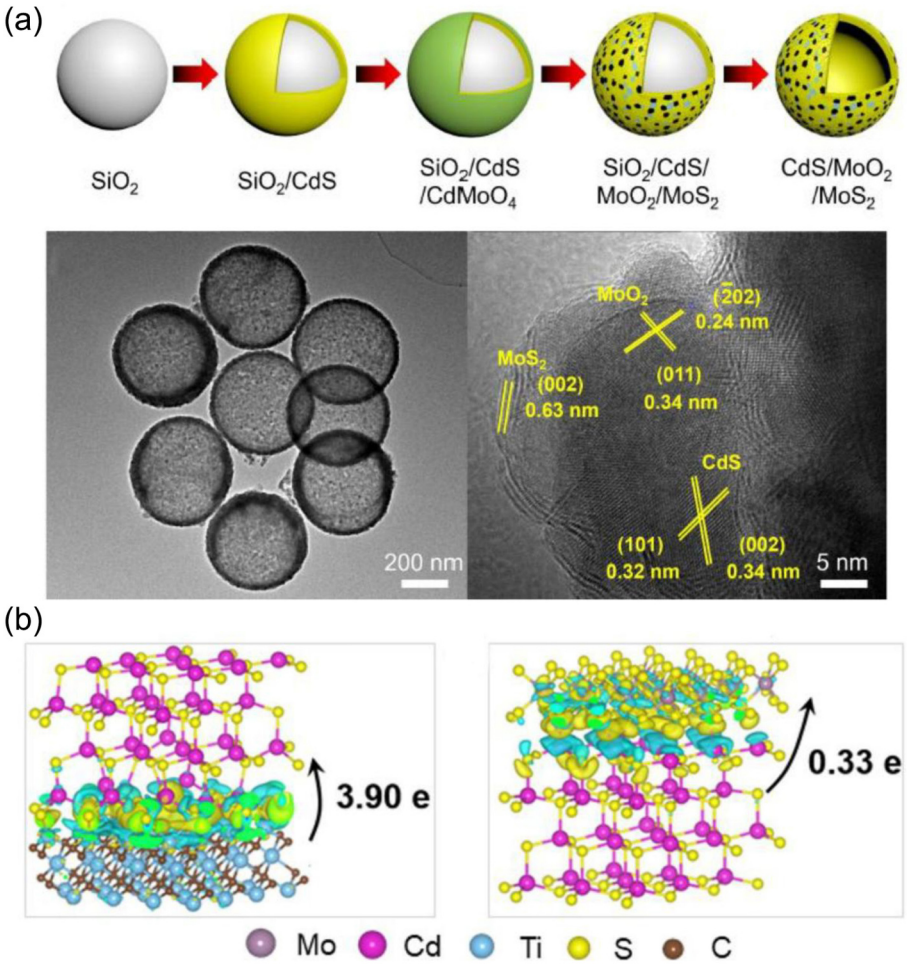

Fig. 9 (a) Schematic diagram of synthesis process and TEM images of $CdS/MoO_2/MoS_2$. Reproduced with permission from Ref. [154], © Wiley-VCH GmbH 2025. (b) Bader electron transfer at CdS/Ti_3C_2 and CdS/MoS_2 interfaces. Reproduced with permission from Ref. [50], © Elsevier B.V. 2023.

(NIR) light, reaching 14.05 $\mu mol \cdot g^{-1} \cdot h^{-1}$. As illustrated in Figs. 10(c) and 10(d), the LSPR effect generated by WO_{3-x} QDs containing oxygen vacancy defects successfully broadened the photoresponse of the photocatalysts to the NIR region (800–1500 nm). DFT calculations and Kelvin probe force microscopy (KPFM) characterization revealed the facilitation of charge separation by the interfacial electric field (IEF). This study provided new ideas for designing photocatalytic systems with NIR responses. The hollow tubular structure has unique advantages in photocatalysis by enhancing light trapping capability through multiple light scattering/reflection and shortening carrier transport paths. As displayed in Fig. 10(e), the unique 3D hierarchical hollow tubular design of g-C_3N_4/ZIS (HTCN/ZIS) combined with the charge separation advantage of the type-II heterojunction realized highly efficient photocatalytic H_2 production with an apparent quantum efficiency (AQE) of 7.5% (420 nm) [164].

3.2 Transition metal oxides

Metal oxides have a long-standing research history in the field of photocatalysis [32]. Endowed with excellent chemical stability, low preparation cost, and straightforward synthesis processes, they have emerged as highly promising candidate materials for advancing solar H_2 production technology toward practical applications [195–197]. Among them, transition metal oxides, featuring unique advantages, such as variable oxidation states, flexible electron transfer capability, and diverse crystal structures, are frequently employed as photocatalyst hosts, cocatalysts, or carriers of composite photocatalysts [198–200]. Through modification strategies, including doping and heterojunction construction, the core photocatalytic properties, such as light absorption range and charge carrier separation efficiency, can be precisely regulated, thereby further expanding their application prospects in the field of solar H_2 production [201–203]. Typical representatives with the widest applications include TiO_2, MnO, CoO, CuO, and ZnO [8,166,167,170,172].

3.2.1 *TiO_2*

Since Fujishima and Honda first reported the photocatalytic water splitting performance of TiO_2 in 1972, TiO_2 has gained extensive research in the field of photocatalytic green H_2 production, owing to its high thermal stability, excellent resistance to photocorrosion, and matching thermodynamic characteristics for water-splitting reactions [32,39]. Zhang *et al.* [39] adopted advanced gliding arc plasma (GAP) technology to rapidly synthesize high-crystalline mesoporous TiO_2 homojunctions in one step without the need for a template. As shown in Fig. 11(a), the sample contained an anatase phase (80%) and a rutile phase (20%), and the two crystal phases were closely combined at the interface. The built-in electric field formed by the bandgap difference (Fig. 11(b)) effectively drove the directional migration of photogenerated electrons and holes, reducing the recombination of photogenerated carriers. During the synthesis process, the size of TiO_2 nanoparticles decreased from 56 to 15 nm with increasing gas flow rate, the morphology changed from spherical to irregular, and the specific

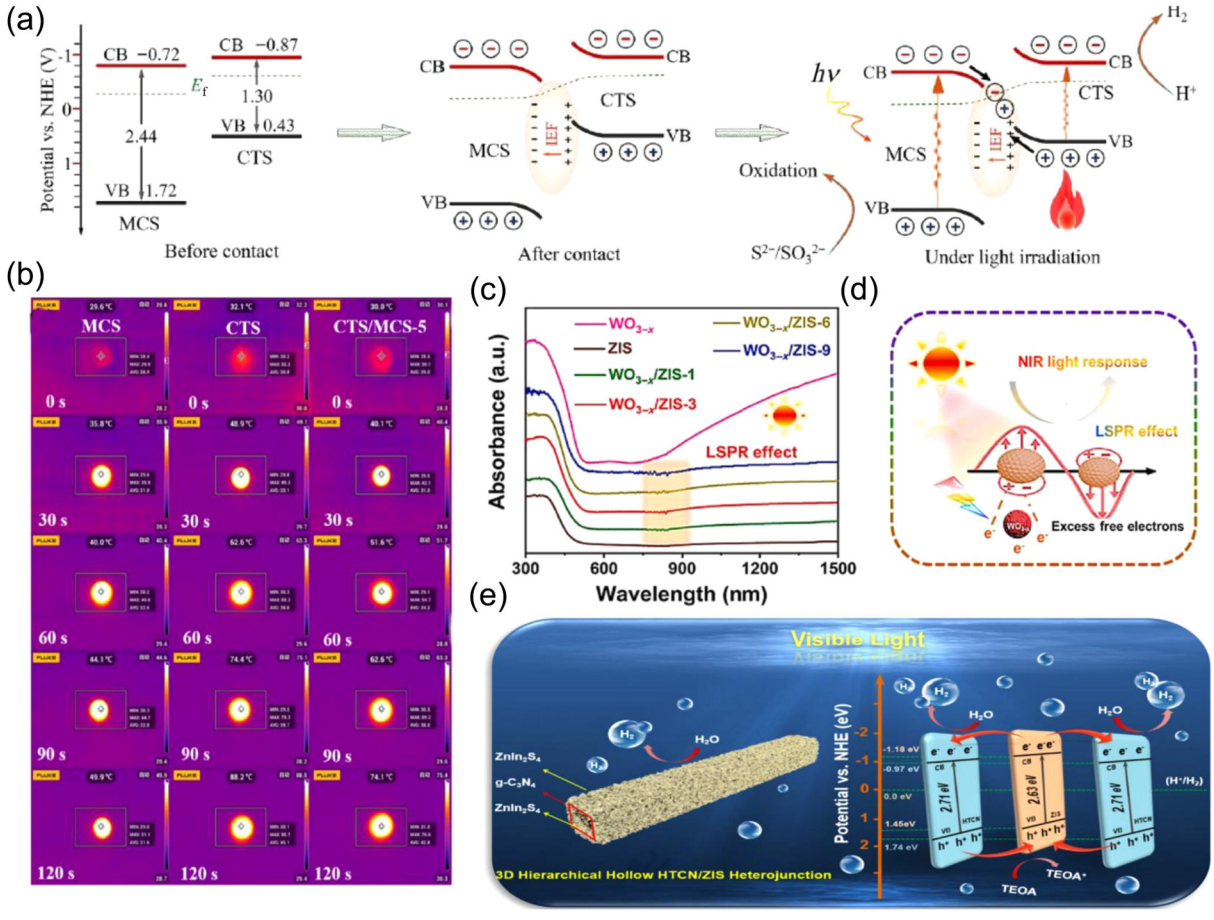

Fig. 10 (a) Charge transfer path of S-type heterojunction CTS/MCS. (b) Infrared thermographic image. Reproduced with permission from Ref. [37], © Elsevier Inc. 2024. (c) Absorption spectra of samples; (d) schematic diagram of NIR light-responsive behavior of WO_{3-x} QDs achieved through the LSPR effect. Reproduced with permission from Ref. [163], © Elsevier Inc. 2024. (e) Mechanism of HTCN/ZIS for photocatalytic H_2 evolution. Reproduced with permission from Ref. [164], © Elsevier Inc. 2021.

surface area grew from 30 to 98 $m^2 \cdot g^{-1}$. The optimization of mass transfer and the improvement of photogenerated carrier separation efficiency enabled a significant enhancement of the photocatalytic H_2 production performance. Researchers have investigated the influence of piezoelectric potential changes on the photocatalytic performance of TiO_2 by combining quartz with TiO_2 [43]. It was found that the piezoelectric potential varied with the microstructure and was significantly enhanced when the quartz grain size increased. The ultrasonic power was also positively correlated with the piezoelectric potential strength. The weak piezoelectric potential caused the CB of TiO_2 to tilt upward, promoting charge separation and enhancing the reduction ability of electrons, while the strong piezoelectric potential led to an excessive downward curvature of CB, weakening the reduction ability of electrons. The "piezoelectric switches" were designed to regulate the performance of photocatalytic H_2 production, which was achieved by adjusting the shape and size of piezoelectric materials or ultrasonic power to precisely control the piezoelectric potential. The research revealed that Pt-C/TiO_2 exhibited superior H_2 production performance under simulated sunlight compared to visible light, which was ascribed to the fact that the photocatalyst excited by ultraviolet light generates more photogenerated electrons [69]. Meanwhile, the surface of Pt-C/TiO_2 retained a part of Ti^{2+}/Ti^{3+}, and the surface oxygen vacancies acted as electron traps, favoring charge separation. However, as depicted in Fig. 11(c), incident light with strong energy can cause the oxidation of the carbon layer to produce O–C=O and C–O and oxidize the sacrificial agent 2-propanol to form propionic acid. The coverage of propionic acid on the surface of the active sites significantly reduced the stability of Pt-C/TiO_2. In contrast, using visible light as the light source sacrificed part of the photocatalytic activity of Pt-C/TiO_2 but improved its stability. Li *et al.* [166] prepared mesoporous black TiO_2 (b-TiO_2) with visible light-responsive properties by hydrogenation treatment. Hierarchical tandem heterojunctions were constructed by vertically growing MoS_2 nanosheets and loading Cu_2S nanoparticles with b-TiO_2 as the substrate. The vertically grown MoS_2 exposed a large number of edge-active sites and effectively facilitated charge transfer as an electron transport bridge. The Cu_2S with a near-infrared photothermal effect increased the temperature of the reaction system to 58.2 °C, and the heightened temperature accelerated the reaction kinetics. The layered heterostructure of b-TiO_2/MoS_2/Cu_2S utilized the synergistic effects of light absorption extension, electron transport bridge, and photothermal action, resulting in a 16-fold enhancement of the photocatalytic H_2 production performance compared to b-TiO_2.

Guo *et al.* [8] constructed a gas-solid biphasic photocatalytic system (water steam/catalyst/hydrogen) by spin-coating photocatalysts onto carbonized pinewood substrates. Compared with the traditional gas-liquid-solid triphasic system (liquid water/photocatalyst/hydrogen), the biphasic system facilitated sufficient contact between water molecules and photocatalysts (Fig. 12(a)). Notably, the adsorption free energy of water molecules in the gas phase (−0.212 eV) was significantly lower than that in the liquid phase (0.331 eV). Additionally, the diffusion coefficient of generated H_2 in the gas phase (2.65×

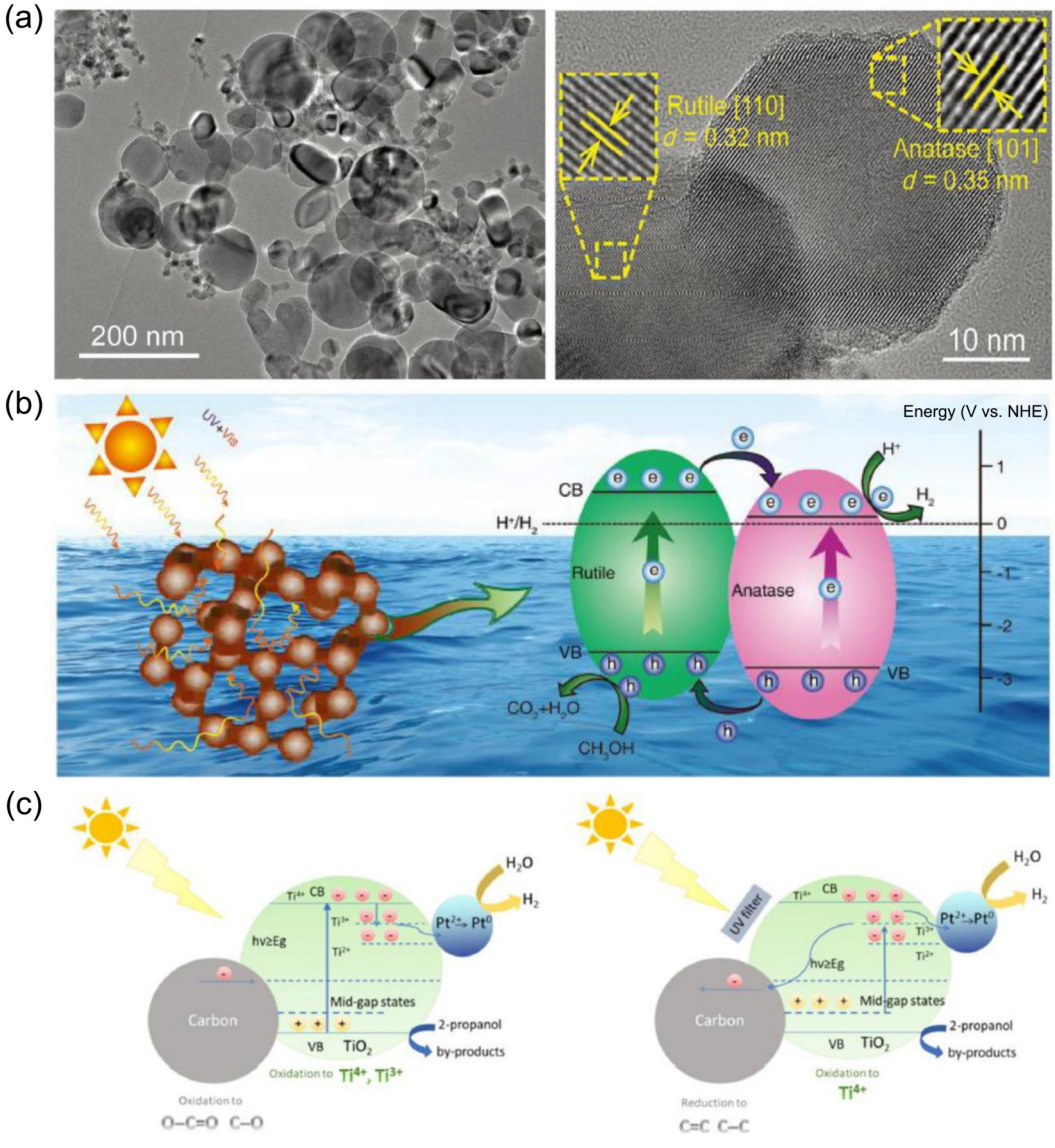

Fig. 11 (a) TEM images and (b) schematic diagram of photocatalytic H_2 generation for TiO_2 homojunctions. Reproduced with permission from Ref. [39], © Wiley-VCH GmbH 2025. (c) Reaction mechanisms of charge transfer and H_2 generation in Pt-C/TiO_2 under simulated sunlight (left) and visible light (right) conditions. Reproduced with permission from Ref. [69], © Elsevier Ltd. 2024.

10^{-3} $m^2 \cdot s^{-1}$) was markedly higher than that in the liquid phase (5×10^{-5} $m^2 \cdot s^{-1}$), which effectively reduced the resistance of gas escape, thereby enabling superior photocatalytic performance for H_2 production. Furthermore, as illustrated in Fig. 12(b), the multichannel structure of carbonized pinewood effectively immobilized the catalyst particles and prevented agglomeration to adequately expose active sites. Remarkably, as a substrate, the unique photothermal effect of carbonized pinewood improved the photocatalytic H_2 production performance by promoting the kinetic process of the photocatalytic reaction and the formation of water vapor (Fig. 12(c)). The experimental results confirmed the universal applicability of this biphasic system for photocatalytic H_2 production. For example, CoO, MoS_2, C_3N_4, TiO_2, and CuS-MoS_2 all exhibited excellent photocatalytic H_2 production performance in this system (Fig. 12(d)).

3.2.2 *MnO*

Compared with TiO_2, MnO is a typical narrow-bandgap TMO with a bandgap width of 1.0–2.0 eV [28,167,204,205]. This characteristic enables it to efficiently capture the visible light region, which accounts for approximately 43% of the solar spectrum, successfully overcoming the inherent limitation of traditional wide-bandgap TMOs that can only respond to ultraviolet light, thereby significantly improving the solar energy utilization efficiency. In addition, MnO possesses a higher electron mobility than TiO_2, and its unique Mn^{2+}/Mn^{3+} redox pairs endow it with abundant surface catalytically active sites, which can effectively reduce the activation energy of the photocatalytic water-splitting reaction for H_2 production and promote charge transfer [167,206]. Based on the aforementioned advantages, MnO demonstrates irreplaceable and distinctive competitiveness in the field of photocatalytic green H_2 production. The *in situ* synthesized heterojunction features an intimate interfacial contact, which not only enhances charge transport and separation but also avoids the agglomeration typically induced during the combination of individual photocatalyst components. Wang *et al.* [28] synthesized a Co/MnO Ohmic junction in one step by directly calcinating the bimetallic precursor MnCo-PBA under an inert atmosphere. Subsequently, graphdiyne (GDY) was introduced via physical stirring to construct the Co/MnO/GDY

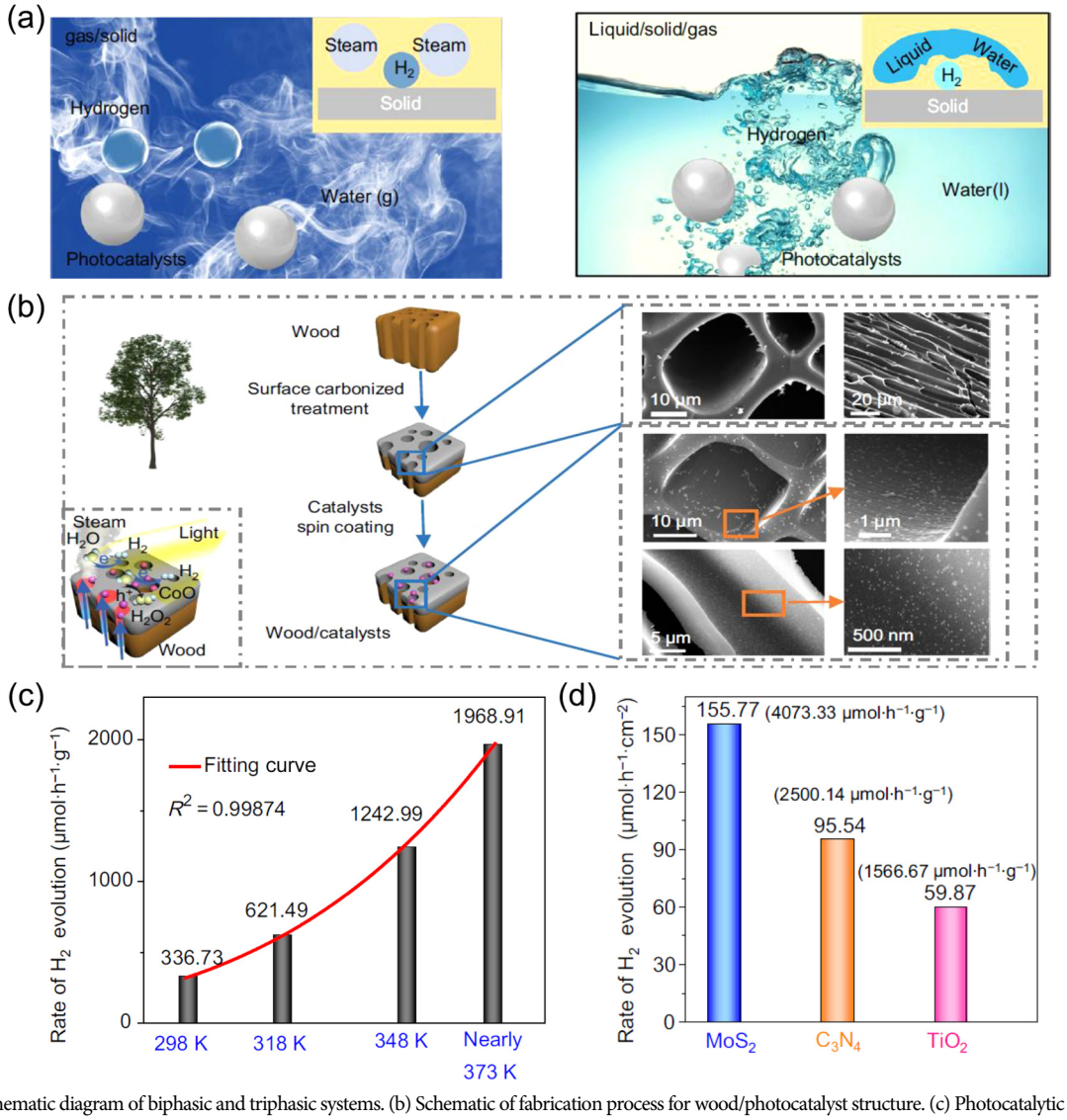

Fig. 12 (a) Schematic diagram of biphasic and triphasic systems. (b) Schematic of fabrication process for wood/photocatalyst structure. (c) Photocatalytic H_2 production efficiency of CoO NPs as a function of reaction temperature. (d) H_2 evolution rates of wood/MoS_2, wood/C_3N_4, and wood/TiO_2 systems. Reproduced with permission from Ref. [8], © The Author(s) 2021.

composite catalyst. As shown in Fig. 13(a), DFT calculations revealed that the work functions (Φ) of GDY, MnO, and Co were 5.74, 5.61, and 4.87 eV, respectively. After contact, the E_F at the interface tended to equilibrate, resulting in electron transfer from the side with a higher E_F to the side with a lower E_F. Under nonillumination conditions, electrons transferred from Co to MnO at the interface, forming an ohmic junction. At the GDY/MnO interface, electrons transferred from MnO to GDY, resulting in upward band bending of MnO and downward band bending of GDY, thereby generating a built-in electric field oriented from MnO to GDY. Under illumination, the photogenerated charges followed a Z-scheme transfer pathway driven by this built-in electric field, as illustrated in Fig. 13(c). As shown in Fig. 13(b), *in situ* XPS characterization indicated that the binding energies of O 1s and Mn 2p decreased under illumination, while that of C 1s increased, suggesting that MnO gained electrons and GDY lost electrons under light. These observations aligned with the direction of photogenerated electron transfer illustrated in Fig. 13(b). Cu/Zn heterojunctions were synthesized *in situ* by high-temperature calcination of Cu/Zn bimetallic organic frameworks. Hu *et al.* [167] employed a one-step salt-assisted thermal polymerization process to synthesize p-type MnO semiconductors *in situ* on the surface of n-type crystalline carbon nitride (CCN), successfully constructing an S-scheme p-n heterojunction photocatalyst (MCN). This innovation enables the synergistic utilization of photogenerated electrons and holes, simultaneously achieving clean energy production and oxidative organic synthesis. Through its unique band structure design, MCN retains the strong redox capability of photogenerated charges, while the built-in interfacial electric field breaks the Coulomb interaction between MnO and CCN, significantly promoting the efficient separation of photogenerated carriers. Specifically, CCN serves as the reduction semiconductor responsible for proton reduction to produce H_2, while MnO functions as the oxidation semiconductor to catalyze alcohol oxidation, realizing the spatial separation of reduction and oxidation reactions. Under visible light irradiation, the photocatalytic H_2 evolution efficiency of MCN reaches 7 times that of pure CCN, and it efficiently and selectively converts benzyl alcohol to benzaldehyde, demonstrating excellent catalytic activity and reaction selectivity.

3.2.3 *ZnO*

The electron mobility of ZnO is significantly superior to that of

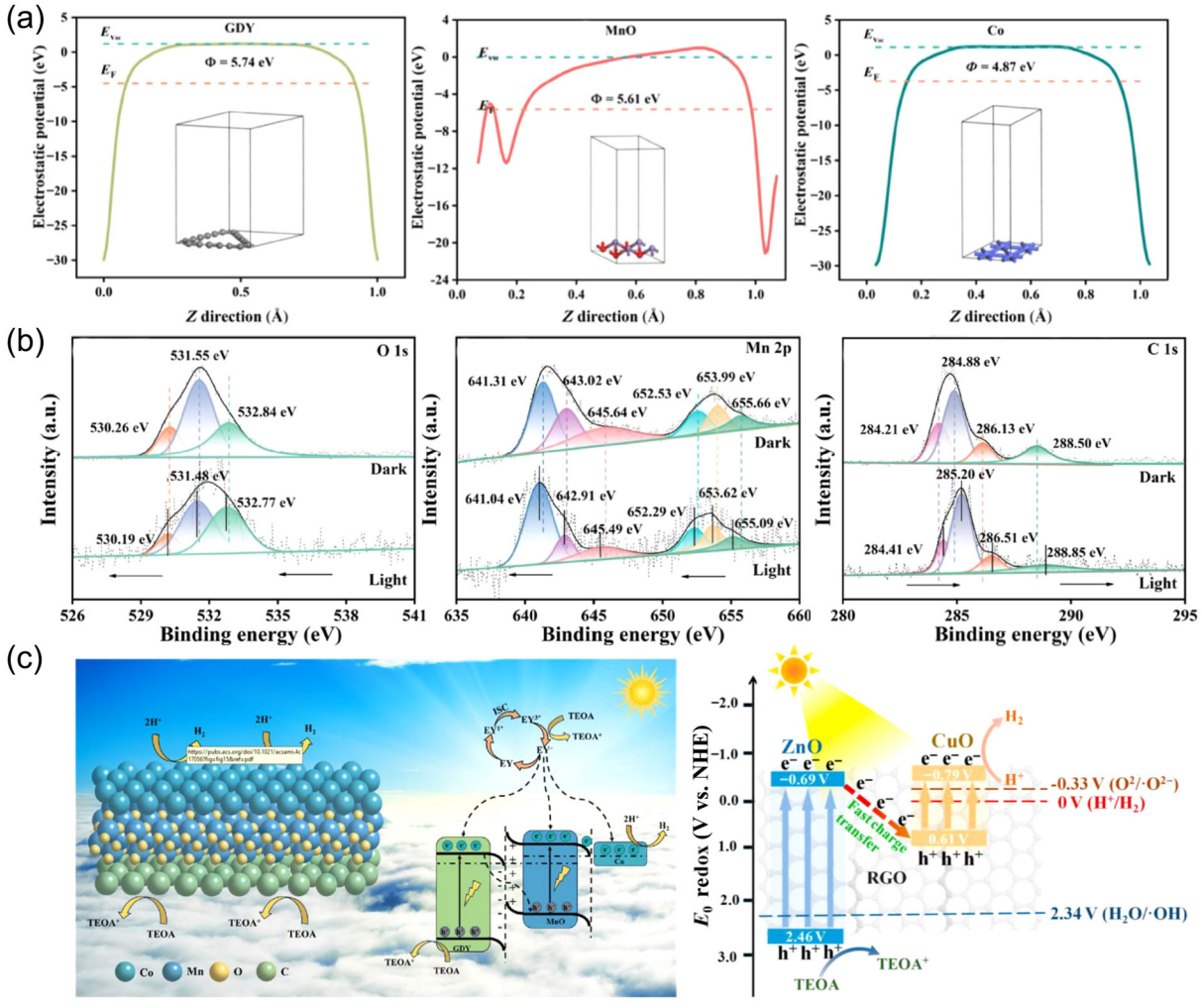

Fig. 13 (a) Work functions of GDY, MnO, and Co. (b) High-resolution XPS spectra of O 1s, Mn 2p, and C 1s. (c) Schematic diagram of photocatalytic H_2 generation for Co/MnO/GDY and RGO/CuO–ZnO. Reproduced with permission from Ref. [28], © American Chemical Society 2025. Reproduced with permission from Ref. [207], © American Chemical Society 2025.

TiO_2 and MnO. The efficient electron transport property directly accelerates the migration of photogenerated carriers, providing kinetic support for photocatalytic reactions [171,206]. However, as a typical wide-bandgap TMO, ZnO has a bandgap width of 3.30–3.38 eV and a high free exciton binding energy of 60 meV [171]. These characteristics limit its response only to ultraviolet light, which accounts for less than 5% of solar energy, restricting its light-harvesting range. Meanwhile, the high recombination rate of photogenerated carriers severely constrains the improvement of photocatalytic activity. Studies have confirmed that introducing oxygen vacancies into the ZnO lattice via an annealing process can effectively narrow the bandgap and construct charge trapping sites, thereby enhancing the visible light absorption and carrier separation efficiency and significantly optimizing photocatalytic performance [170–172]. Innovatively, an *in situ* sulfidation method based on ion-by-ion growth mechanisms was employed to grow ZnS directly on the ZnO surface, thereby constructing the ZnO–ZnS heterojunction [170,171]. This strategy not only preserves the original crystal structure of ZnO but also avoids the common lattice mismatch problem in traditional heterojunction preparation. While reducing the interfacial charge migration impedance, it effectively suppresses the recombination of photogenerated carriers by forming Type-II or S-scheme charge transfer pathways, providing an efficient and feasible modification approach for performance breakthroughs of ZnO-based photocatalysts. Xie *et al.* [170] successfully synthesized oxygen vacancy-rich ZnO–ZnS hollow porous spheres (Ov-ZOS) by optimizing the calcination process combined with a template approach. The unique structure can enhance photon harvesting through multiple refractions and scattering of light and synergize with the narrow-bandgap effect induced by oxygen vacancies to significantly improve light absorption performance. Consequently, the photocatalytic H_2 evolution activity of Ov-ZOS is notably superior to that of ZnO–ZnS nanosheets. However, the ZnS on the outer layer of ZnO is directly exposed to the reaction solution, where S^{2-} in its lattice is easily oxidized by photogenerated holes, triggering photocorrosion that severely impairs the long-term cycling stability of photocatalysts. Different from the aforementioned strategy, Lu *et al.* [172] designed and synthesized a core–shell heterojunction ZnO@ZnS (ZnS as the core and ZnO as the shell) rich in Zn, S, and O vacancies using a metal–organic coordination polymer as the template. The ZnO shell layer effectively isolates the reaction environment and inhibits the photocorrosion of the ZnS core, thereby enhancing the stability of ZnO@ZnS. In addition, the synergistic effect of multiple vacancies and heterojunctions simultaneously achieves the dual goals of efficient photocatalytic H_2 production and degradation of oxytetracycline in seawater. Chen *et al.* [207] synthesized an *in situ* Cu/Zn-bimetallic organic framework on reduced graphene oxide (RGO), which was subsequently calcined to obtain the

RGO/CuO–ZnO heterojunction. Serving as a channel for fast electron transport, RGO effectively promoted charge transfer and separation while enhancing the light absorption capability of the photocatalyst. As shown in Fig. 11(c), benefiting from the synergistic effects of the Z-scheme charge transfer pathway and RGO, the RGO/CuO–ZnO heterojunction achieved an AQE of 8.96% at 420 nm even without loading noble metal cocatalysts.

3.3 Carbon nitrides

$g\text{-}C_3N_4$ is a highly representative metal-free polymeric semiconductor photocatalyst. It was prepared from inexpensive and readily available nitrogen-containing compounds such as melamine and urea through a simple thermal polymerization process [127,208]. The core structure is composed of a conjugated framework formed by triazine or heptazine rings [209,210]. As a typical two-dimensional material, it exhibits a graphite-like layered structure, with the layers connected by weak van der Waals forces. This characteristic endows it with a potentially high specific surface area, providing abundant active sites for photocatalytic reactions [211,212]. Moreover, $g\text{-}C_3N_4$ possesses prominent advantages, such as nontoxicity, environmental friendliness, excellent chemical stability, low preparation cost, and intrinsic visible light response. It is widely regarded as a highly promising green photocatalytic material [213–215]. However, pure $g\text{-}C_3N_4$ exhibits a significant drawback of low electrical conductivity, resulting in poor transport efficiency of photogenerated carriers and a tendency toward charge recombination. Additionally, it tends to induce a light-shielding effect in aqueous solutions, thereby limiting its photocatalytic performance [110,216,217]. To overcome these bottlenecks, various modification strategies have been widely employed, among which cocatalyst loading and heterostructure construction represent two of the most commonly used and highly effective approaches [40,54,174,218,219].

3.3.1 *Cocatalyst loading*

Cocatalyst loading can reduce the activation energy of the reaction and promote the separation of photogenerated carriers, which is an effective strategy to enhance the photocatalytic performance of $g\text{-}C_3N_4$. Shi *et al.* [42] synthesized the nonmetallic cocatalyst $NiCS_3$ by a precipitation method and combined it with $g\text{-}C_3N_4$. As shown in Fig. 14(a), DFT calculations revealed that the C sites in $NiCS_3$ possessed an excellent ΔG_{H^*} (0.195 eV) as the active site for photocatalytic H_2 production, indicating that H^+ preferentially adsorbs and undergoes activation at the C sites. The distribution of charge density (Fig. 14(a)) demonstrated that the $g\text{-}C_3N_4$ layer at the heterogeneous interface acted as an electron depletion layer,

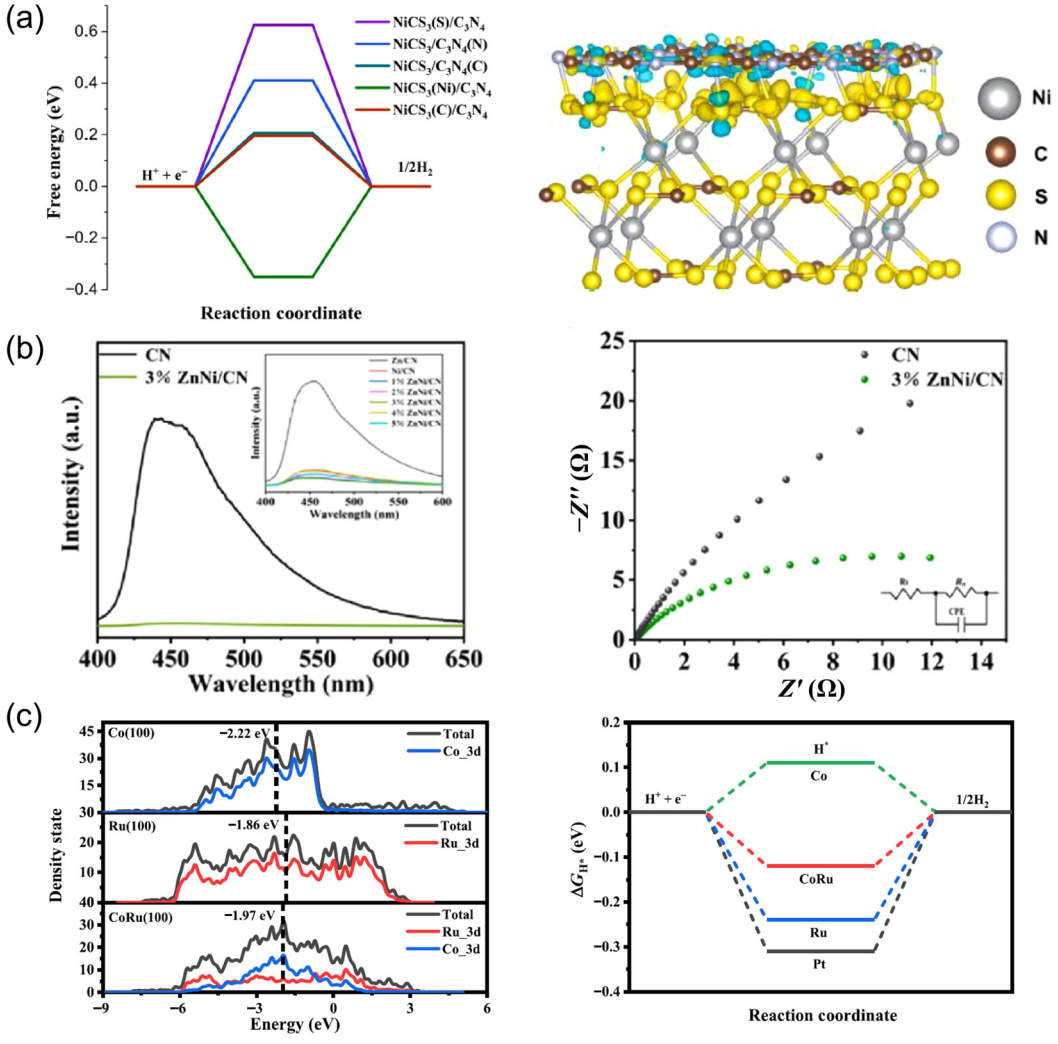

Fig. 14 (a) ΔG_{H^*} and calculated charge density difference of $NiCS_3/g\text{-}C_3N_4$ (yellow and blue represent electron accumulation and depletion, respectively). Reproduced with permission from Ref. [42], © Elsevier Inc. 2024. (b) Curves of PL and EIS. Reproduced with permission from Ref. [73], © Hydrogen Energy Publications LLC. 2024. (c) d-band centers and ΔG_{H^*}. Reproduced with permission from Ref. [220], © Elsevier B.V. 2024.

while the $NiCS_3$ layer served as an electron accumulation layer to receive electrons and further reduce adsorbed H^+ at the C sites, thereby generating H_2. Sun *et al.* [73] prepared a bimetallic ZnNi cocatalyst by the chemical reduction method. Through optimization of the loading amount, 3% ZnNi/CN exhibited the highest performance of photocatalytic H_2 evolution, achieving 1822.75 $\mu mol \cdot g^{-1} \cdot h^{-1}$, which was superior to the modification of single-metal cocatalysts (Zn/CN, Ni/CN). The loading of the bimetallic ZnNi cocatalyst reduced the bandgap of the photocatalyst from 2.87 to 2.80 eV, effectively broadening the range of light absorption and simultaneously supplying more active sites for the photocatalytic reaction. As depicted in Fig. 14(b), photoluminescence (PL) spectroscopy and electrochemical impedance spectroscopy (EIS) confirmed that the charge separation efficiency of 3% ZnNi/CN exhibited a significant improvement compared with that of CN. Similarly, Li *et al.* [220] prepared the composite photocatalyst CoRu/TCN by loading CoRu nanosheets on tubular g-C_3N_4 (TCN). The Schottky barrier between CoRu and TCN impeded the electron backflow from CoRu to TCN, which significantly enhanced the charge separation efficiency. As displayed in Fig. 14(c), the calculated d-band center clearly illustrates the interaction between reaction intermediates and metal active sites. Compared to Co, the d-band center of Ru was closer to E_F, indicating that Ru sites were more favorable for hydrogen adsorption. Consequently, after alloying Co and Ru, CoRu exhibited an optimized d-band center position, which balanced hydrogen adsorption and desorption. Furthermore, compared to Co, Ru, and Pt, CoRu showed a ΔG_{H^*} closer to zero (Fig. 14(c)), corresponding to an optimal hydrogen binding energy. Ultimately, the photocatalytic H_2 evolution efficiency of CoRu/TCN reached 1601.32 $\mu mol \cdot g^{-1} \cdot h^{-1}$, surpassing that of Pt/TCN (1271.32 $\mu mol \cdot g^{-1} \cdot h^{-1}$). Lu *et al.* [54] prepared CDs/TCN by loading carbon dots (CDs) on TCN. The unique hollow tubular structure of TCN enhanced the light absorption property through multiple scattering and reflection of photons. The photothermal effect of CDs was utilized to reduce the reaction activation energy and promote the reaction kinetics through the local temperature increase. Meanwhile, CDs as electron traps effectively promoted photogenerated charge separation.

3.3.2 *Construction of heterojunctions*

The construction of heterojunctions, which can further suppress charge recombination and broaden the light absorption range through bandgap matching and interfacial electric field regulation, represents a core strategy for optimizing the photocatalytic performance of g-C_3N_4. Wu *et al.* [221] prepared CoAl-LDH/Cv-CN heterojunctions by electrostatic self-assembly, combining CoAl-LDH with g-C_3N_4 containing carbon vacancies (Cv-CN). The carbon vacancies introduced intermediate energy levels in g-C_3N_4 to optimize the energy band structure (Figs. 15(a) and 15(b)) and extend the light absorption performance. Meanwhile, as an electronic trap, the capture of electrons by carbon vacancies facilitated the separation of charges. Additionally, the layered structure of CoAl-LDH offered plentiful active sites for the reaction. The staggered band structure of CoAl-LDH and Cv-CN formed a Z-scheme charge transfer path, which not only facilitated charge separation but also preserved the strong redox capacity of photogenerated charges. The tetracycline degradation efficiency of 30% CoAl-LDH/70% Cv-CN (CCN-2) reached 93.1% with a H_2 production rate of 2515 $\mu mol \cdot g^{-1}$. The thermal treatment of g-C_3N_4 with ammonium carbonate can introduce abundant carbon vacancies and pore structures [222]. Carbon vacancies improve the photocatalytic performance by modulating the electronic structure of g-C_3N_4 and introducing defect energy levels. The optimization of the energy band structure and the increase in the specific surface area improved the photocatalytic H_2 production performance of g-C_3N_4 by 1.54 times. Gu *et al.* [174] modified the surface of g-C_3N_4 using the phosphate group of amino tris (methylene phosphonic acid) (ATMP), which engaged with water molecules through hydrogen bonds and accelerated the migration of H^+ to the active sites. Meanwhile, as shown in Figs. 15(c) and 15(d), the phosphorylation (CN-P) led to a space charge density separation of the highest occupied molecular orbital and lowest unoccupied molecular orbital (HOMO-LUMO), effectively inhibiting the recombination of charge. Moreover, after phosphorylation, the bandgap of g-C_3N_4 was reduced from 2.65 to 2.51 eV, and the light-absorbing ability was obviously enhanced. After optimization, the photocatalytic H_2 production performance of g-C_3N_4 under visible light reached 976.7 $\mu mol \cdot g^{-1} \cdot h^{-1}$. Wang *et al.* [40] achieved K^+ doping and material nanofabrication using a salt (KCl)-assisted method. K^+ doping caused the CB of g-C_3N_4 to shift negatively by −1.32 eV, enhancing the reduction property of electrons. Moreover, the contact angle of g-C_3N_4 decreased from 54.7° to 18.6°, and the significant enhancement of hydrophilicity improved the dispersibility of g-C_3N_4 in water. The nanosized g-C_3N_4 exposed more edge-active sites, resulting in a significant enhancement of photocatalytic H_2 production performance.

3.4 Perovskite materials

Perovskite materials, with the general formula ABX_n (where A and B are cations with different radii, and X is an anion), have emerged as star materials in the field of green H_2 production via water splitting due to their unparalleled structural tunability [182,223,224]. By flexibly substituting the ions at sites A (e.g., Cs^+, La^{3+}), B (e.g., Ti^{4+}, Sn^{4+}), and X (e.g., O^{2-}, I^-), the bandgap, mobility efficiency of photoinduced carriers, and surface chemical property can be precisely regulated to optimize the photocatalytic performance [225–227]. Over the past decade, significant progress has been made in the research of perovskite-based photocatalysts, covering multiple aspects from the fundamental structure–property relationships to performance optimization strategies [228–230]. However, challenges such as the inherent instability of perovskite materials, limited carrier lifetime, and the presence of toxic components still restrict their large-scale application. According to the differences in anion types, perovskite photocatalysts for H_2 production are primarily categorized into oxide perovskites and halide perovskites.

3.4.1 *Oxide perovskites*

The oxide perovskites are characterized by the classic ABO_3 with O^{2-} as the X-site anion. Among them, lead-free oxide perovskite materials have emerged as important candidates in the field of photocatalysis due to their environmental friendliness, tunable band structure, efficient charge separation capability, and multifunctional catalytic activity [231–233]. $SrTiO_3$, a typical lead-free perovskite material, has attracted considerable interest in the field of photocatalytic H_2 production because of its excellent photostability [234,235]. However, the large bandgap of STO (3.3 eV) limits its photocatalytic performance, as it can only be excited by ultraviolet light. STO is composed of eight $[TiO_6]$ octahedra, with Ti^{4+} located at the center of $[TiO_6]$ to form a 3D octahedral network. Sr^{2+} fills the twelve coordination positions in the octahedral gaps, maintaining charge balance, and O^{2-} occupies the vertex positions of the octahedra. Among them, Ti^{4+} and Sr^{2+}

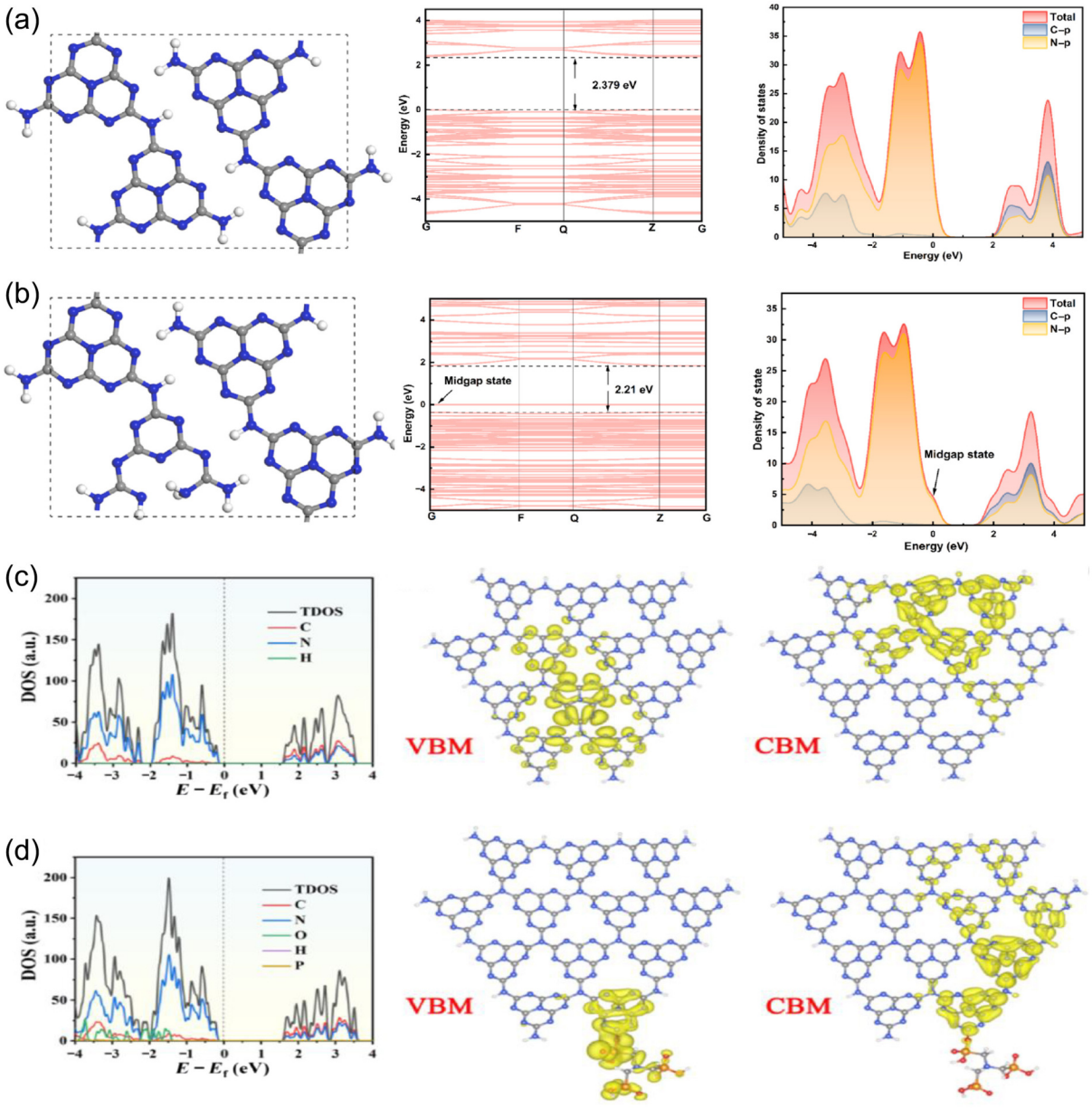

Fig. 15 Calculation model, energy band structure, and DOS for (a) g-C_3N_4 and (b) Cv-CN. Reproduced with permission from Ref. [221], © Elsevier 2024. DOS and electronic structure with corresponding charge distribution of CBM and VBM for (c) CN and (d) CN-P. Reproduced with permission from Ref. [174], © Elsevier 2024.

are easily replaced by other ions, so element doping is one of the common means to modify the photocatalytic activity of $SrTiO_3$ [236]. As displayed in Fig. 16(a), DFT calculations showed that Ag doping reduced the water decomposition energy of the (001) crystal plane to 5.74 kJ·mol^{-1} for STO (Ag-(001)-STO), which was 94% lower than that of undoped (001)-STO [180]. It is worth mentioning that water decomposition is a key step in H_2 production, but it does not proceed spontaneously ($\Delta G \approx$ 237 kJ·mol^{-1}). The calculated hydrogen generation Gibbs free energy of Ag-(001)-STO was −302 kJ·mol^{-1}, which proved that Ag doping made the standard half-reaction of H_2 generation in STO proceed spontaneously, offering promising application prospects. Jiang *et al.* [77] prepared the composite photocatalyst Pd-ASTO by loading Pd on Al-doped STO (ASTO). As shown in Fig. 16(b), the Φ of Pd (5.12 eV) was significantly greater than that of ASTO (4.43 eV). Therefore, after Pd and ASTO came into contact, the energy band of ASTO bent upward, forming a Schottky barrier at the interface. The Schottky barrier effectively enhanced the separation efficiency of photogenerated charges. After component optimization, the H_2 production efficiency of Pd-ASTO-1.5% increased to 1.43 mmol·g^{-1}·h^{-1}, which was 140 times that of ASTO. Liu *et al.* [76] prepared amorphous red phosphorus-modified STO (P/STO) by phosphorylating STO with NaH_2PO_2. As depicted in Fig. 16(c), compared with STO, the light absorption boundary of P/STO was broadened from 370 to 600 nm, and the light absorption ability was significantly enhanced. Meanwhile, the heterojunction effect facilitated charge separation, and the photocatalytic H_2 yield reached 80 μmol·h^{-1}.

3.4.2 *Halide perovskites*

Halide perovskites with halide ions (Cl^-, Br^-, and I^-) as the X-site component feature general formulas such as ABX_3, A_2BX_6, and $A_3B_2X_5$. Compared with oxide perovskites, halide perovskites exhibit better light absorption capabilities [237–240]. As shown in Fig. 17(a), Zhou *et al.* [182] synthesized an inorganic perovskite material Cs_2SnI_6 (PtSA/Cs_2SnI_6) with single-atom Pt-I_3 site

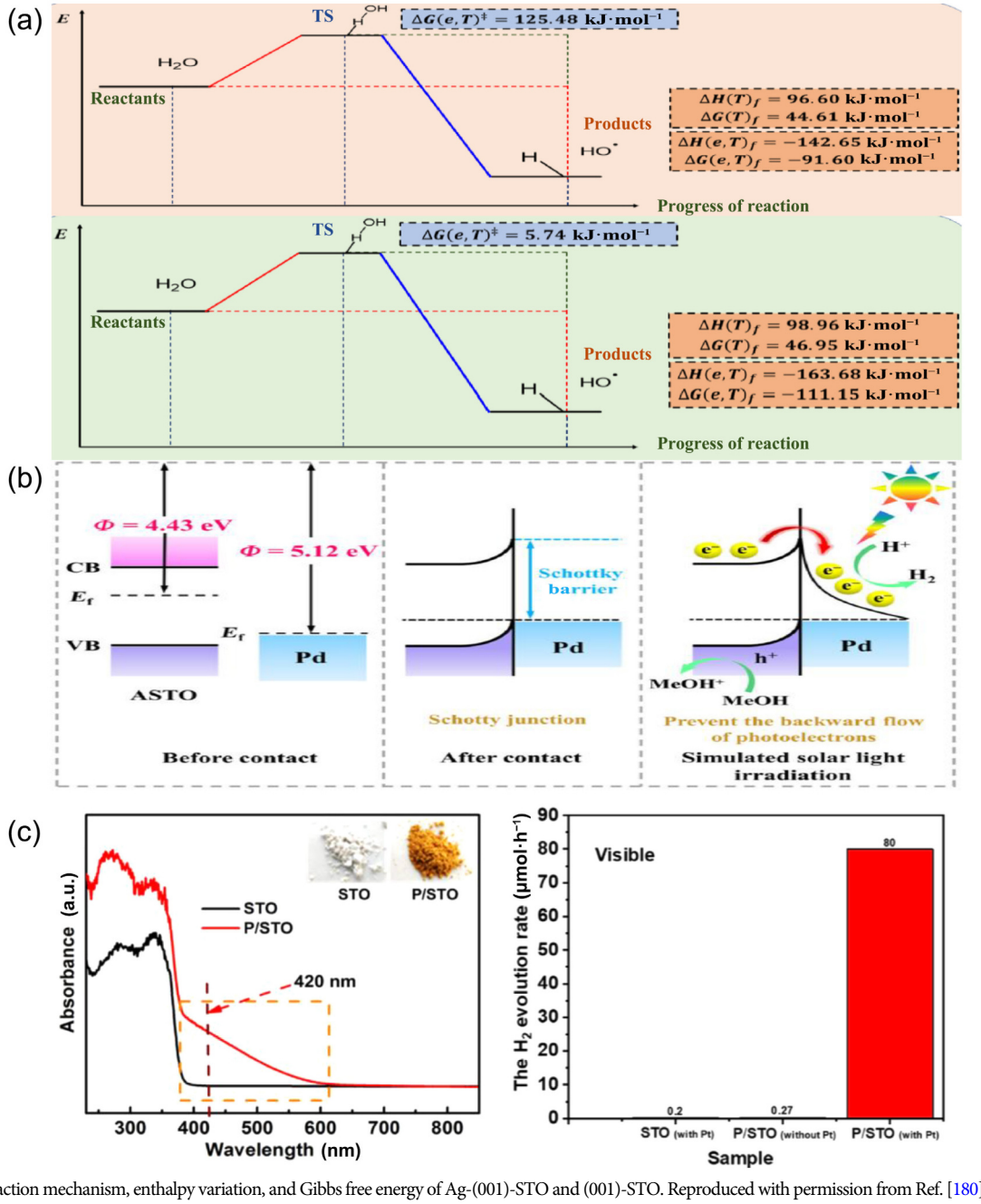

Fig. 16 (a) Reaction mechanism, enthalpy variation, and Gibbs free energy of Ag-(001)-STO and (001)-STO. Reproduced with permission from Ref. [180], © Hydrogen Energy Publications LLC 2024. (b) Energy band structure and charge transfer mechanism of Pd-ASTO. Reproduced with permission from Ref. [77], © Hydrogen Energy Publications LLC 2024. (c) Absorption spectra and photocatalytic H_2 production performance under visible light irradiation. Reproduced with permission from Ref. [76], © Hydrogen Energy Publications LLC. 2024.

modification by combining hydrothermal and impregnation methods, achieving efficient solar decomposition of HI for H_2 production. Compared with Cs_2SnI_6 loaded with Pt nanoparticles, PtSA/Cs_2SnI_6 benefited from strong interactions between single-atom Pt and Cs_2SnI_6, which promoted photogenerated charge separation and transfer, along with a significant reduction in the energy barrier for H_2 production. As a result, the photocatalytic H_2 production performance achieved a 176.5-fold enhancement and exhibited excellent cycling stability. Zhang *et al.* [181] prepared the inorganic bimetallic perovskite $Cs_6Cu_3AgBr_{10}$ and $Cs_3Cu_2Br_5$ through the cold crystallization method. The experiments demonstrated that the doping of Ag^+ reduced the bandgap value of $Cs_3Cu_2Br_5$. Correspondingly, the absorption edge extended from 344 to 380 nm (Fig. 17(b)). Additionally, the introduction of Ag^+ provided many new active sites for the reaction and decreased the exciton binding energy. Therefore, $Cs_6Cu_3AgBr_{10}$ exhibited excellent photocatalytic H_2 production performance of 14.64 μmol·h^{-1}. Fu *et al.* [184] successfully coupled photocatalytic H_2 evolution and O_2 evolution half-reactions using the I_3^-/I^- redox pair as an electron transfer bridge, achieving efficient production of H_2 and O_2 in stoichiometric ratios. This study innovatively constructed a dual-catalyst system, employing the halide perovskite PMA_2PbI_4 (PMA = $C_6H_5CH_2NH_2$) loaded with MoS_2 as the photocatalyst for H_2 evolution and RuO_x loaded with WO_3 as the photocatalyst for O_2 evolution. This design effectively overcomes the limitations of single narrow-bandgap photocatalysts in the light absorption range and redox capability, addressing the bottleneck of their inability to independently

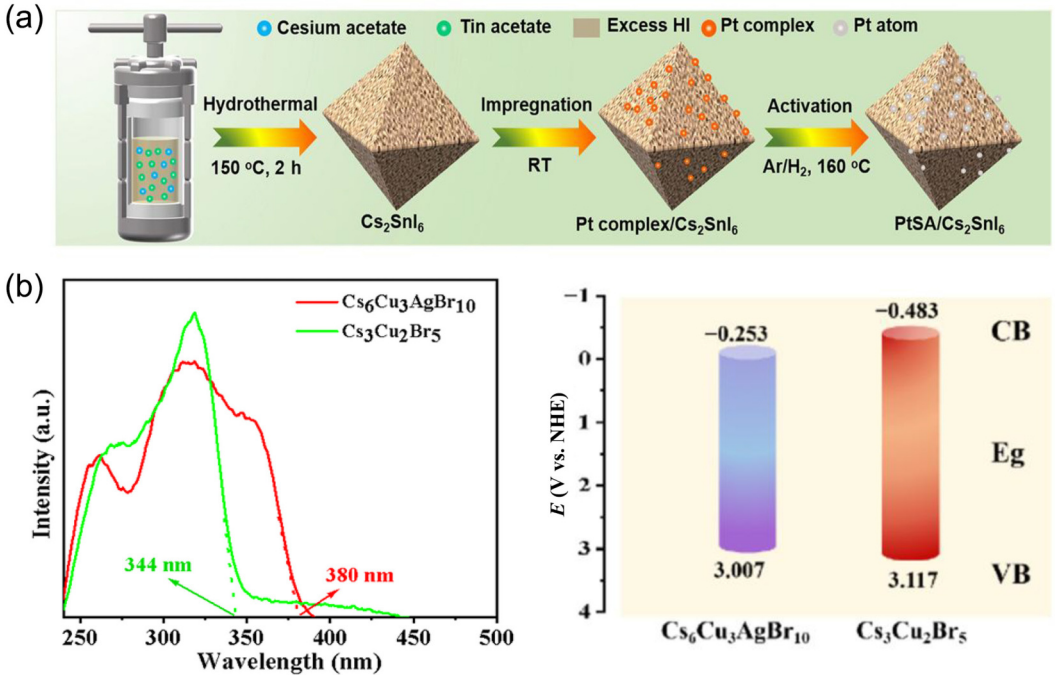

Fig. 17 (a) Schematic diagram of preparation process for PtSA/Cs_2SnI_6. Reproduced with permission from Ref. [182], © The Author(s) 2021. (b) Absorption spectra and energy band structure. Reproduced with permission from Ref. [181], © Elsevier B.V. 2024.

achieve complete water splitting. Ultimately, the system achieves an STH conversion efficiency of 2.07%. Guo *et al.* [185] systematically revealed the regulatory mechanism of alkali metal doping on the photocatalytic performance of metal halide perovskite materials. In this study, K^+ was doped into the $CsPbBr_3$ lattice by the anti-solvent precipitation method. It was clearly confirmed that as the doping content increased, the occupation position of K^+ in the lattice gradually changed from A-site substitution to interstitial doping. When the doping concentration of K^+ was optimized to 11.1% (A-site substitution), the photocatalytic H_2 production efficiency reached the optimum, which was 11 times that of pure $CsPbBr_3$. Similarly, A-site doping of other alkali metals, such as Li, Na, and Rb, also significantly improved the photocatalytic H_2 production performance. The experimental characterization combined with theoretical calculation results indicated that the lattice strain relaxation caused by A-site doping could significantly promote the charge transfer process and effectively regulate the band structure of $CsPbBr_3$, thereby enhancing its photocatalytic performance.

3.5 Others

MXenes are often employed as cocatalysts in photocatalysis due to their good electrical conductivity, large specific surface area, and abundant surface functional groups [57,74,241,242]. CdSe nanorods and Ti_3C_2 MXene nanosheets were combined to form the composite photocatalyst CdSe-MXene by a one-step hydrothermal method. Due to the difference in E_F, electrons flowed from CdSe to MXene at the interface, and the upward bending of the energy bands for CdSe effectively suppressed the electron backflow and promoted charge separation. Compared with CdSe, the photocatalytic H_2 production efficiency of CdSe-MXene achieved a 6-fold improvement. Similarly, Ti_3C_2 MXene is often applied to photocatalytic H_2 production by constructing Schottky heterojunctions with g-C_3N_4 [74,242]. Photocatalytic H_2 production efficiency increased from 393 to 2181 μmol·g^{-1} after the combination of protonated g-C_3N_4 and Ti_3C_2 MXene [242]. Kseniya O. Potapenko *et al.* [74] further investigated the influence of the types of terminal groups (–F, –O, and –OH) and sacrificial agents (triethanolamine, ethanol, and glucose) on the photocatalytic H_2 production efficiency of $Ti_3C_2T_x$/g-C_3N_4 composites.

Porous organic framework materials provide an efficient and sustainable solution for photocatalytic H_2 production through their unique structural tunability, high specific surface area, functionalization site design, and stability. Four benzotrithiophene-based covalent organic framework materials (BTT-COFs) with different conjugated structural units were designed and synthesized by Jeon *et al.* [178]. Experimental and computational results showed that the electron affinity and conjugation degree of building blocks had an important effect on the photocatalytic H_2 production performance. The electron affinity can characterize the ability of the active site to attract electrons. As shown in Fig. 18(a), the electron affinity of BTT-COFs increased with the number of aromatic rings. When the length of the aromatic rings was similar, the electron affinity depended on the degree of conjugation. Correspondingly, the photocatalytic performance gradually improved as the electron affinity increased. However, excessive electron affinity led to a decrease in the photocatalytic H_2 production efficiency. The experimental results demonstrated that a suitable electron affinity was conducive to the capture of electrons and inhibited charge recombination. However, when electrons are strongly immobilized at the active site, charge transport and transfer can be hindered, resulting in charge recombination and reducing the catalytic performance. Li *et al.* [22] innovatively designed novel metal-covalent organic framework (COF-Cu_3TG) materials using small-sized metal clusters and nitrogen-rich ligands. The small metal clusters effectively shortened the charge transport distance and increased the number of active sites for the reaction. By anchoring Ru atoms with nitrogen-rich organic ligands as nodes, a single-atom electronic bridge (N-Ru-N) structure was formed. This not only enhanced the light absorption of the catalysts but also promoted electron transfer between the layers, achieving improved photocatalytic performance. As displayed in Fig. 18(b), the

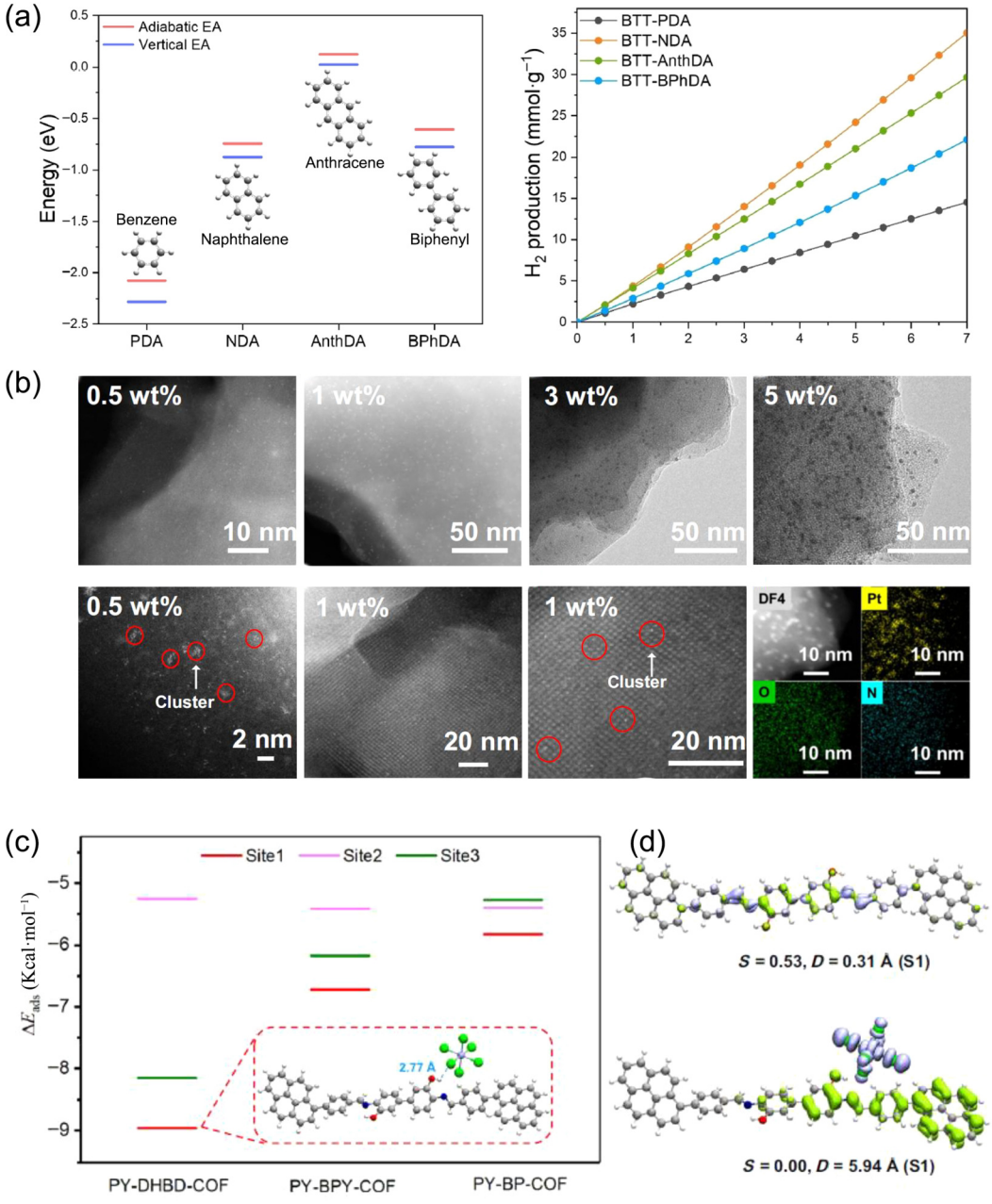

Fig. 18 (a) Calculated electron affinities and photocatalytic H_2 production performance. Reproduced with permission from Ref. [178], © Wiley-VCH GmbH 2022. (b) HR-TEM, HAADF-STEM, and EDX mapping images of PY-DHBD-COF loaded with Pt. (c) Adsorption energy of $PtCl_6^{2-}$. (d) Distribution of electrons and holes at site 1 for PY-DHBD-COF. Reproduced with permission from Ref. [243], © The Author(s) 2022.

introduction of hydroxyl and imine-N sites in the structural unit of the COF can achieve the precise adsorption of the Pt precursor ($PtCl_6^{2-}$) and the uniform deposition of highly dispersed Pt clusters [243]. The results of theoretical calculation (Fig. 18(c)) showed that the COF generated via the Schiff-base condensation reaction between 1,4-dihydroxybenzidine (DHBD) and 1,3,6,8-tetra(4-formylphenyl)pyrene (PY-CHO) (denoted as PY-DHBD-COF) had the lowest $PtCl_6^{2-}$ adsorption energy, with its adsorption sites localized around the hydroxyl and imine sites. From the hole and electron distribution diagram of site 1 (Fig. 18(d)), it can be found that PY-DHBD-COF-$PtCl_6^{2-}$ had a smaller S value and a larger D value, showing a stronger photogenerated charge separation ability. The S value represented the overlap integral of the hole and electron distribution, while the D value was the distance between the centers of holes and electrons. Benefiting from the introduction of hydroxyl and imine-N sites, PY-DHBD-COF exhibited excellent $PtCl_6^{2-}$ adsorption energy and charge separation efficiency, with a H_2 production rate as high as 42,432 μmol $g^{-1}·h^{-1}$ at 1 wt% Pt loading.

4 Conclusions and outlooks

This review systematically investigates the latest advances in the field of photocatalytic green H_2 production and provides in-depth analyses ranging from the design and synthesis of photocatalysts and the charge dynamics process of photogenerated carriers to the surface reaction mechanism. This highlights the critical role and great potential of photocatalytic technology in the energy transition. Photocatalytic green H_2 production, which exploits solar energy to drive the decomposition of water for H_2 generation, offers a promising solution to the energy crisis and

environmental challenges. It has the potential to restructure the global energy landscape and is one of the core technologies to achieve the goal of sustainable development.

The development of this field still faces the serious challenges of low efficiency, limited mass transfer and insufficient stability of photocatalysts. Currently, most photocatalysts have problems such as a narrow light absorption range and severe carrier recombination, which makes it difficult for the photocatalytic efficiency to meet the demands of industrialized large-scale production. The rational design of high-performance photocatalysts is the key to breaking through the above bottlenecks and achieving efficient solar energy conversion. Energy band engineering is a valid means to realize the precise regulation of photocatalysts [127]. The introduction of impurity energy levels through element doping constructs electron traps and promotes charge separation while extending the light absorption range by modulating the bandgap structure [160]. Compounding narrow bandgap semiconductors with wide bandgap semiconductors to create multicomponent heterojunctions, such as Type II and Type Z heterojunctions, not only retains the visible light absorption ability of narrow bandgap materials but also promotes carrier separation through interfacial charge transfer [8,128,170]. Loading metal quantum dots (such as Au and Ag) or semiconductor quantum dots (such as PbS) enhances visible light absorption through the LSPR effect, and at the same time, the band structure can be regulated through the quantum confinement effect to expand the light response range [11,115,116]. Upconversion materials that can convert long-wavelength infrared light into visible light are another powerful way to improve solar energy utilization [244]. Moreover, cocatalyst modification and the introduction of defects are key strategies to suppress carrier recombination [154,157,245]. Cocatalysts with high conductivity promote charge migration while acting as active sites to facilitate proton reduction [154,157]. The introduction of vacancies captures electrons and reduces their direct recombination with holes [245]. In the multiphase photocatalytic system, the low mass transfer efficiency between the reactants, products, and photocatalysts seriously hinders the rapid transfer of photogenerated carriers to reactants, which makes it difficult to increase the H_2 production rate. The design of innovative structures is crucial for promoting mass transfer. Low-dimensional structures such as nanowires and nanosheets can shorten the carrier migration path and reduce the probability of recombination in the bulk phase [246]. Meanwhile, a high specific surface area provides more active sites to accelerate the surface reaction. The core–shell structure, as a special composite structure, can simultaneously optimize key performance indicators such as light absorption, carrier separation, and stability through the cooperative effect between the core and shell layers, which is one of the important research directions in the future [247]. In addition, under actual reaction conditions, the photocatalyst is prone to being affected by photocorrosion, structural collapse, and toxicity, resulting in a dramatic decrease in photocatalytic activity with reaction time. This phenomenon is particularly prevalent in metal sulfide and perovskite-based photocatalytic materials [38,59,128,248]. To address this issue, the strategy of band structure modulation is commonly employed to accelerate the separation efficiency of photogenerated charges. This approach facilitates the rapid depletion of photogenerated holes, reducing their accumulation in both the bulk and surface of the photocatalyst. Consequently, it effectively suppresses the oxidative corrosion of photocatalysts and significantly enhances the photochemical stability of the materials. Surface passivation is an effective strategy for enhancing the stability of perovskite materials. By precisely modifying the surface and regulating the interface of perovskite materials, photoinduced phase separation and ion migration can be significantly suppressed, thereby greatly improving their photochemical stability and long-term cycling stability. Furthermore, cation doping can simultaneously enhance lattice rigidity and effectively regulate internal defect concentrations, thereby synergistically improving both the structural stability and photocatalytic stability of perovskite materials [249,250].

Photocatalytic water splitting for H_2 production often requires sacrificial agents to consume photogenerated holes and achieve efficient separation of photogenerated charges. The employment of sacrificial agents not only increases the cost of industrial applications but also pollutes the environment. In contrast, the overall water splitting system does not need to continuously replenish sacrificial agents and can be designed as a closed-loop system, facilitating integration and offering greater advantages in practical applications [251,252]. Photocatalysts with a suitable band structure can utilize photogenerated electrons and holes to simultaneously produce H_2 and O_2 with a specific stoichiometric ratio, achieving 100% atomic utilization efficiency. However, the overall water splitting reaction requires the simultaneous occurrence of oxidation and reduction half-reactions on the surface of the photocatalyst. In this case, photogenerated electrons and holes migrate to different active sites to participate in the reaction, making recombination more likely to occur during this migration process. Meanwhile, this reaction imposes more stringent requirements on the band structure of the photocatalyst. The potential of CB must be more negative than the reduction potential of hydrogen, while the potential of VB should be higher than the oxidation potential of water. Notably, seawater accounts for approximately 97% of the total global water resources, making it a raw material with vast reserves that can be directly accessed. Photocatalytic seawater splitting for H_2 production does not rely on scarce freshwater resources [253,254]. Meanwhile, this technology can be integrated with wave energy and tidal energy to synergistically achieve the piezo-photocatalytic effect, emerging as a crucial and highly promising development direction in the field of photocatalytic H_2 production. The oxidation of the photocatalyst by photogenerated holes is the main reason for its insufficient stability. Furthermore, the kinetic balance between hole consumption by sacrificial agents and proton reduction critically governs the overall photocatalytic reaction rate. By coupling the oxidation half-reaction with reactions such as biomass conversion and alcohol oxidation, the photogenerated holes can be consumed in time to enhance the stability of the photocatalyst while achieving the synthesis of high-value chemicals [255,256]. For example, using organic substances such as methanol, ethanol, and glycerol as sacrificial agents, methanol oxidation can produce formaldehyde and formic acid, and glycerol can be oxidized to form propylene glycol or hydroxyacetone [256–258]. Therefore, achieving the joint production of clean H_2 energy and value-added organic chemicals under solar illumination is a green and sustainable approach. In conclusion, these development directions are more conducive to realizing the industrial application of photocatalytic green H_2 production.

Clarifying the reaction mechanism is a prerequisite for the accurate design of photocatalysts. The ambiguity of the reaction mechanism often leads to the design of photocatalysts being trapped in a "trial and error" exploration approach. Therefore, analyzing the reaction mechanism at the atomic and molecular levels and establishing the "structure–property–mechanism"

relationship are fundamental guarantees for achieving precise design of photocatalysts and breaking through the bottlenecks of efficiency and stability. It is also the basis to promote the technology of photocatalytic H_2 production from the laboratory to practical applications. Advanced characterization techniques achieve dynamic tracking of light absorption, charge separation, and surface reaction processes through real-time, *in situ* capture of the dynamic changes in active species during the reaction process, which provides sufficient data support for in-depth analysis of the mechanism. Advanced computational methods, such as DFT calculations, can reveal the relationship between the structure and performance of photocatalysts at the atomic scale and accurately predict and design the structure of photocatalysts. Machine learning, through the data-driven approach, has broken through the limitations of the "trial and error" method in traditional material research and is an important engine for the development of materials science toward efficiency and precision. By dealing with massive data and mining hidden laws, on the one hand, the characterization data can be integrated to accurately identify the key parameters affecting the reaction mechanism. On the other hand, it can efficiently predict the energy barriers of reaction pathways and the stability of intermediates, excavating potential mechanisms that are difficult to cover with traditional experiments. For example, by training the neural network model, the ΔG_{H^*} on the surface of different alloy cocatalysts can be rapidly predicted, revealing its quantitative relationship with the H_2 production activity and providing theoretical guidance for the design of active sites. Based on the above, the combination of in situ characterization techniques, advanced computational materials science, and machine learning is an important means for in-depth analysis of mechanisms and accelerating the research and development process.

In summary, photocatalytic green H_2 production technology offers a clean and efficient approach for the acquisition of sustainable H_2 energy. With the advantages of solar-driven processes and minimal environmental impact, it has become an important breakthrough in addressing energy crises and environmental issues. In recent years, although significant progress has been made in photocatalyst design, reaction mechanism analysis, and system optimization, the realization of large-scale applications still faces serious challenges, such as a restricted light absorption range, a high recombination rate of photogenerated carriers, and insufficient photocatalyst stability. We have reviewed the latest research achievements in the field of green H_2 production through photocatalysis, covering the construction strategies of efficient photocatalysts, the advances in charge dynamics and surface reaction mechanisms, and specifically proposed future development directions to break through the existing bottlenecks. We expect that this work can provide valuable references for designing high-performance photocatalytic systems and promoting the practical application of photocatalytic green H_2 production technology and contribute to the green and sustainable development of society.

Acknowledgements

This work was supported by the National Natural Science Foundation of China (Nos. 52402359, 52325208, 52106248, and 22279029), the Key Scientific and Technological Research Project in Henan Province (Nos. 252102321054 and 252102240081), the Doctor Foundation of Henan University of Technology (No. 2023BS025), and the Innovation and Entrepreneurship Training Project for College Students in Henan Province (No. S202510463063)

Author contributions

Mengxi Tan: Writing– original draft, Investigation. Jing Chen: Writing – review & editing, Supervision. Zenghui Zhang: Writing – review & editing, Visualization. Lushan Ma: Investigation. Luhan Wang: Investigation. Yang Li: Investigation, Writing – review & editing. Yang Bai: Writing – review & editing, Validation, Supervision.

Availability of data and materials

The data that support the findings of this study are available from the corresponding author upon reasonable request.

Competing interests

The authors have no competing interests to declare that are relevant to the content of this article. The author Yang Bai is the Associate Editor of this journal.

References

[1] Teng JY, Li WL, Wei Z, *et al.* Coupling photocatalytic hydrogen production with key oxidation reactions. *Angew Chem Int Edit* 2024, **63**: 202416039.

[2] Nishiyama H, Yamada T, Nakabayashi M, *et al.* Photocatalytic solar hydrogen production from water on a 100-m^2 scale. *Nature* 2021, **598**: 304–307.

[3] Yu HJ, Wei XD, Wang M, *et al.* Macroscopic polarization enhancement boosting piezo-photocatalytic performance via Nb-doping on B-site of $Bi_4Ti_3O_{12}$ nanosheets. *J Adv Ceram* 2024, **13**: 437–446.

[4] Dang VH, Nguyen TA, Le MV, *et al.* Photocatalytic hydrogen production from seawater splitting: Current status, challenges, strategies and prospective applications. *Chem Eng J* 2024, **484**: 149213.

[5] Wang Q, Domen K. Particulate photocatalysts for light-driven water splitting: Mechanisms, challenges, and design strategies. *Chem Rev* 2020, **120**: 919–985.

[6] Liang LL, Yang YJ, Gong YT, *et al.* Machine learning-guided discovery of stable low-work-function perovskite oxides for advanced catalysis and energy technologies. *J Adv Ceram* 2025, **14**: 9221159.

[7] Chen SS, Takata T, Domen K. Particulate photocatalysts for overall water splitting. *Nat Rev Mater* 2017, **2**: 17050.

[8] Guo SH, Li XH, Li J, *et al.* Boosting photocatalytic hydrogen production from water by photothermally induced biphase systems. *Nat Commun* 2021, **12**: 1343.

[9] Zhang HB, Shao CF, Wang ZL, *et al.* One-step synthesis of seamlessly contacted non-precious metal cocatalyst modified CdS hollow nanoflowers spheres for photocatalytic hydrogen production. *J Mater Sci Technol* 2024, **195**: 146–154.

[10] Information on https://www.iea.org/reports/global-hydrogen-review-2024.

[11] Lu Y, Jia XF, Ma ZY, *et al.* W^{5+}–W^{5+} pair induced LSPR of $W_{18}O_{49}$ to sensitize $ZnIn_2S_4$ for full-spectrum solar-light-driven photocatalytic hydrogen evolution. *Adv Funct Mater* 2022, **32**: 2203638.

[12] Fang S, Zhu XR, Liu XK, *et al.* Uncovering near-free platinum single-atom dynamics during electrochemical hydrogen evolution reaction. *Nat Commun* 2020, **11**: 1029.

[13] Hu YP, Ding X, Feng J, *et al.* Molecular regioisomerism of benzobisthiazole-based conjugated polymers promotes photocatalytic hydrogen production. *Adv Funct Mater* 2024, **34**: 2400946.

[14] Rahman MZ, Davey K, Mullins CB. Tuning the intrinsic properties of carbon nitride for high quantum yield photocatalytic hydrogen production. *Adv Sci* 2018, **5**: 1800820.

[15] Li JS, Yao J, Yu Q, *et al.* Understanding the unique Ohmic-junction for enhancing the photocatalytic activity of CoS_2/$MgIn_2S_4$ towards

hydrogen production. *Appl Catal B Environ Energy* 2024, **351**: 123950.
[16] Jiang TL, Liu ZC, Yuan Y, *et al.* Ultrafast electrical pulse synthesis of highly active electrocatalysts for beyond-industrial-level hydrogen gas batteries. *Adv Mater* 2023, **35**: 2300502.
[17] Tan MX, Huang C, Yu CY, *et al.* Unexpected high-performance photocatalytic hydrogen evolution in Co@NCNT@$ZnIn_2S_4$ triggered by directional charge separation and transfer. *Small* 2022, **18**: 2205266.
[18] Zhang L, Hu ZH, Huang JT, *et al.* Experimental and DFT studies of flower-like Ni-doped Mo_2C on carbon fiber paper: A highly efficient and robust HER electrocatalyst modulated by $Ni(NO_3)_2$ concentration. *J Adv Ceram* 2022, **11**: 1294–1306.
[19] Hwang SW, Jeong YJ, Tan RF, *et al.* Texture development and surface reconstruction of $BiVO_4$ photoanode via one-pot hydrothermal reaction for enhanced photoelectrochemical water splitting. *J Adv Ceram* 2025, **14**: 9221043.
[20] Xu ZH, Kibria MG, AlOtaibi B, *et al.* Towards enhancing photocatalytic hydrogen generation: Which is more important, alloy synergistic effect or plasmonic effect. *Appl Catal B Environ* 2018, **221**: 77–85.
[21] Zhang J, Sha SM, Ni JC, *et al.* Design strategies for high entropy materials in water electrolysis: Enhancing activity, stability, and reaction kinetics. *J Adv Ceram* 2025, **14**: 9221152.
[22] Li J, Zhou J, Wang XH, *et al. In situ* construction of single-atom electronic bridge on COF to enhance photocatalytic H_2 production. *Angew Chem Int Edit* 2024, **63**: 202411721.
[23] Zhong SL, Shi HX, Xiao CW, *et al.* Efficient photocatalytic hydrogen production via single-atom Pt anchored hydrogen-bonded organic frameworks. *J Colloid Interf Sci* 2025, **679**: 91–101.
[24] Schlenkrich J, Lübkemann-Warwas F, Graf RT, *et al.* Investigation of the photocatalytic hydrogen production of semiconductor nanocrystal-based hydrogels. *Small* 2023, **19**: 2208108.
[25] Wang FH, Dong BB, Wang JW, *et al.* Self-supported porous heterostructure WC/WO_{3-x} ceramic electrode for hydrogen evolution reaction in acidic and alkaline media. *J Adv Ceram* 2022, **11**: 1208–1221.
[26] Shi KN, Ding SH, Zhang XL, *et al.* Synergistic effect of sulfur atoms and ordered oxygen vacancies to enhance Fe_2O_3 bifunctional electrocatalytic water splitting activity. *J Adv Ceram* 2025, **14**: 9221157.
[27] Xin X, Li YK, Zhang YZ, *et al.* Large electronegativity differences between adjacent atomic sites activate and stabilize $ZnIn_2S_4$ for efficient photocatalytic overall water splitting. *Nat Commun* 2024, **15**: 337.
[28] Wang PZ, Jin F, Yang C, *et al.* Co nanoparticles on MnO: Electron transfer through ohmic and S-scheme heterojunction for photocatalytic hydrogen evolution. *ACS Appl Mater Inter* 2025, **17**: 10542–10555.
[29] Hisatomi T, Kubota J, Domen K. Recent advances in semiconductors for photocatalytic and photoelectrochemical water splitting. *Chem Soc Rev* 2014, **43**: 7520–7535.
[30] Shahid MU, Najam T, Helal MH, *et al.* Transition metal chalcogenides and phosphides for photocatalytic H_2 generation via water splitting: A critical review. *Int J Hydrogen Energ* 2024, **62**: 1113–1138.
[31] Yang JX, Yu WB, Li CF, *et al.* PtO nanodots promoting Ti_3C_2 MXene *in-situ* converted Ti_3C_2/TiO_2 composites for photocatalytic hydrogen production. *Chem Eng J* 2021, **420**: 129695.
[32] Fujishima A, Honda K. Electrochemical photolysis of water at a semiconductor electrode. *Nature* 1972, **238**: 37–38.
[33] Liu YX, Sun ZX, Hu YH. Bimetallic cocatalysts for photocatalytic hydrogen production from water. *Chem Eng J* 2021, **409**: 128250.
[34] Li MT, Zhou JH, Di R, *et al.* Piezoelectric potential activated interfacial electric field in $BiFeO_3$@$BaTiO_3$ heterojunction for rapid and round-the-clock photocatalytic degradation of organic pollutants. *J Adv Ceram* 2024, **13**: 2030–2042.
[35] Mani AD, Li J, Wang ZQ, *et al.* Coupling of piezocatalysis and photocatalysis for efficient degradation of methylene blue by $Bi_{0.9}Gd_{0.07}La_{0.03}FeO_3$ nanotubes. *J Adv Ceram* 2022, **11**: 1069–1081.
[36] Wang Q, Zheng DD, Pan ZM, *et al.* Spatially separated redox cocatalysts on poly triazine imides boosting photocatalytic overall water splitting. *Adv Funct Mater* 2025, **35**: 2501889.
[37] Zhang RQ, Liu RC, Ding ZH, *et al.* Photothermal-assisted S-scheme heterojunction of $Cu_3SnS_4/Mn_{0.3}Cd_{0.7}S$ for enhanced photocatalytic hydrogen production. *J Colloid Interf Sci* 2025, **682**: 568–577.
[38] Yang RM, Mu WN, He LY, *et al.* CdS/NiCoAl-LDH heterojunction for superior photocatalytic hydrogen production and stability in water splitting. *Chem Eng J* 2025, **503**: 158495.
[39] Zhang SY, Li XS, Zhu AM, *et al.* Gliding arc plasma induced one-step millisecond synthesis of highly crystalline mesoporous TiO_2 homojunctions for robust photocatalytic H_2 production. *Small* 2025, **21**: 2410603.
[40] Wang C, Lu YC, Wang ZQ, *et al.* Salt-assisted construction of hydrophilic carbon nitride photocatalysts with abundant water molecular adsorption sites for efficient hydrogen production. *Appl Catal B Environ Energy* 2024, **350**: 123902.
[41] Deng J, Xu XY, Su B, *et al.* Structural amine-induced interfacial electrical double layers for efficient photocatalytic H_2 evolution. *Mater Horiz* 2025, **12**: 5702–5709.
[42] Shi HR, Yan B, Li HY, *et al.* A new Ni-based cocatalyst nickel thiocarbonate enhancing graphitic carbon nitride photocatalytic hydrogen production by constructing a built-in electric field. *J Colloid Interf Sci* 2024, **672**: 126–132.
[43] Jin XX, Li X, Dong LM, *et al.* Enhancement and inhibition of photocatalytic hydrogen production by fine piezoelectric potential tuning over piezo-photocatalyst. *Nano Energy* 2024, **123**: 109341.
[44] Zhu JF, Bi QY, Tao YH, *et al.* Mo-modified $ZnIn_2S_4$@$NiTiO_3$ S-scheme heterojunction with enhanced interfacial electric field for efficient visible-light-driven hydrogen evolution. *Adv Funct Mater* 2023, **33**: 2213131.
[45] Chen LY, Xie XL, Su TM, *et al.* Co_3O_4/CdS p–n heterojunction for enhancing photocatalytic hydrogen production: Co–S bond as a bridge for electron transfer. *Appl Surf Sci* 2021, **567**: 150849.
[46] Zheng DD, Wang Q, Pan ZM, *et al.* Poly(triazine imide) nanospheres with spatially exposed prismatic facets for photocatalytic overall water splitting. *Sci China Mater* 2024, **67**: 1900–1906.
[47] Zhong YQ, Li MY, Luan X, *et al.* Ultrathin $ZnIn_2S_4$/ZnSe heteronanosheets with modulated S-scheme enable high efficiency of visible-light-responsive photocatalytic hydrogen evolution. *Appl Catal B Environ* 2023, **335**: 122859.
[48] Zhan XQ, Ou DL, Zheng YP, *et al.* Boosted photocatalytic hydrogen production over two-dimensional/two-dimensional Ta_3N_5/ReS_2 van der Waals heterojunctions. *J Colloid Interf Sci* 2023, **629**: 455–466.
[49] Xu FH, Weng BC. Photocatalytic hydrogen production: An overview of new advances in structural tuning strategies. *J Mater Chem A* 2023, **11**: 4473–4486.
[50] Wu C, Huang WX, Liu HM, *et al.* Insight into synergistic effect of Ti_3C_2 MXene and MoS_2 on anti-photocorrosion and photocatalytic of CdS for hydrogen production. *Appl Catal B Environ* 2023, **330**: 122653.
[51] Wang XH, Wang XH, Shi TY, *et al.* "O–S" charge transfer mechanism guiding design of a $ZnIn_2S_4/SnSe_2/In_2Se_3$ heterostructure photocatalyst for efficient hydrogen production. *ACS Catal* 2023, **13**: 1020–1032.
[52] Tan MX, Yu CY, Yao JQ, *et al.* The 2D van der Waals heterojunction MoC@NG@CN for enhanced photocatalytic hydrogen production. *J Mater Chem A* 2023, **11**: 5350–5358.
[53] Sun XZ, Cao CC, Fu YY, *et al.* Engineering different B doping modes on Ru active sites for efficient alkaline hydrogen evolution. *J Mater Chem A* 2023, **11**: 23370–23375.
[54] Lu JL, Shi YX, Chen ZZ, *et al.* Photothermal effect of carbon dots for boosted photothermal-assisted photocatalytic water/seawater splitting into hydrogen. *Chem Eng J* 2023, **453**: 139834.

[55] Li RH, Takata T, Zhang BB, *et al.* Criteria for efficient photocatalytic water splitting revealed by studying carrier dynamics in a model Al-doped $SrTiO_3$ photocatalyst. *Angew Chem Int Edit* 2023, **62**: 202313537.
[56] Li XQ, Chen DY, Li NJ, *et al.* Built-in electric field and oxygen absorption synergistically optimized an organic/inorganic heterojunction for high-efficiency photocatalytic hydrogen peroxide production. *J Colloid Interf Sci* 2023, **648**: 664–673.
[57] Gu HJ, Zhang HH, Wang XL, *et al.* Robust construction of CdSe nanorods@Ti_3C_2 MXene nanosheet for superior photocatalytic H_2 evolution. *Appl Catal B Environ* 2023, **328**: 122537.
[58] Zhou XF, Tian YH, Luo J, *et al.* MoC quantum dots@N-doped-carbon for low-cost and efficient hydrogen evolution reaction: From electrocatalysis to photocatalysis. *Adv Funct Mater* 2022, **32**: 2201518.
[59] Zhao H, Liu J, Li CF, *et al.* Meso-microporous nanosheet-constructed 3DOM perovskites for remarkable photocatalytic hydrogen production. *Adv Funct Mater* 2022, **32**: 2112831.
[60] Chong WK, Ng BJ, Kong XY, *et al.* Non-metal doping induced dual p–n charge properties in a single $ZnIn_2S_4$ crystal structure provoking charge transfer behaviors and boosting photocatalytic hydrogen generation. *Appl Catal B Environ* 2023, **325**: 122372.
[61] Zhou DX, Xue XD, Wang X, *et al.* Ni, in Co-doped $ZnIn_2S_4$ for efficient hydrogen evolution: Modulating charge flow and balancing H adsorption/desorption. *Appl Catal B Environ* 2022, **310**: 121337.
[62] Zhang WJ, Zhao SS, Xing YP, *et al.* Sandwich-like P-doped h-BN/$ZnIn_2S_4$ nanocomposite with direct Z-scheme heterojunction for efficient photocatalytic H_2 and H_2O_2 evolution. *Chem Eng J* 2022, **442**: 136151.
[63] Tao JN, Wang MY, Liu GW, *et al.* Efficient photocatalytic hydrogen evolution coupled with benzaldehyde production over 0D $Cd_{0.5}Zn_{0.5}S$/2D Ti_3C_2 Schottky heterojunction. *J Adv Ceram* 2022, **11**: 1117–1130.
[64] Su P, Kong DZ, Zhao HH, *et al.* $SnFe_2O_4$/$ZnIn_2S_4$/PVDF piezophotocatalyst with improved photocatalytic hydrogen production by synergetic effects of heterojunction and piezoelectricity. *J Adv Ceram* 2023, **12**: 1685–1700.
[65] Ahmad MI, Chen S, Yu HT, *et al.* Electronic tuning of SnO_2 by rGO nanosheets for highly efficient photocatalytic hydrogen peroxide evolution. *ACS Sustain Chem Eng* 2023, **11**: 10520–10533.
[66] Zhang JN, Lei YF, Cao S, *et al.* Photocatalytic hydrogen production from seawater under full solar spectrum without sacrificial reagents using TiO_2 nanoparticles. *Nano Res* 2022, **15**: 2013–2022.
[67] Li HM, Shen QQ, Zhang H, *et al.* Oxygen vacancy-mediated WO_3 phase junction to steering photogenerated charge separation for enhanced water splitting. *J Adv Ceram* 2022, **11**: 1873–1888.
[68] Tan RF, Jeong YJ, Li Q, *et al.* Defect-rich spinel ferrites with improved charge collection properties for efficient solar water splitting. *J Adv Ceram* 2023, **12**: 612–624.
[69] Šalipur H, Manojlović D, Milošević K, *et al.* Unraveling the solar and visible light-induced deactivation mechanism of Pt-decorated carbon/TiO_2 nanocomposite in photocatalytic hydrogen production. *J Environ Chem Eng* 2024, **12**: 112862.
[70] Zhao DM, Wang YQ, Dong CL, *et al.* Electron-deficient Zn–N_6 configuration enabling polymeric carbon nitride for visible-light photocatalytic overall water splitting. *Nano-Micro Lett* 2022, **14**: 223.
[71] Zhang YZ, Liang C, Feng HP, *et al.* Nickel single atoms anchored on ultrathin carbon nitride for selective hydrogen peroxide generation with enhanced photocatalytic activity. *Chem Eng J* 2022, **446**: 137379.
[72] Zhang SY, Gao MJ, Zhai YP, *et al.* Which kind of nitrogen chemical states doped carbon dots loaded by g-C_3N_4 is the best for photocatalytic hydrogen production. *J Colloid Interf Sci* 2022, **622**: 662–674.
[73] Sun LJ, Jia YM, Yang F, *et al.* Bimetallic ZnNi co-catalyst modified g-C_3N_4 nanosheets for highly efficient photocatalytic hydrogen evolution. *Int J Hydrogen Energ* 2025, **98**: 1386–1395.
[74] Potapenko KO, Vasilchenko DB, Kurenkova AY, *et al.* Expanding g-C_3N_4 capabilities for photocatalytic H_2 production by modification with $Ti_3C_2T_x$ MXene. *Int J Hydrogen Energ* 2025, **99**: 291–300.
[75] Liu XY, Liu H, Wang YJ, *et al.* Nitrogen-rich g-C_3N_4@AgPd Mott-Schottky heterojunction boosts photocatalytic hydrogen production from water and tandem reduction of NO_3^- and NO_2^-. *J Colloid Interf Sci* 2021, **581**: 619–626.
[76] Liu JY, Wei ZD, Fang WJ, *et al.* *In-situ* construction of amorphous red phosphorus/$SrTiO_3$ heterojunctions for enhanced visible-light photocatalytic hydrogen production. *Int J Hydrogen Energ* 2024, **93**: 1127–1134.
[77] Jiang JH, Zhou Y, Zhang JL, *et al.* Accelerating the charge separation from the Schottky junction effect of Pd-loaded Al: $SrTiO_3$ for highly efficient photocatalytic hydrogen evolution. *Int J Hydrogen Energ* 2024, **82**: 646–654.
[78] Yu CY, He JJ, Tan MX, *et al.* Selective enhancement of photo-piezocatalytic performance in $BaTiO_3$ via heterovalent ion doping. *Adv Funct Mater* 2022, **32**: 2209365.
[79] Wang H, Zhang HF, Wang JH, *et al.* Mechanistic understanding of efficient photocatalytic H_2 evolution on two-dimensional layered lead iodide hybrid perovskites. *Angew Chem Int Edit* 2021, **60**: 7376–7381.
[80] Zheng D, Xue YF, Wang J, *et al.* Nanocatalysts in photocatalytic water splitting for green hydrogen generation: Challenges and opportunities. *J Clean Prod* 2023, **414**: 137700.
[81] Yang Y, Zhou CY, Wang WJ, *et al.* Recent advances in application of transition metal phosphides for photocatalytic hydrogen production. *Chem Eng J* 2021, **405**: 126547.
[82] Yu XX, Li H, Xu CC, *et al.* Liquid–liquid phase separation-mediated photocatalytic subcellular hybrid system for highly efficient hydrogen production. *Adv Sci* 2024, **11**: 2400097.
[83] Wang ZM, Huang XQ, Jia Y, *et al.* Localized surface plasmon resonance-induced bidirectional electron transfer of formic acid adsorption for boosting photocatalytic hydrogen production on Ni/TiO_2. *Chem Eng J* 2024, **482**: 148942.
[84] Yu JG, Yu YF, Zhou P, *et al.* Morphology-dependent photocatalytic H_2-production activity of CdS. *Appl Catal B Environ* 2014, **156**: 184–191.
[85] Yan YR, Zhao YY, Lou Y, *et al.* Constructing core–shell phosphorus doped $MnCo_2O_{4.5}$@ZIS for efficient photocatalytic hydrogen production from water splitting. *J Colloid Interf Sci* 2025, **680**: 965–975.
[86] Shi YX, Li LL, Xu Z, *et al.* Construction of full solar-spectrum available S-scheme heterojunction for boosted photothermal-assisted photocatalytic H_2 production. *Chem Eng J* 2023, **459**: 141549.
[87] Shan PN, Geng K, Shen Y, *et al.* Facile synthesis of hierarchical core–shell carbon@$ZnIn_2S_4$ composite for boosted photothermal-assisted photocatalytic H_2 production. *J Colloid Interf Sci* 2025, **677**: 1098–1107.
[88] Wang CX, Cui DH, Yang X, *et al.* $H_3PMo_{12}O_{40}$@ZIF-67-derived CoMoC/$ZnIn_2S_4$ Schottky heterojunction for enhanced photocatalytic hydrogen evolution. *Int J Hydrogen Energ* 2024, **77**: 666–676.
[89] Lu P, Liu K, Liu Y, *et al.* Heterostructure with tightly-bound interface between In_2O_3 hollow fiber and $ZnIn_2S_4$ nanosheet toward efficient visible light driven hydrogen evolution. *Appl Catal B Environ Energy* 2024, **345**: 123697.
[90] Zuo LY, Li R, Liu Q, *et al.* *In situ* Mo-doped $ZnIn_2S_4$/Ni–Ni Hofmann-type coordination polymer composites for photocatalytic hydrogen evolution reaction. *J Colloid Interf Sci* 2024, **661**: 207–218.
[91] Jia L, Ma N, Shao PP, *et al.* Incorporating ReS_2 nanosheet into $ZnIn_2S_4$ nanoflower as synergistic Z-scheme photocatalyst for highly effective and stable visible-light-driven photocatalytic hydrogen evolution and degradation. *Small* 2024, **20**: 2404622.

[92] Du JY, Zhang LJ, Zhang LQ, *et al.* Polarised electric field induced efficient photocatalytic hydrogen production at $NiCrO_4$/ZnCdS heterogeneous interface. *J Colloid Interf Sci* 2025, **689**: 137211.
[93] Liu MH, Zhang GG, Liang XC, *et al.* Rh/Cr_2O_3 and CoO_x cocatalysts for efficient photocatalytic water splitting by poly (triazine imide) crystals. *Angew Chem Int Edit* 2023, **62**: 202304694.
[94] Wang J, Niu XY, Hao Q, *et al.* Promoting charge separation in $CuInS_2$/CeO_2 photocatalysts by an S-scheme heterojunction for enhanced photocatalytic H_2 production. *Chem Eng J* 2024, **493**: 152534.
[95] Deng W, Hao XQ, Yang JQ, *et al.* Strong electron coupling effect of non-precious metal Schottky junctions enhanced square meter level photocatalytic hydrogen evolution. *Appl Catal B Environ Energy* 2025, **360**: 124551.
[96] He BW, Xiao P, Wan SJ, *et al.* Rapid charge transfer endowed by interfacial Ni-O bonding in S-scheme heterojunction for efficient photocatalytic H_2 and imine production. *Angew Chem Int Edit* 2023, **62**: 202313172.
[97] Liu YT, Ma MY, Cheng XZ, *et al.* Engineering electron lifetime for high-performance heterostructured 1D CdS photocatalyst. *Small* 2025, **21**: 2412588.
[98] Hu TP, Dai K, Zhang JF, *et al.* Noble-metal-free Ni_2P modified step-scheme $SnNb_2O_6$/CdS-diethylenetriamine for photocatalytic hydrogen production under broadband light irradiation. *Appl Catal B Environ* 2020, **269**: 118844.
[99] Hunge YM, Yadav AA, Kang SW, *et al.* Visible light activated MoS_2 /ZnO composites for photocatalytic degradation of ciprofloxacin antibiotic and hydrogen production. *J Photoch Photobio A* 2023, **434**: 114250.
[100] Li T, Tsubaki N, Jin ZL. S-scheme heterojunction in photocatalytic hydrogen production. *J Mater Sci Technol* 2024, **169**: 82–104.
[101] Huang YJ, Xie JY, Zhang J, *et al.* Preparation of carbon/Fe-doped g-C_3N_4 and study on its photocatalytic hydrogen production performance. *J Mol Struct* 2024, **1307**: 138043.
[102] Wang L, Zhang Y. Impact of interfaces on the performance of covalent organic frameworks for photocatalytic hydrogen production. *Small* 2025, **21**: 2408395.
[103] Kong D, Zheng Y, Kobielusz M, *et al.* Recent advances in visible light-driven water oxidation and reduction in suspension systems. *Mater Today* 2018, **21**: 897–924.
[104] Fang SY, Liu YX, Sun ZX, *et al.* Photocatalytic hydrogen production over Rh-loaded TiO_2: What is the origin of hydrogen and how to achieve hydrogen production from water. *Appl Catal B Environ* 2020, **278**: 119316.
[105] Zhang LQ, Yang H, Li YJ, *et al.* Rapid transfer pathways formed with bimetallic oxides and nickel boosting photocatalytic hydrogen production. *J Colloid Interf Sci* 2025, **694**: 137709.
[106] Li Z, Huang F, Xu YF, *et al.* Electron-extracting system with enhanced photocatalytic hydrogen production performance: Synergistic utilization of Z-scheme and Ohmic heterojunctions. *Chem Eng J* 2022, **429**: 132476.
[107] Sun BJ, Zhou W, Li HZ, *et al.* Synthesis of particulate hierarchical tandem heterojunctions toward optimized photocatalytic hydrogen production. *Adv Mater* 2018, **30**: 1804282.
[108] Guo GY, Feng JX, Wang HT, *et al.* Loaded carbon shell encapsulated transition metal and $ZnIn_2S_4$ on carbonized paper for enhanced photocatalytic hydrogen production. *J Colloid Interf Sci* 2025, **697**: 137990.
[109] Zhang M, Chen XJ, Jiang XY, *et al.* Activate Fe_3S_4 nanorods by Ni doping for efficient dye-sensitized photocatalytic hydrogen production. *ACS Appl Mater Inter* 2021, **13**: 14198–14206.
[110] Yang JD, Zeng XK, Tebyetekerwa M, *et al.* Engineering 2D photocatalysts for solar hydrogen peroxide production. *Adv Energy Mater* 2024, **14**: 2400740.
[111] Yang Y, Zheng YQ, Liu SK, *et al.* Deep learning prediction of photocatalytic water splitting for hydrogen production under natural light based on experiments. *Energ Convers Manage* 2024, **301**: 118007.
[112] Zhao XW, Zhang XY, Lei MJ, *et al.* Synergistic effect of morphology regulation of $LaNiO_3$ S-scheme heterojunction for enhanced photocatalytic hydrogen production. *J Mater Sci Technol* 2026, **245**: 238–248.
[113] Cao Y, Han Z, Song R, *et al.* Topological Luttinger-semimetal $CoAs_3$ dye-sensitized photocatalyst for efficient solar hydrogen evolution. *Nat Commun* 2025, **16**: 8759.
[114] Lu XY, Niu XK, Zhang EH, *et al.* Energy transfer-induced enhanced photocatalytic hydrogen production in a D–π–a cyanine dye-encapsulated pyrene-based metal–organic framework. *J Colloid Interf Sci* 2025, **698**: 138047.
[115] Che Y, Weng B, Li KJ, *et al.* Chemically bonded nonmetallic LSPR S-scheme hollow heterostructure for boosting photocatalytic performance. *Appl Catal B Environ Energy* 2025, **361**: 124656.
[116] Liu X, Zhang YJ, Zhang WX, *et al.* Type II/Schottky heterojunctions-triggered multi-channels charge transfer in Pd–TiO_2–Cu_2O hybrid promotes photocatalytic hydrogen production. *J Colloid Interf Sci* 2025, **685**: 173–185.
[117] Wang ZG, Bie CB. HOF/COF 2D/2D S-scheme heterojunction for photocatalytic H_2 production. *J Mater Sci Technol* 2026, **243**: 206–208.
[118] Téllez-Flores D, Sánchez-Cantú M, Tzompantzi F, *et al.* Influence of the Zn/Al molar ratio over the photocatalytic hydrogen production by ZnS/ZnAl-LDH composites. *Int J Hydrogen Energ* 2025, **108**: 32–42.
[119] Wu GY, Gao X, Sun PP, *et al.* High-intensity interfacial electric fields between co-catalysts and semiconductor: A determinant factor in enhancing photocatalytic hydrogen production. *Appl Catal B Environ Energy* 2025, **371**: 125265.
[120] Umer K, Li BN, Shahid H, *et al.* Electrostatically engineered Ni4POM/$Mn_{0.2}Cd_{0.8}S$ through 1,4-benzene dicarboxylic acid for efficient photocatalytic hydrogen production. *Appl Catal B Environ Energy* 2025, **373**: 125357.
[121] Lazaar N, Wu SM, Qin SS, *et al.* Single-atom catalysts on C_3N_4: Minimizing single atom Pt loading for maximized photocatalytic hydrogen production efficiency. *Angew Chem Int Edit* 2025, **64**: 202416453.
[122] Shan PN, Geng K, Guo L, *et al.* Synergistic effects of photothermal response and Schottky junction for enhanced photothermal-assisted photocatalytic hydrogen production. *Chem Eng J* 2025, **513**: 162801.
[123] Li ZY, Li M, Ding MJ, *et al.* Nitrogen-doped biochar assists rapid electron transfer at the ZnCdS/$CoMoO_4$ interface to enhance photocatalytic hydrogen production. *J Colloid Interf Sci* 2025, **699**: 138231.
[124] Geng K, Shan PN, Shi JQ, *et al.* Broad spectral absorption cooperates with local plasma resonance for promoted photothermal-assisted photocatalytic hydrogen production. *Chem Eng J* 2025, **507**: 160561.
[125] Cheng YJ, Zhao JQ, Ma XF, *et al.* Simultaneously tailoring hydrostability and photoelectroactivity in heterocluster metal–organic frameworks for efficient photocatalytic hydrogen production. *Adv Mater* 2025, **37**: 2503756.
[126] Tan MX, Yao ZY, Ma LS, *et al.* Design of the photocatalyst for H_2O_2 production by oxygen reduction reaction. *Coordin Chem Rev* 2025, **544**: 216993.
[127] Tan MX, Yu CY, Li JJ, *et al.* Engineering of g-C_3N_4-based photocatalysts to enhance hydrogen evolution. *Adv Colloid Interfac* 2021, **295**: 102488.
[128] Tan MX, Ma Y, Yu CY, *et al.* Boosting photocatalytic hydrogen production via interfacial engineering on 2D ultrathin Z-scheme $ZnIn_2S_4$/g-C_3N_4 heterojunction. *Adv Funct Mater* 2022, **32**: 2111740.
[129] Chen YF, Agrelo-Lestón A, Burgués-Ceballos I, *et al.* Bimetallic nanoparticles as cocatalysts for photocatalytic hydrogen production. *Adv Funct Mater* 2025: 06279.

[130] Wang ZN, Zhou D, Tian KG, *et al.* Asymmetric $Zn_{0.5}Cd_{0.5}S$ loading of CoS_x for full-space electric field photocatalytic hydrogen production and synergistic organic synthesis. *ACS Catal* 2025, **15**: 3660–3673.
[131] Meinhardová V, Dubnová L, Kobielusz M, *et al.* Electron migration pathways in S-scheme GaP-TiO_2 photocatalysts and their implications for photocatalytic hydrogen production. *Acta Mater* 2025, **296**: 121274.
[132] Zhang DD, Gao ZY, Yang DJ, *et al.* Crystal-interface-mediated self-assembly of $ZnIn_2S_4$/CdS S-scheme heterojunctions toward efficient photocatalytic hydrogen production. *Carbon Energy* 2025, **7**: 707.
[133] Che HN, Liu LH, Che GB, *et al.* Control of energy band, layer structure and vacancy defect of graphitic carbon nitride by intercalated hydrogen bond effect of NO_3^- toward improving photocatalytic performance. *Chem Eng J* 2019, **357**: 209–219.
[134] Ruan XW, Meng DP, Xu MH, *et al.* Semi-organic artificial photosynthetic system with engineered phenoxazinone derivatives for photocatalytic hydrogen production with broadened near-infrared light harvesting. *Adv Sci* 2025, **12**: 2501037.
[135] Li SJ, Xiao XP, Zuo LY, *et al.* Synthesis of Mn-doped hollow octahedron $ZnIn_2S_4$ to enhance photocatalytic hydrogen production performance utilizing metal–organic framework as template. *J Colloid Interf Sci* 2025, **684**: 412–422.
[136] Fan DQ, Zhao CX, Lu Y, *et al.* Immobilization of covalent triazine framework into hydrogels for photothermal-promoted gas-solid photocatalytic hydrogen production. *Adv Mater* 2025, **37**: 2505932.
[137] Zhang HJ, Jaenecke J, Bishara-Robertson IL, *et al.* Semiartificial photosynthetic nanoreactors for H_2 generation. *J Am Chem Soc* 2024, **146**: 34260–34264.
[138] Sheng HX, Wang J, Huang JH, *et al.* Strong synergy between gold nanoparticles and cobalt porphyrin induces highly efficient photocatalytic hydrogen evolution. *Nat Commun* 2023, **14**: 1528.
[139] Guo K, Yang S, Wang YT, *et al.* Self-sensitized cobalt molecular photocatalysts: The effects of alkali cations on tuning the activity of H_2 production. *ACS Catal* 2025, **15**: 18769–18781.
[140] Xia RQ, Wang WC, Zhou T, *et al.* Au_1–N_3 site induced mid-band charge trapping in carbon-defective holey G-$C_{3-x}N_4$ enhances highly efficient photocatalytic H_2 production. *Adv Funct Mater* 2025: 12866.
[141] Fan JP, Song CH, Zhang YT, *et al.* Engineering MXenes charge bridge enables fast carrier transport in S-scheme heterojunctions for enhanced photocatalytic H_2 production. *Appl Catal B Environ Energy* 2026, **385**: 126268.
[142] Wan SJ, Wang W, Cheng B, *et al.* A superlattice interface and S-scheme heterojunction for ultrafast charge separation and transfer in photocatalytic H_2 evolution. *Nat Commun* 2024, **15**: 9612.
[143] Guo YC, Tan X, Yu T, *et al.* Recent advances of photocatalytic hydrogen evolution via water vapor splitting. *Adv Funct Mater* 2025: e22276.
[144] Han X, Ge XY, He WW, *et al.* Covalent triazine frameworks modified by ultrafine Pt nanoparticles for efficient photocatalytic hydrogen production. *Nano Res* 2024, **17**: 4908–4915.
[145] Zi BY, Zheng HS, Zhou T, *et al.* Pr doping promotes the formation of Pt single atoms by regulating metal–support interaction for remarkable photocatalytic hydrogen production. *J Colloid Interf Sci* 2025, **680**: 298–306.
[146] Shi HR, Yan B, Xu HK, *et al.* $NiCS_3$: A cocatalyst surpassing Pt for photocatalytic hydrogen production. *J Colloid Interf Sci* 2024, **659**: 878–885.
[147] Geng L, Li WJ, Dong M, *et al.* Dual electric field and defect engineering induced multi-channel electron transfer for boosting photocatalytic hydrogen production on Cu^{2+}-doped $ZnMoO_4$/$ZnIn_2S_4$ heterojunction. *J Colloid Interf Sci* 2025, **679**: 748–759.
[148] Fan LL, An ZY, Xiao Q, *et al.* Enhanced charge transfer through defect and doping synergistic engineering for efficient hydrogen production. *Appl Catal B Environ Energy* 2025, **363**: 124821.
[149] Chen XY, Zhang QT, Wang Y, *et al.* Construction of O, S-dual-vacancy defects mediated H-CeO_2/H-CdS hollow core–shell spheres for photocatalytic hydrogen production. *J Mater Sci Technol* 2025, **238**: 86–96.
[150] Luan X, Yu ZQ, Zi JZ, *et al.* Photogenerated defect-transit dual S-scheme charge separation for highly efficient hydrogen production. *Adv Funct Mater* 2023, **33**: 2304259.
[151] Zhang H, Cai JM, Wang YT, *et al.* Insights into the effects of surface /bulk defects on photocatalytic hydrogen evolution over TiO_2 with exposed{001}facets. *Appl Catal B Environ* 2018, **220**: 126–136.
[152] Gui XX, Zhou YT, Pan D, *et al.* Construction of ternary Ni_2P/ZIF-8/CdS composite for efficient photocatalytic hydrogen production and pollutant degradation: Accelerating separation of photogenerated carriers. *J Phys Chem Solids* 2024, **190**: 111983.
[153] Feng Y, Fang X, Zang JN, *et al.* Improvement of charge-transfer kinetics via MXene and cobalt containing polyoxometalate loading on CdS for photocatalytic hydrogen production. *Sci China Chem* 2025, **68**: 772–780.
[154] Bie CB, Zhu BC, Wang LX, *et al.* A bifunctional CdS/MoO_2/MoS_2 catalyst enhances photocatalytic H_2 evolution and pyruvic acid synthesis. *Angew Chem Int Edit* 2022, **61**: e202212045.
[155] Chang YC, Syu SY, Hsu PC. Construction of In_2S_3–$In(OH)_3$–ZnS nanofibers for boosting photocatalytic hydrogen evolution. *Int J Hydrogen Energ* 2024, **86**: 24–35.
[156] Yuan YJ, Shen ZK, Wu ST, *et al.* Liquid exfoliation of g-C_3N_4 nanosheets to construct 2D-2D MoS_2/g-C_3N_4 photocatalyst for enhanced photocatalytic H_2 production activity. *Appl Catal B Environ* 2019, **246**: 120–128.
[157] Hao XQ, Jin ZL, Yang H, *et al.* Peculiar synergetic effect of MoS_2 quantum dots and graphene on metal–organic Frameworks for photocatalytic hydrogen evolution. *Appl Catal B Environ* 2017, **210**: 45–56.
[158] Hu XL, Lu SC, Tian J, *et al.* The selective deposition of MoS_2 nanosheets onto (101) facets of TiO_2 nanosheets with exposed (001) facets and their enhanced photocatalytic H_2 production. *Appl Catal B Environ* 2019, **241**: 329–337.
[159] Song JH, Ge W, Deng SD, *et al.* Construction of Au nanoparticles decorated on $ZnFe_2O_4$@$ZnIn_2S_4$ core–shell structure to enhance photocatalytic hydrogen production. *Colloid Surface A* 2025, **705**: 135705.
[160] Luan WQ, Yan YY, Wang JX, *et al.* Fabrication of in-doped CdSe/$Zn_3In_2S_6$ type II heterojunction composite for efficient photocatalytic hydrogen evolution. *Sep Purif Technol* 2025, **356**: 129907.
[161] Xi TL, Liu LJ, Liu Q, *et al.* Hollow MoS_2@$ZnIn_2S_4$ nanoboxes for improving photocatalytic hydrogen evolution. *Int J Hydrogen Energ* 2024, **62**: 62–70.
[162] Yan YB, Zhou L, Wang H, *et al.* Photothermal ReO_2/ReS_2/$Zn_2In_2S_5$ heterojunction for enhanced photocatalytic hydrogen evolution. *Sep Purif Technol* 2024, **346**: 127473.
[163] Chen ZZ, Yan YJ, Sun KQ, *et al.* Plasmonic coupling-boosted photothermal composite photocatalyst for achieving near-infrared photocatalytic hydrogen production. *J Colloid Interf Sci* 2024, **661**: 12–22.
[164] Chen ZH, Guo F, Sun HR, *et al.* Well-designed three-dimensional hierarchical hollow tubular g-C_3N_4/$ZnIn_2S_4$ nanosheets heterostructure for achieving efficient visible-light photocatalytic hydrogen evolution. *J Colloid Interf Sci* 2022, **607**: 1391–1401.
[165] Song JG, Su HY, Fang M, *et al.* Photochemical construction of the ZnCdS/PO/FeCoNiPi–MnO composite for efficient tandem application of photocatalytic partial water splitting and overall water splitting. *J Mater Chem A* 2022, **10**: 16029–16036.
[166] Li ZZ, Li HZ, Wang SJ, *et al.* Mesoporous black TiO_2/MoS_2/Cu_2S hierarchical tandem heterojunctions toward optimized photothermal-photocatalytic fuel production. *Chem Eng J* 2022, **427**: 131830.
[167] Hu XL, Xu YS, Tang S, *et al.* Photoreduction of aqueous protons coupling with alcohol oxidation on a S-scheme heterojunction photocatalyst MnO/carbon nitride. *Small* 2024, **20**: 2306563.

[168] Suo RB, Xie LJ, Hu ZY, *et al.* A Z-scheme heterojunction constructed by ZnO/$CeVO_4$ for highly active photocatalytic hydrogen production. *J Rare Earth* 2025, **43**: 1859–1869.
[169] Sun M, Wang J, Yu HH, *et al.* Converting solar energy into hydrogen energy: Research on the green hydrogen production mechanism of nanocomposite materials with graphene nanoribbons and ZnO composite materials based on the local electric field effect for transferring electrons. *Renew Energ* 2026, **256**: 124355.
[170] Xie Y, Wang TW, Li HQ, *et al.* Generalized synthetic strategies toward oxygen vacancy-enriched ZnO–ZnS hollow porous spheres with enhanced photocatalytic hydrogen evolution. *Inorg Chem* 2025, **64**: 3563–3571.
[171] Mourya AK, Singh RP, Amin M, *et al.* Tuning photocatalytic performance via oxygen vacancies and *in situ* ZnS formation on ZnO for hydrogen evolution. *Renew Energ* 2025, **249**: 123166.
[172] Lu SS, Liu YN, Wang SQ, *et al.* Vacancy-rich S-scheme core–shell-like ZnO@ZnS for visible-light photocatalytic degradation of oxytetracycline and hydrogen production in seawater. *ACS Appl Mater Inter* 2025, **17**: 38143–38158.
[173] Han CC, Su PF, Tan BH, *et al.* Defective ultra-thin two-dimensional g-C_3N_4 photocatalyst for enhanced photocatalytic H_2 evolution activity. *J Colloid Interf Sci* 2021, **581**: 159–166.
[174] Gu YP, Han YN, Li YK, *et al.* Phosphorylation promotes liquid-phase proton transfer and carrier separation for boosted photocatalytic hydrogen evolution over g-C_3N_4. *Chem Eng J* 2024, **502**: 158084.
[175] Yang C, Li X, Li M, *et al.* Anchoring oxidation co-catalyst over $CuMn_2O_4$/graphdiyne S-scheme heterojunction to promote eosin-sensitized photocatalytic hydrogen evolution. *Chinese J Catal* 2024, **56**: 88–103.
[176] Pan JQ, Dong ZJ, Wang BB, *et al.* The enhancement of photocatalytic hydrogen production via Ti^{3+} self-doping black TiO_2/g-C_3N_4 hollow core-shell nano-heterojunction. *Appl Catal B Environ* 2019, **242**: 92–99.
[177] Wang XN, Long R, Liu D, *et al.* Enhanced full-spectrum water splitting by confining plasmonic Au nanoparticles in N-doped TiO_2 bowl nanoarrays. *Nano Energy* 2016, **24**: 87–93.
[178] Jeon JP, Kim YJ, Joo SH, *et al.* Benzotrithiophene-based covalent organic framework photocatalysts with controlled conjugation of building blocks for charge stabilization. *Angew Chem Int Edit* 2023, **62**: 202217416.
[179] Li XX, Feng XY, Meng DL, *et al.* Fabrication of TiO_2/MOF type II heterojunction by growth of TiO_2 on Cr-based MOF for enhanced photocatalytic hydrogen production. *Cryst Growth Des* 2025, **25**: 1182–1189.
[180] Azevedo SA, Laranjeira JAS, Silva JF, *et al.* Ag-doped $SrTiO_3$: Enhanced water splitting for hydrogen production. *Int J Hydrogen Energ* 2024, **79**: 199–207.
[181] Zhang WQ, Chu Y, Wang C, *et al.* Enhancing photocatalytic hydrogen production efficiency in all-inorganic lead-free double perovskites via silver doping-induced efficient separation of photogenerated carriers. *Sep Purif Technol* 2025, **357**: 130111.
[182] Zhou P, Chen H, Chao YG, *et al.* Single-atom Pt-I3 sites on all-inorganic Cs_2SnI_6 perovskite for efficient photocatalytic hydrogen production. *Nat Commun* 2021, **12**: 4412.
[183] Gao SQ, Wang BL, Chen FJ, *et al.* Confinement of $CsPbBr_3$ perovskite nanocrystals into extra-large-pore zeolite for efficient and stable photocatalytic hydrogen evolution. *Angew Chem Int Edit* 2024, **63**: 202319996.
[184] Fu H, Zhang QQ, Liu YY, *et al.* Photocatalytic overall water splitting with a solar-to-hydrogen conversion efficiency exceeding 2% through halide perovskite. *Angew Chem Int Edit* 2024, **63**: 202411016.
[185] Guo Q, Zhang JD, Liu JM, *et al.* Promoting charge-carriers dynamics by relaxed lattice strain in A-site-doped halide perovskite for photocatalytic H_2 evolution. *Angew Chem Int Edit* 2025, **64**: 202419082.
[186] Yuan M, Zhou WH, Kou DX, *et al.* $Cu_2ZnSnS4$ decorated CdS nanorods for enhanced visible-light-driven photocatalytic hydrogen production. *Int J Hydrogen Energ* 2018, **43**: 20408–20416.
[187] Raza A, Ali Haidry A, Yao ZJ, *et al.* Construction of S-scheme heterojunction via Cu_2ZnSnS_4 coupled with g-C_3N_4 for enhancing HER performance. *Int J Hydrogen Energ* 2024, **83**: 421–431.
[188] Huang T, Chen W, Liu TY, *et al.* Hybrid of AgInZnS and MoS_2 as efficient visible-light driven photocatalyst for hydrogen production. *Int J Hydrogen Energ* 2017, **42**: 12254–12261.
[189] Chai Y, Kong YH, Lin M, *et al.* Metal to non-metal sites of metallic sulfides switching products from CO to CH_4 for photocatalytic CO_2 reduction. *Nat Commun* 2023, **14**: 6168.
[190] Chandrasekaran S, Yao L, Deng LB, *et al.* Recent advances in metal sulfides: From controlled fabrication to electrocatalytic, photocatalytic and photoelectrochemical water splitting and beyond. *Chem Soc Rev* 2019, **48**: 4178–4280.
[191] Zhu QH, Xu Q, Du MM, *et al.* Recent progress of metal sulfide photocatalysts for solar energy conversion. *Adv Mater* 2022, **34**: 2202929.
[192] Shen SH, Guo PH, Zhao L, *et al.* Insights into photoluminescence property and photocatalytic activity of cubic and rhombohedral $ZnIn_2S_4$. *J Solid State Chem* 2011, **184**: 2250–2256.
[193] Xue MZ, Dong YC, Ye XY, *et al.* A cation exchange strategy to construct highly dispersed copper-doped CdS nanoparticles for photocatalytic hydrogen production. *Int J Hydrogen Energ* 2024, **87**: 1110–1120.
[194] Li BF, Wang WJ, Zhao JW, *et al.* All-solid-state direct Z-scheme $NiTiO_3/Cd_{0.5}Zn_{0.5}S$ heterostructures for photocatalytic hydrogen evolution with visible light. *J Mater Chem A* 2021, **9**: 10270–10276.
[195] Musa EN, Yadav AK, Smith KT, *et al.* Boosting photocatalytic hydrogen production by MOF-derived metal oxide heterojunctions with a 10.0% apparent quantum yield. *Angew Chem Int Edit* 2024: 202405681.
[196] Xu T, Shi JF, Peng KS, *et al.* Organic surface passivation on Rh@CeO_2 cocatalysts for photocatalytic overall water splitting. *Angew Chem Int Edit* 2025, **64**: 202513029.
[197] Zhou YJ, Gao KJ, Song YX, *et al.* Binary direct vs. *ternary electron-mediated Z-scheme heterojunctions: Unraveling pathway-engineered carrier dynamics for photocatalytic hydrogen evolution. Appl Catal B Environ Energy* 2026, **382**: 126002.
[198] Shi M, Wu X, Zhao Y, *et al.* Unlocking the key to photocatalytic hydrogen production using electronic mediators for Z-scheme water splitting. *J Am Chem Soc* 2025: 15540.
[199] Liu W, Zhang CY, Shi JW, *et al.* Improved carriers transfer dynamics through dual-functional charge trapping and electronic tailoring for photocatalytic hydrogen production. *Appl Catal B Environ Energy* 2026, **381**: 125858.
[200] Rahman MZ, Raziq F, Zhang HB, *et al.* Key strategies for enhancing H_2 production in transition metal oxide based photocatalysts. *Angew Chem Int Edit* 2023, **62**: 202305385.
[201] Raja A, Chava RK, Kang M. Enhanced photocatalytic hydrogen generation and degradation performance using a novel design of dual Co and W single metal atom oxides on the interstitial atomic line of TiO_2–g-C_3N_4–rGO. *Chem Eng J* 2025, **513**: 163000.
[202] Bharagav U, Reddy NR, Navakoteswara Rao V, *et al.* Z-scheme driven photocatalytic activity of CNTs-integrated Bi_2S_3/WO_3 nanohybrid catalysts for highly efficient hydrogen evolution under solar light irradiation. *Chem Eng J* 2023, **465**: 142886.
[203] Sun Z, Ran MN, Zhang G. Uncovering intrinsic photochemical behaviour changes of semiconductor and synergistic effects in photothermal catalytic H_2 production from water reduction and cellulose pyrolysis. *Appl Catal B Environ Energy* 2024, **358**: 124398.
[204] Anwar M, Gumaah NF, Ragab AH, *et al.* Enhancing the photocatalytic and biological potential of MnO nanoparticles through strontium doping. *J Mol Struct* 2025, **1343**: 142872.
[205] Kanmaz N, Buğdaycı M, Demircivi P. Exploring photocatalytic tetracycline removal performance under simulated sunlight

irradiation: Milling time effect on metallic reduction of MnO/ZrO_2 mixed oxide. *Ceram Int* 2024, **50**: 44598–44608.
[206] Kanan DK, Carter EA. Ab initio study of electron and hole transport in pure and doped MnO and MnO:ZnO alloy. *J Mater Chem A* 2013, **1**: 9246.
[207] Chen L, Zhao JL, Li JL, *et al.* Cu/Zn-bimetallic organic framework-derived RGO/CuO–ZnO Z-scheme heterojunction for efficient photocatalytic hydrogen production. *Int J Hydrogen Energ* 2025, **103**: 45–52.
[208] Wang D, Qiu GH, Wang H, *et al.* Dual-heterojunctions with reversibly photoactivated structure shift alternately decode photocatalytic H_2 burst and cascade catalytic ROS birth to repress cancer. *Adv Mater* 2026, **38**: 16305.
[209] Deng S, Xiong WP, Zhang GX, *et al.* Metal-free modification overcomes the photocatalytic limitations of graphitic carbon nitride: Efficient production and *in situ* application of hydrogen peroxide. *Adv Energy Mater* 2024, **14**: 2401768.
[210] Bai CW, Liu LL, Chen JJ, *et al.* Circumventing bottlenecks in H_2O_2 photosynthesis over carbon nitride with iodine redox chemistry and electric field effects. *Nat Commun* 2024, **15**: 4718.
[211] Yang M, Chen TT, Chen X, *et al.* Development of graphitic carbon nitride quantum dots-based oxygen self-sufficient platforms for enhanced corneal crosslinking. *Nat Commun* 2024, **15**: 5508.
[212] Liu H, Yang B, Liao GF, *et al.* Facilitating carrier kinetics in ultrathin porous carbon nitride through shear-repair strategy for peroxymonosulfate-assisted water purification. *Nat Commun* 2025, **16**: 5909.
[213] Liu P, Liang T, Li YT, *et al.* Photocatalytic H_2O_2 production over boron-doped g-C_3N_4 containing coordinatively unsaturated FeOOH sites and CoO_x clusters. *Nat Commun* 2024, **15**: 9224.
[214] Wang GW, Zhang HG, Tang TY, *et al.* Ultrathin cobalt phthalocyanine/poly(heptazine imide) heterojunctions with Co–N_4 sites for improved photocatalytic CO_2 reduction and electron kinetics. *Adv Energy Mater* 2025, **15**: 2405622.
[215] Zhao DM, Dong CL, Wang B, *et al.* Synergy of dopants and defects in graphitic carbon nitride with exceptionally modulated band structures for efficient photocatalytic oxygen evolution. *Adv Mater* 2019, **31**: 1903545.
[216] Gao YJ, Liu CJ, Li YW, *et al.* 2,2′ -thienoviologens with low reduction potential for electrochromism and visible-light-driven hydrogen evolution using g-C_3N_4-based composites via hydrogen bonds. *Adv Energy Mater* 2024, **14**: 2470107.
[217] Yu Y, Yan W, Wang XF, *et al.* Surface engineering for extremely enhanced charge separation and photocatalytic hydrogen evolution on g-C_3N_4. *Adv Mater* 2018, **30**: 1705060.
[218] Chen XJ, Wang J, Chai YQ, *et al.* Efficient photocatalytic overall water splitting induced by the giant internal electric field of a g-C_3N_4/rGO/PDIP Z-scheme heterojunction. *Adv Mater* 2021, **33**: 2007479.
[219] Yang Z, Huang TY, Li M, *et al.* Unveiling the synergistic role of frustrated lewis pairs in carbon-encapsulated Ni/NiO_x photothermal cocatalyst for enhanced photocatalytic hydrogen production. *Adv Mater* 2024, **36**: 2313513.
[220] Li Q, Zhang Q, Ye QJ, *et al.* CoRu alloy synergistically co-catalyzes effective photocatalytic hydrogen evolution reaction of carbon nitride. *Appl Surf Sci* 2024, **655**: 159548.
[221] Wu LX, Hu J, Sun C, *et al.* Interfacial engineering between carbon vacancies modified graphitic carbon nitride and CoAl-LDH formed heterojunctions for improved photocatalytic performance: Degradation pathway, DFT calculations, and mechanism insights. *Chem Eng Sci* 2024, **295**: 120191.
[222] Gong YY, Xu ZD, Wu J, *et al.* Enhanced photocatalytic hydrogen production performance of g-C_3N_4 with rich carbon vacancies. *Appl Surf Sci* 2024, **657**: 159790.
[223] Zhang GQ, Sun SR, Jiang WS, *et al.* A novel perovskite $SrTiO_3$–Ba_2FeNbO_6 solid solution for visible light photocatalytic hydrogen production. *Adv Energy Mater* 2017, **7**: 1600932.
[224] Feng JP, Mak CH, Jia GH, *et al.* Unlocking interfacial interactions of *in situ* grown multidimensional bismuth-based perovskite heterostructures for photocatalytic hydrogen evolution. *Adv Energy Mater* 2024, **14**: 2470187.
[225] Wang MY, Zuo YP, Wang JL, *et al.* Remarkably enhanced hydrogen generation of organolead halide perovskites via piezocatalysis and photocatalysis. *Adv Energy Mater* 2019, **9**: 1901801.
[226] Liu XL, Zhang QQ, Zhao SL, *et al.* Integrating mixed halide perovskite photocatalytic HI splitting and electrocatalysis into a loop for efficient and robust pure water splitting. *Adv Mater* 2023, **35**: 2208915.
[227] Fu H, Wu YQ, Guo YH, *et al.* A scalable solar-driven photocatalytic system for separated H_2 and O_2 production from water. *Nat Commun* 2025, **16**: 990.
[228] Yu JX, Huang J, Li RH, *et al.* Fluorine-expedited nitridation of layered perovskite Sr_2TiO_4 for visible-light-driven photocatalytic overall water splitting. *Nat Commun* 2025, **16**: 361.
[229] Xiao JD, Nakabayashi M, Hisatomi T, *et al.* Sub-50 nm perovskite-type tantalum-based oxynitride single crystals with enhanced photoactivity for water splitting. *Nat Commun* 2023, **14**: 8030.
[230] Pan S, Li J, Wen ZC, *et al.* Halide perovskite materials for photo (electro)chemical applications: Dimensionality, heterojunction, and performance. *Adv Energy Mater* 2022, **12**: 2004002.
[231] Kim M, Lee B, Ju H, *et al.* Oxygen-vacancy-introduced $BaSnO_{3-\delta}$ photoanodes with tunable band structures for efficient solar-driven water splitting. *Adv Mater* 2019, **31**: 1903316.
[232] Tao XP, Zhou HP, Zhang CB, *et al.* Triclinic-phase bismuth chromate: A promising candidate for photocatalytic water splitting with broad spectrum ranges. *Adv Mater* 2023: 2211182.
[233] Li JH, Ding LL, Su ZY, *et al.* Non-lignin constructing the gas–solid interface for enhancing the photothermal catalytic water vapor splitting. *Adv Mater* 2023, **35**: 2305535.
[234] Murthy DHK, Nandal V, Furube A, *et al.* Origin of enhanced overall water splitting efficiency in aluminum-doped $SrTiO_3$ photocatalyst. *Adv Energy Mater* 2023, **13**: 2302064.
[235] Sun JW, Farid MU, Li XL, *et al.* MXene membrane as multifunctional interface for vapor splitting via photothermal-catalytic membrane distillation. *Adv Mater* 2026, **38**: 13926.
[236] Avcıoğlu C, Avcıoğlu S, Bekheet MF, *et al.* Photocatalytic overall water splitting by $SrTiO_3$: Progress report and design strategies. *ACS Appl Energy Mater* 2023, **6**: 1134–1154.
[237] Chen GQ, Wang P, Wu YQ, *et al.* Lead-free halide perovskite $Cs_3Bi_{2x}Sb_{2-2x}I_9$ ($x \approx 0.3$) possessing the photocatalytic activity for hydrogen evolution comparable to that of $(CH_3NH_3)PbI_3$. *Adv Mater* 2020, **32**: 2001344.
[238] Chen S, Yin HJ, Liu PR, *et al.* Stabilization and performance enhancement strategies for halide perovskite photocatalysts. *Adv Mater* 2023, **35**: 2203836.
[239] Wang J, He SY, Zhang M, *et al.* *In-situ* constructing eosin Y sensitized $Cs_2PtSnCl_6$ perovskites for enhanced photocatalytic hydrogen evolution. *Adv Energy Mater* 2025, **15**: 2406048.
[240] Shi M, Li GN, Tian WM, *et al.* Understanding the effect of crystalline structural transformation for lead-free inorganic halide perovskites. *Adv Mater* 2020, **32**: 2002137.
[241] Ran JR, Gao GP, Li FT, *et al.* Ti_3C_2 MXene co-catalyst on metal sulfide photo-absorbers for enhanced visible-light photocatalytic hydrogen production. *Nat Commun* 2017, **8**: 13907.
[242] Xu HT, Xiao R, Huang JR, *et al.* *In situ* construction of protonated g-C_3N_4/Ti_3C_2 MXene Schottky heterojunctions for efficient photocatalytic hydrogen production. *Chinese J Catal* 2021, **42**: 107–114.
[243] Li YM, Yang L, He HJ, *et al.* *In situ* photodeposition of platinum clusters on a covalent organic framework for photocatalytic hydrogen production. *Nat Commun* 2022, **13**: 1355.
[244] Zhao XD, Liu Q, Li XL, *et al.* Exited state absorption upconversion induced by structural defects for photocatalysis with a breakthrough efficiency. *Angew Chem Int Edit* 2023, **62**: 202219214.

[245] Shundo Y, Tam Nguyen T, Akrami S, *et al.* Oxygen vacancy-rich high-pressure rocksalt phase of zinc oxide for enhanced photocatalytic hydrogen evolution. *J Colloid Interf Sci* 2024, **666**: 22–34.

[246] Huang QP, Yang C, Yin Q, *et al.* Building ultrathin MOL/MOL S-scheme heterostructures toward boosted photocatalytic charge kinetics for efficient H_2Evolution. *Angew Chem Int Edit* 2025, **64**: 202502009.

[247] Xu YX, Qiu F, Xu SQ, *et al.* Boosting photocatalytic hydrogen evolution by a light coupling and charge carrier confinement strategy. *Adv Funct Mater* 2025, **35**: 2417553.

[248] Yu CY, He JJ, Tan MX, *et al.* Selective enhancement of photo-piezocatalytic performance in $BaTiO_3$ via heterovalent ion doping. *Adv Funct Mater* 2023, **33**: 2310927.

[249] Li ZY, Zhang XY, Xue M, *et al.* Enhanced peroxymonosulfate activation in organic degradation by modulating cationic doping of $Ba_xSr_{1-x}Co_yFe_{1-y}O_{3-\delta}$ perovskites: DFT calculations and mechanism study. *Appl Catal B Environ Energy* 2025, **377**: 125502.

[250] Zhao YP, Yavuz I, Wang MH, *et al.* Suppressing ion migration in metal halide perovskite via interstitial doping with a trace amount of multivalent cations. *Nat Mater* 2022, **21**: 1396–1402.

[251] Chen J, Zhang XT, Cai XY, *et al.* Design of donor-acceptor type 2D covalent organic frameworks as efficient photocatalysts for visible-light-driven water splitting. *Adv Funct Mater* 2025, **35**: 2505453.

[252] Wu H, Qu SY, Ng YH. Bismuth vanadate capable of driving one-step-excitation photocatalytic overall water splitting. *J Am Chem Soc* 2025, **147**: 10829–10833.

[253] Zhang J, Li XJ, Chang JH, *et al.* Dual electric fields in cyclooctatetrathiophene-based COF/$ZnIn_2S_4$ Z-scheme heterojunction boost photocatalytic seawater hydrogen evolution. *Angew Chem Int Edit* 2026, **65**: 19752.

[254] Wu LB, Lu WH, Ong WL, *et al.* Photothermal-promoted anion exchange membrane seawater electrolysis on a nickel-molybdenum-based catalyst. *Nat Commun* 2025, **16**: 3098.

[255] Han C, Zeng ZK, Zhang XR, *et al.* All-in-one: Plasmonic Janus heterostructures for efficient cooperative photoredox catalysis. *Angew Chem Int Edit* 2024, **63**: 202408527.

[256] Liu BX, Li YF, Guo YC, *et al.* Regulating the transfer of photogenerated carriers for photocatalytic hydrogen evolution coupled with furfural synthesis. *ACS Nano* 2024, **18**: 17939–17949.

[257] Huang ZS, Wang YF, Qi MY, *et al.* Interface synergy of exposed oxygen vacancy and Pd lewis acid sites enabling superior cooperative photoredox synthesis. *Angew Chem Int Edit* 2024, **63**: 202412707.

[258] Jia ZW, Li R, Ji PZ, *et al.* Design and fabrication of a novel 2D/3D $ZnIn_2S_4$@Ni1/UiO-66-NH_2 heterojunction for highly efficient visible-light photocatalytic H_2 evolution coupled with benzyl alcohol valorization. *Appl Catal B Environ Energy* 2024, **357**: 124279.